September 2002

The MEG experiment: search for the $\mu^+ \to e^+\gamma$ decay at PSI

Research Proposal to INFN

A. Baldini[4*], A. de Bari[5], L. M. Barkov[1], C. Bemporad[4], P. Cattaneo[5], G. Cecchet[5], F. Cei[4], T. Doke[9], J. Egger[7], F. Gatti[6], M. Grassi[4], A. A. Grebenuk[1], D. G. Grigoriev[1], T. Haruyama[2], P.-R. Kettle[7], B. Khazin[1], J. Kikuchi[9], Y. Kuno[3], A. Maki[2], Y. Makida[2], T. Mashimo[8], S. Mihara[8], T. Mitsuhashi[8], T. Mori[8*], D. Nicolò[4], H. Nishiguchi[8], H. Okada[9], W. Ootani[8], K. Ozone[8], R. Pazzi[4], N. M. Ryskulov[1], S. Ritt[7], T. Saeki[8], R. Sawada[8], F. Sergiampietri[4], G. Signorelli[4], S. Suzuki[9], K. Terasawa[9], A. Yamamoto[2], M. Yamashita[9], S. Yamashita[8], K. Yoshimura[2], T. Yoshimura[9]

[1]BINP, Novosibirsk, Russia
[2]KEK, Tsukuba, Japan
[3]Osaka University, Osaka, Japan
[4]INFN, University and Scuola Normale Superiore, Pisa, Italy
[5]INFN and University of Pavia, Pavia, Italy
[6]INFN and University of Genova, Genova, Italy
[7]PSI, Villigen, Switzerland
[8]University of Tokyo, Tokyo, Japan
[9]Waseda University, Tokyo, Japan

*co–spokesmen

Contents

1 Physics Motivation **9**
- 1.1 Supersymmetric Grand Unified Theory . . . 9
- 1.2 Connection with Neutrino Oscillations . . . 11

2 Beam and Target **13**
- 2.1 Beam . . . 13
- 2.2 Target . . . 17

3 The Positron Detector **19**
- 3.1 Concept of the COBRA spectrometer . . . 19
- 3.2 Thin-wall Superconducting Magnet . . . 20
  - 3.2.1 Overview of the design of the COBRA magnet . . . 20
  - 3.2.2 Development of the superconducting cable . . . 21
  - 3.2.3 Suppression of the stray field . . . 23
  - 3.2.4 Mechanical design of the COBRA magnet . . . 29
  - 3.2.5 Transparency of the magnet . . . 29
- 3.3 Chamber System . . . 29
  - 3.3.1 Drift Chambers R&D . . . 32
  - 3.3.2 Pattern Recognition . . . 37
  - 3.3.3 Tracker Resolutions . . . 37
- 3.4 Timing Counter . . . 40

4 The Photon Detector **47**
- 4.1 General design . . . 47
- 4.2 Photon detector R&D . . . 49
  - 4.2.1 The large prototype . . . 49
  - 4.2.2 Gamma beam test at TERAS . . . 50
  - 4.2.3 Purification system . . . 60
- 4.3 Final photon detector . . . 68
  - 4.3.1 Expected Performance . . . 68
  - 4.3.2 Calibration method . . . 73
  - 4.3.3 Cryostat design . . . 73

5 Electronics, Trigger and DAQ **77**
- 5.1 Slow Control System . . . 77
- 5.2 High Voltage System . . . 78

5.3 Trigger rate estimates . . . 79
5.3.1 The trigger system . . . 82
5.4 Front-end Electronics . . . 84
5.5 Data Acquisition . . . 86

6 Sensitivity and Background **87**
6.1 Single Event Sensitivity . . . 87
6.2 Background . . . 87
6.2.1 Prompt Background . . . 88
6.2.2 Accidental Background . . . 88

7 Collaboration, Cost and Schedule **91**
7.1 Collaboration . . . 91
7.2 Cost . . . 91
7.3 Schedule . . . 91

A The Past Experiments **95**

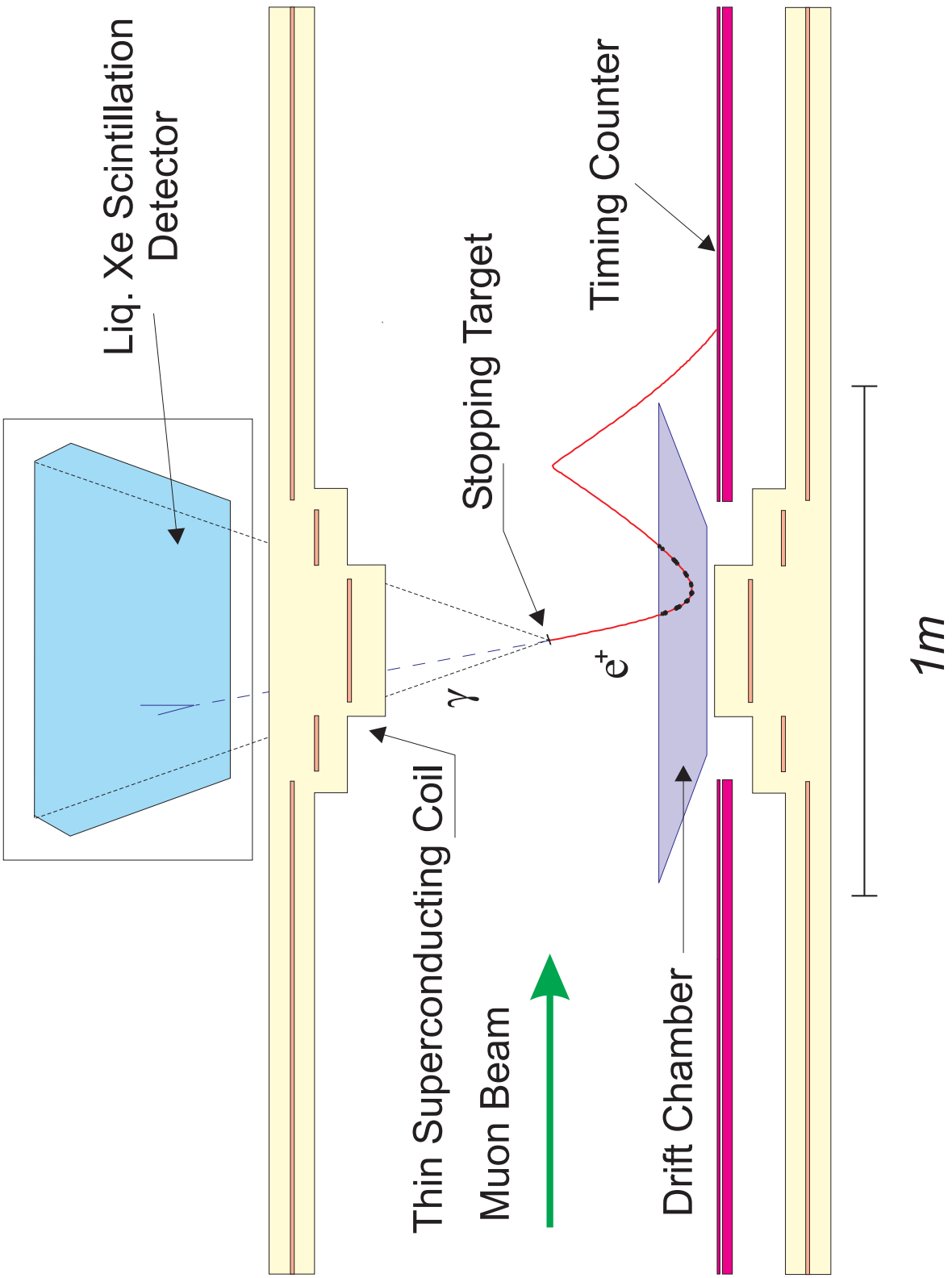

Figure 1: Schematic view of the detector

Introduction

We propose to search for the lepton-flavor-violating decay $\mu^+ \to e^+\gamma$ with a sensitivity of $\sim 5 \times 10^{-14}$, an improvement of about two order of magnitudes with respect to the present best limit set by the MEGA experiment [1].

Fundamental theories such as supersymmetric unification predict [2] that $\mu^+ \to e^+\gamma$ should occur with a decay branching ratio that, apart from accidental cancellations, should be above 10^{-14}. This experiment has therefore a real chance of making a discovery, which would provide very clear evidence for new physics beyond the Standard Model.

Even a non-observation of the decay at the foreseen level of sensitivity would place a stringent constraint on these theories and on the general nature of the new physics, and will thus be of crucial importance in pointing out the future direction of particle physics, though with the recent evidence of neutrino oscillations provided by the Super Kamiokande [3, 4] and SNO [5] experiments the importance of such a search is greatly enhanced.

The see-saw mechanism [6] induced by superheavy ($10^{12} \div 10^{15}$GeV) right-handed gauge singlets (ν_{R_i}) is considered to be a promising candidate in the explaination of the origin of the extremely small neutrino masses. It is pointed out [7] that the off-diagonal slepton mass-matrices, induced by the same right-handed singlets, will significantly contribute to the $\tau \to \mu\gamma$ and $\mu \to e\gamma$ decay rates. When inserted into this framework, the recent results of the solar neutrino experiments predict $\mu \to e\gamma$ rates very close to the present experimental limit. The $\mu^+ \to e^+\gamma$ decay can therefore be a unique way of observing the isolated world of the right-handed gauge singlets, postulated to exist at ultra high energies.

In the framework of the theories mentioned above, our sensitivity to $\mu^+ \to e^+\gamma$ corresponds [8] to a sensitivity of $\sim 10^{-16}$ on the $\mu-e$ conversion process with an aluminum target, slightly above that the proposed MECO experiment aims to reach [9].

The MEG experiment will be conducted at PSI, using the πE5 beam, the most intense DC muon beam presently available in the world. A schematic view of the detector is shown in Fig. 1. The muon beam is brought to stop in a thin target after passing a stage in which most of the contaminating positrons are eliminated. Depending on the ultimate resolutions of the individual devices, we will choose the optimal beam intensity in order to have the lowest accidental background rate. Our beam studies aim at reaching a muon stop rate of the order of 10^8/s in a ~ 0.5 cm radius spot.

The momentum and the direction of the emerging e^+ are measured precisely by a "COnstant-Bending-RAdius (COBRA) spectrometer", composed of a quasi-solenoidal magnetic field. This field is shaped so that monochromatic e^+s from the target follow trajectories with constant projected bending radius, independent of the emission angle over a wide angular range. This allows a defined window on the absolute e^+ momentum to be set for detection by the drift chamber cells placed at the outermost radii, thereby reducing the accidental pile-up of the Michel e^+ much more effectively than what is possible with a simple solenoidal configuration as that employed by MEGA. This new feature, together with the special arrangement of the drift chamber cells, makes the pattern recognition securer against pile-up, particularly

at our beam rate, which is well below the instantaneous stop rate (2.5×10^8/s) MEGA accepted. Simulation shows the expected FWHM resolutions range between 0.7 and 0.9% for the positron momentum and from 9 to 12 mrad for the angle.

A hodoscope array of plastic scintillators is placed on each side of the spectrometer to measure the impact point and the timing of the e^+ with resolutions (FWHM) of 2 cm and 0.1 ns, respectively.

While all e^+ are confined inside the magnet, the γ-rays penetrate through the thin superconducting coil of the spectrometer with $\simeq 80\%$ transmission probability, and are detected by a liquid Xenon scintillation detector of a "Mini-Kamiokande" type, which consists of a 0.8 m^3 volume of liquid Xenon viewed from all sides by about 800 photomultipliers. We use only the scintillation light and do not attempt to collect the ionization, thus making our photon detector simpler. The scintillation pulse from the Xe is very fast and has a short tail, thereby minimizing the pile-up problem, which can further be reduced by off-line analyses of the image-pattern and the pulse-shapes.

Tests on a large scale prototype as well as a full simulation show that one can expect FWHM resolutions of 4% for the energy, 10.5 mm for the position and 0.1 ns for the timing measurements for 52.8 MeV γ-rays.

A first proposal containing the conceptual description of the apparatus was presented to PSI in 1999 by one part of the collaboration [10]. Much effort has since been put into detailed R&D on all the experimental devices; the results will be described in the following sections.

The wider collaboration signing this document believes, on the basis the studies performed, that the proposed detectors will allow to reach a 5×10^{-14} sensitivity (and consequently a $\sim 1 \times 10^{-13}$ 90% C.L. limit in case of no signal observed) but a further improvement is possible and only operation of the experimental apparatus will enable to understand what the final sensitivity will be.

1. Physics Motivation

In the Standard Model, lepton flavor conservation (LFC) is built in by hand with assumed vanishing neutrino masses. The introduction of neutrino masses and mixing into the Standard Model also predicts unmeasurably small lepton flavor violation (LFV). On the other hand, fundamental theories such as Supersymmetry (SUSY) generically predict LFV at a measurable level. Lepton-flavor-violating processes such as $\mu^+ \to e^+\gamma$ are therefore very clean (i.e. not contaminated by the background of the Standard Model) and at the same time present a promising area to hunt for signals of profound new physics.

Taking the case of the recent $(g_\mu - 2)$ results. Despite the improvement of a factor of two in the experimental uncertainty [11] the measured value lies between $1.6 \div 2.6$ σ Standard Model prediction, depending on the way the theoretical value is computed. We just note here that a real discrepancy between the measured and the Standard Model predicted $a_\mu \sim 10^{-9}$ could imply $\mu^+ \to e^+\gamma$ rates close to 10^{-11} in the framework of supersymmetric theories [12].

In the following two sections we briefly discuss the predicted rates for the $\mu^+ \to e^+\gamma$ decay in grand unified supersymmetric theories caused by slepton mixing due to radiative corrections and by the inclusion of a see–saw mechanism for the neutrino masses. We observe that these two sources of LFV are independent and always present in all supersymmetric grand unified models.

LFV has recently been examined also in the framework of theories with extra spatial dimensions (see for instance [13]). Rates above 10^{-14} are again expected and the experiment proposed here would therefore be crucial even in testing these new ideas.

1.1 Supersymmetric Grand Unified Theory

LFV processes are especially sensitive to the supersymmetric extensions of the Standard Model, in particular supersymmetric grand unified theories (SUSY-GUT). In SUSY-GUT, finite slepton mixing appears through radiative corrections in the renormalization group evolution from the GUT to the weak energy scale, even if the slepton mass matrix is assumed to be diagonal at the Plank scale [14]. It has been pointed out that the slepton mixing thus generated can be very large owing to the heavy top-quark mass [2], thereby enhancing $\mu^+ \to e^+\gamma$ decay through the loop diagrams shown in Fig. 1.1. The predicted branching ratio of $\mu^+ \to e^+\gamma$ in SUSY SU(5) models [15] is shown in Fig. 1.2. It ranges from 10^{-15} to 10^{-13} for the singlet smuon mass $m_{\tilde{\mu}_R}$ of 100 to 300 GeV.

Recent combined analyses of the four LEP experiments have excluded most of the SUSY parameter space with $\tan\beta < 10$ [16]. The predicted $\mu \to e\gamma$ rates for higher $\tan\beta$ values should be measurable by the experiment proposed here.

The SO(10) SUSY-GUT models predict an even larger rate than for SU(5) (10^{-13} to 10^{-11}) due to an enhancement factor of $(m_\tau^2/m_\mu^2) \sim 100$ [2], induced by the loop diagrams whose magnitude is proportional to the tau-lepton mass.

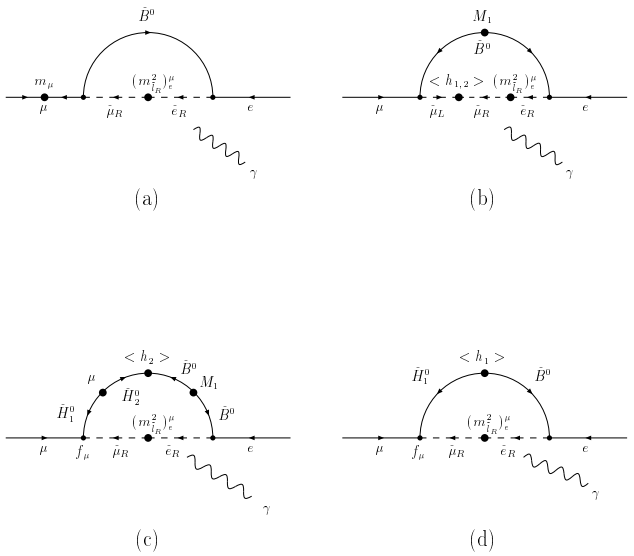

Figure 1.1: Diagrams of $\mu^+ \to e^+\gamma$ in SU(5) SUSY models.

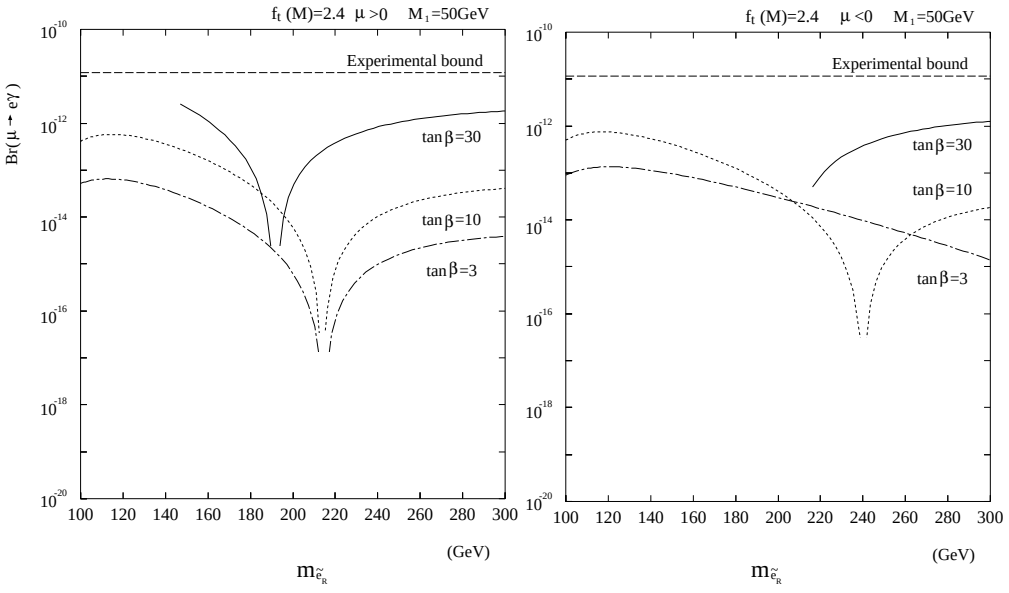

Figure 1.2: Predictions of $\mu^+ \to e^+\gamma$ branching ratio in SU(5) SUSY models [14].

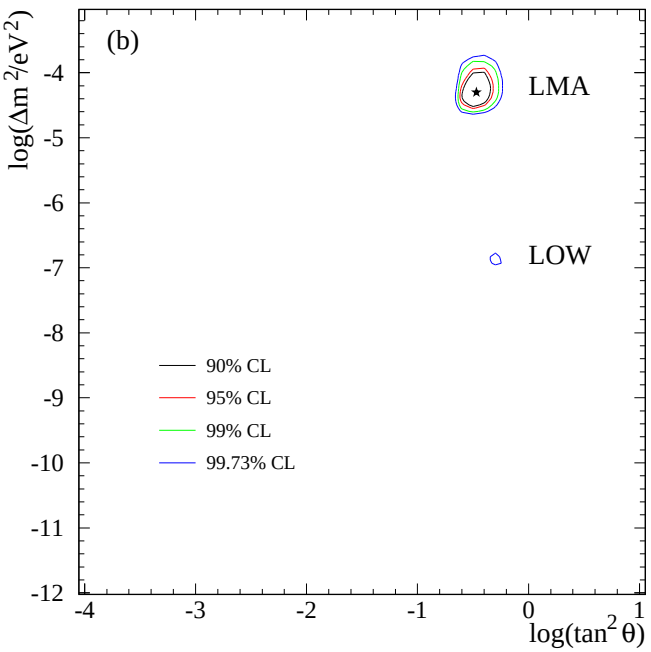

Figure 1.3: Possible solutions for solar neutrino oscillations in the $\tan^2\theta$ vs Δm^2 parameter space after the recent SNO [5] measurements.

1.2 Connection with Neutrino Oscillations

The phenomenon of neutrino oscillations which has been established by experimental observation of atmospheric [3, 17, 18] and solar [4, 5, 19, 20, 21, 22, 23] neutrinos implies both non-zero neutrino masses and LFV. In SUSY models, neutrino mixing is expected to enhance the rate of LFV processes such as $\mu^+ \to e^+\gamma$ [7, 24, 25].

A possible contribution to the slepton mixing between $\tilde{\mu}$ and $\tilde{e}$ is from V_{21} (between ν_1 and ν_2), corresponding to the mixing needed to explain the solar neutrino deficit. The recent SNO solar neutrino observations [5], when combined with all the previous measurements, confine the mixing parameters to two allowed regions, namely the MSW large mixing angle solution (LMA) and the MSW large angle–low Δm^2 (LOW) solution, as shown in Fig. 1.3. The plot in Fig. 1.4 shows the predictions for $\mu^+ \to e^+\gamma$ decay corresponding to the two solutions as a function of the mass of the right-handed gauge singlet ν_{R_2}. The vacuum solutions is also shown for completeness though it is excluded by the SNO analysis.

The width of the predicted bands is associated with the possible $\tan\beta$ parameter values. We observe again (see the previous section) that the lowest $\tan\beta$ values, corresponding to lower $\mu \to e\gamma$ rates, are highly disfavored by the recent analyses of the LEP data [16].

In conclusion, the $\mu^+ \to e^+\gamma$ branching ratio, when combined with Δm^2 and mixing angle measurements by solar neutrino experiments, will determine or severely constrain the mass scale of the right-handed gauge singlet, postulated to exist at ultra high energies ($10^{12} \div 10^{15}$ GeV).

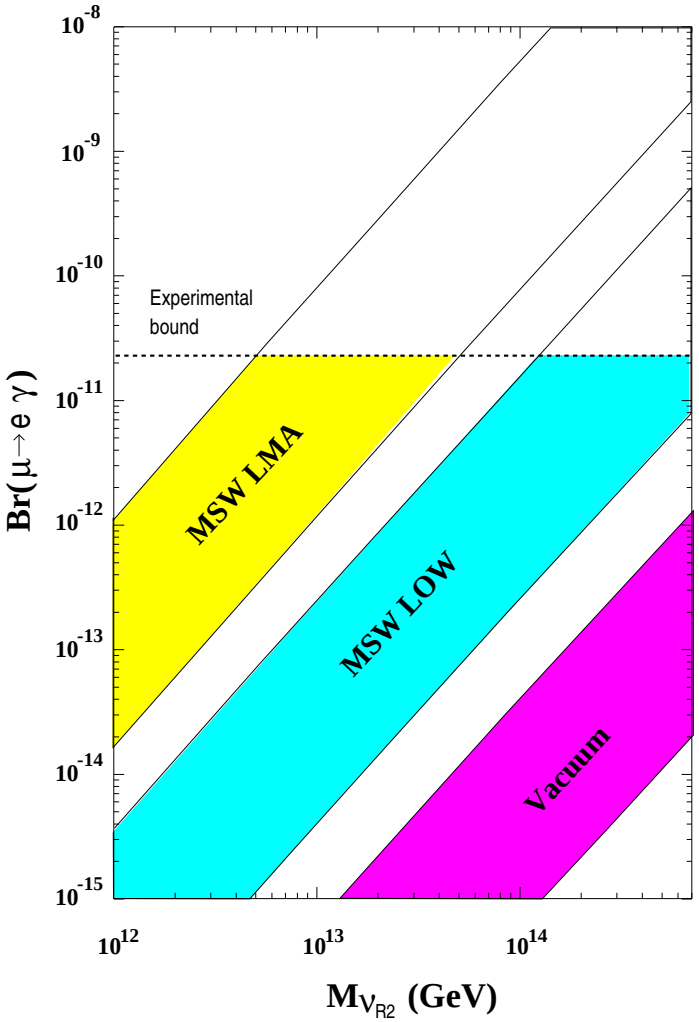

Figure 1.4: $\mu \to e\gamma$ branching ratios as a function of the mass of the right-handed gauge singlet ν_{R_2} for the different (LMA and LOW) solutions allowed by the solar neutrino experiments. The vacuum solution case is shown for completeness though excluded by the SNO experiment (from ref. [7]).

2. Beam and Target

2.1 Beam

The πE5 channel [26] extracts low-energy pion and muon beams from the thick production target at an angle of 175° with respect to the primary proton beam. The main characteristics of the beam are listed in Table 2.1. For this experiment the beam channel will be tuned to ≈ 28 MeV/c to collect surface muons (muons coming from the decay at rest of pions on the production target surface). Measurements indicate that we can expect a beam intensity up to $(8 \div 10) \times 10^8 \mu^+/\mathrm{s}$ for the primary proton current of 1.5 mA [26].

solid angle acceptance	150 msr
momentum range	$20 \div 120$ MeV/c
length	10.4 m
momentum band (FWHM)	10%
momentum resolution (FWHM)	2%
horizontal emittance	15.3 cm·rad
vertical emittance	3.6 cm·rad
spot size	4×4 cm^2

Table 2.1: Main properties of πE5.

In order to be able to reach the best sensitivity to the $\mu \to e\gamma$ decay it is necessary to have a well understood beam transport system delivering a high intensity surface muon beam (up to $1 \div 2 \times 10^8$ μ^+/s) with a minimum spot-size and a small momentum spread, that must be stopped in a thin target, with a minimum of contaminant particles (positrons) entering the detectors.

Positron contamination can be reduced 1) either by using a mass selection device (Wien filter) or 2) with a combination of an energy degrader and a magnetic selection.

In the πE5 beamline two separate branches are present, a "U"-branch feeding the πE52-area and a "Z"-branch feeding the πE51-area (Figure 2.1).

Option 2) for reducing the number of e^+ was used in previous measurements on the "Z"-branch [27], showing that a suitable number of muons, with a low positron contamination, could be stopped in a final focus with the help of a large aperture, 8.5 m long solenoidal magnet (PMC-magnet).

A comparative study on the "U"-branch was started with a beam test [28], during 2001, which however, was prematurely ended by a technical problem in the primary beam-blocker system of the πE5 beam line. This study of the "U"-branch is presently being continued.

Table 2.2 gives an overview of the comparative rate quantities obtained from the last "U"-branch and previous "Z"-branch measurements, using a degrader in both cases for separation and moderation. All

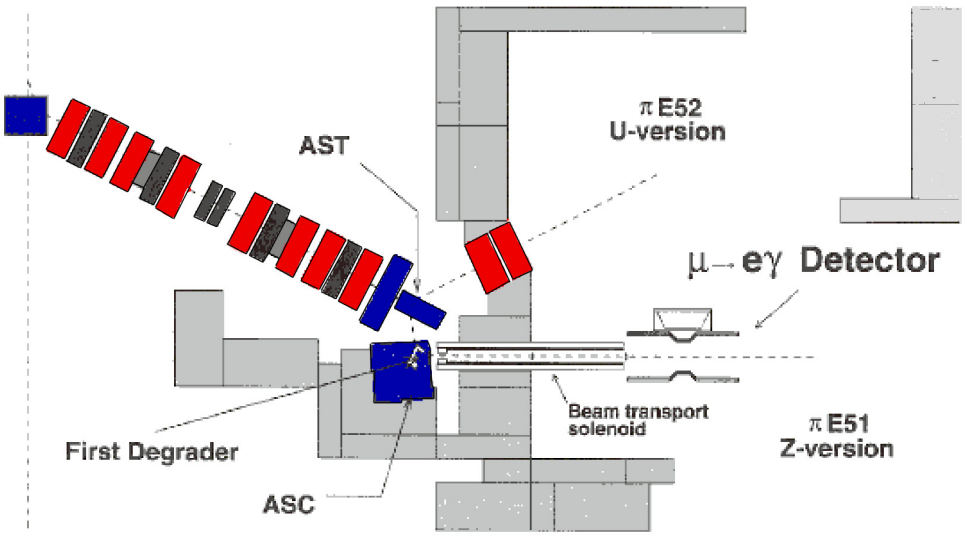

Figure 2.1: πE5 Beam line and experimental area showing the two branches, "U" leading to the πE52-zone and "Z" leading to the πE51-zone. It is shown an experimental layout only for the "Z" version.

quoted results, unless otherwise stated, are normalized to a 1800 μA of beam current on a 6 cm long E–Target and a momentum bite of 6.4% FWHM.

The present results from the "U"-branch measurements give an unacceptable rate loss. The solution to this problem is being tackled in a beam test currently going–on at PSI, in which measurements using a Wien-filter are being performed. A 1 m long solenoid is also used in order to simulate the final experimental set-up. A simulation of the present beam optics, as given by TRANSPORT [29] is shown in Figure 2.2. In the solenoid there is one intermediate focus for a degrader, followed by the final focus where the stop target will be placed. A simulation of the set-up using the 2^{nd}–order ray tracing programme TURTLE [29] showed (Figure 2.3) [51] that we expect $2.7 \cdot 10^8$ μ^+/s at the final focus, without any degrader in the solenoid.

The estimated phase space of the beam at this point, taken from TURTLE, gives an rms half-width

Condition	"Z"-branch	"U"-branch
No Degrader, Transmitted to Zone	$3.6 \cdot 10^8$ μ^+/s	$3.5 \cdot 10^8$ μ^+/s
	$6.0 \cdot 10^8$ e^+/s	$1.6 \cdot 10^9$ e^+/s
Degrader, at Final Focus	$2.0 \cdot 10^8$ μ^+/s	$3.2 \cdot 10^7$ μ^+/s
μ/e ratio at Muon Peak	9	16.5

Table 2.2: Comparison of "U"- and "Z"-branches for various conditions

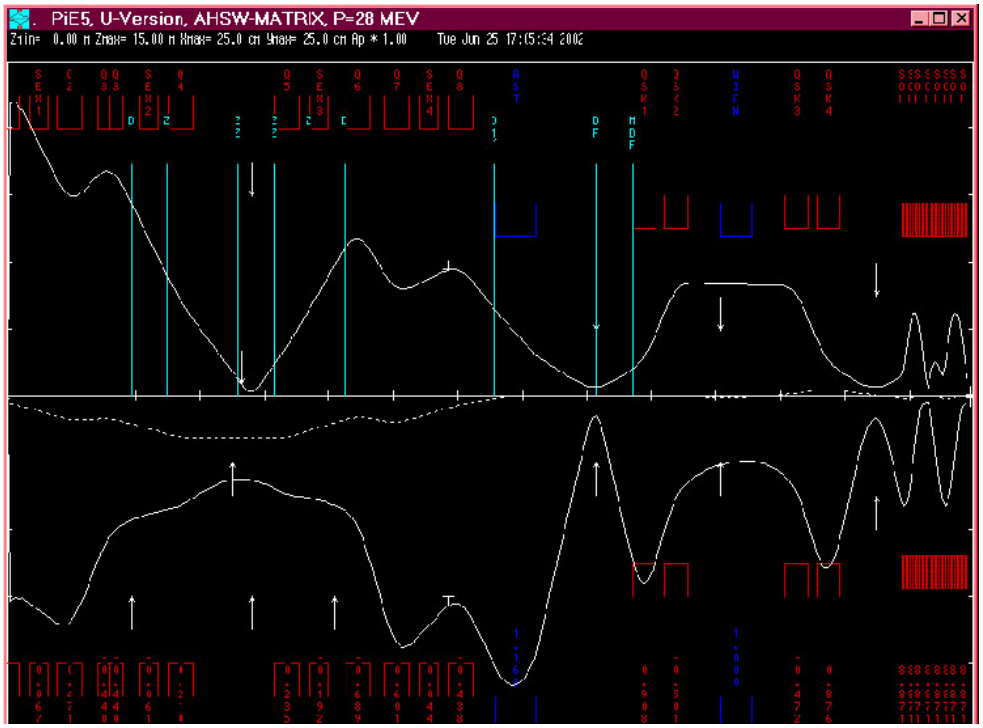

Figure 2.2: πE5 TRANSPORT beam envelopes (solid white lines) for the proposed Wien-filter set-up in the "U"-branch. The vertical envelopes are shown in the upper-half of the figure and the horizontal in the lower-half. The dashed line shows the momentum dispersion trajectory for a 1% higher momentum. The beam elements and their apertures are shown in red and blue. The horizontal axis is in 1 m intervals along the central trajectory of the beam line, whereas the vertical scale is shown in 5 cm divisions.

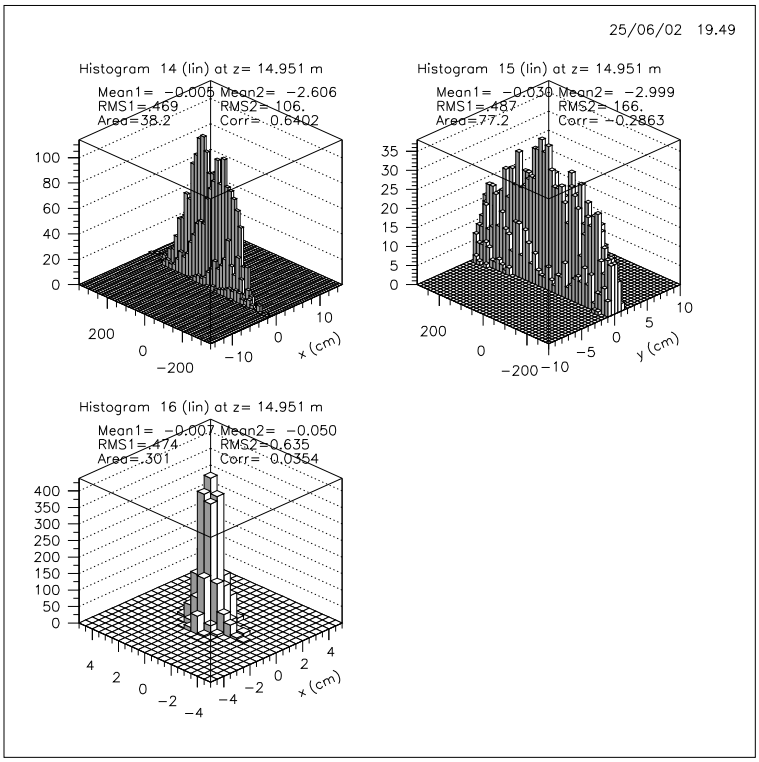

Figure 2.3: πE5 TURTLE 2$^{\text{nd}}$-order calculation output for the proposed Wien-filter set-up in the "U"-branch. The three histograms show the beam phase space 5 cm after the exit of the solenoid. The top-left shows the $(x - x')$ phase space in cm·mrad, followed consecutively by the $(y - y')$ and finally the beam spot size $(x - y)$ in cm. The simulation is for a total of 20 000 particles tracked through the set-up; approximately 17% of the muons make it to the final focus, with more than 70% being lost up to and including the momentum slits.

of the horizontal and vertical profiles of $\sigma_x = 5$ mm, $\sigma_y = 6$ mm, with divergences in the horizontal and vertical planes of $x' = 106$ mrad and $y' = 166$ mrad, respectively. We used these values in our Monte Carlo simulations.

Concerning the "Z"-branch, where a suitable number of surface muons as well as a reasonable beam positron separation could be achieved phase space was not measured but rather imposed through collimation. It is planned to undertake phase–space measurements in the "Z"-branch in November 2002, such that all the results necessary for a decision as to which branch will eventually be used, can be obtained by the end of 2002.

2.2 Target

The target will be placed at a slant angle of 22° (corresponding to a slant ratio of 1 : 2.5) in a He-gas filled region. A possible stopping target could be made of Mylar, 100 μm thick. This is the solution we chose for our Monte Carlo simulations and in our first tests. The main reason Mylar was used was that it was already implemented for the beam windows and convenient thicknesses were readily available. However, for a real measurement, the best possible material must be chosen.

Assuming a central beam momentum of 28 MeV/c, with a momentum bite of 6.4% FWHM, a material simulation was done using the GEANT [30] code. Three target/degrader materials were looked at: Polyethylene $(CH_2)_n$, Mylar $(C_5H_4O_2)_n$ and Kapton $(C_{22}H_{10}N_2O_5)_n$. The mean range was found to be $\sim$ 1100 μm in the case of CH_2 and $\sim$ 870 μm for both the other materials, with the range straggling varying between 7.8% and 8.2% respectively. Assuming an equivalent 100 μm Mylar thickness of the target, a CH_2 target with a density of 0.95 g/cm^3, would have to be 150 μm thick, if placed at the same slant angle. This would imply a residual material thickness of 700 μm of Polyethylene as a degrader. In the case of Mylar the respective thicknesses are 100 μm for the target and 600 μm for the degrader. This implies about 16% less multiple scattering for both muons and higher energy positrons in the degrader for the case of Polyethylene as well as 20% less equivalent material for the degrader. The radiation length X_0 in the case of Polyethylene is also about 12% longer than that of Mylar, giving a total of 30% less X_0's in the case of a CH_2 degrader.

Overall, it seems that Polyethylene is the best material from both a background suppression and a beam quality point of view. However, questions such as the depolarization characteristics of these materials are being checked and a serious look into the mechanical suitability for constructing a zero-materials, infinite precision target suspension system is starting. The experience and knowledge obtained by the previous experiments, mainly MEGA and the Crystal Box Collaborations, concerning the target questions and the use of special calibration targets has been duely noted and will also be taken into account.

3. The Positron Detector

The positron detector, schematically shown in Fig. 3.1, consists of a magnet specially designed to form a gradient field, a drift chamber system to measure the positron momentum and scintillation counters to measure the positron timing.

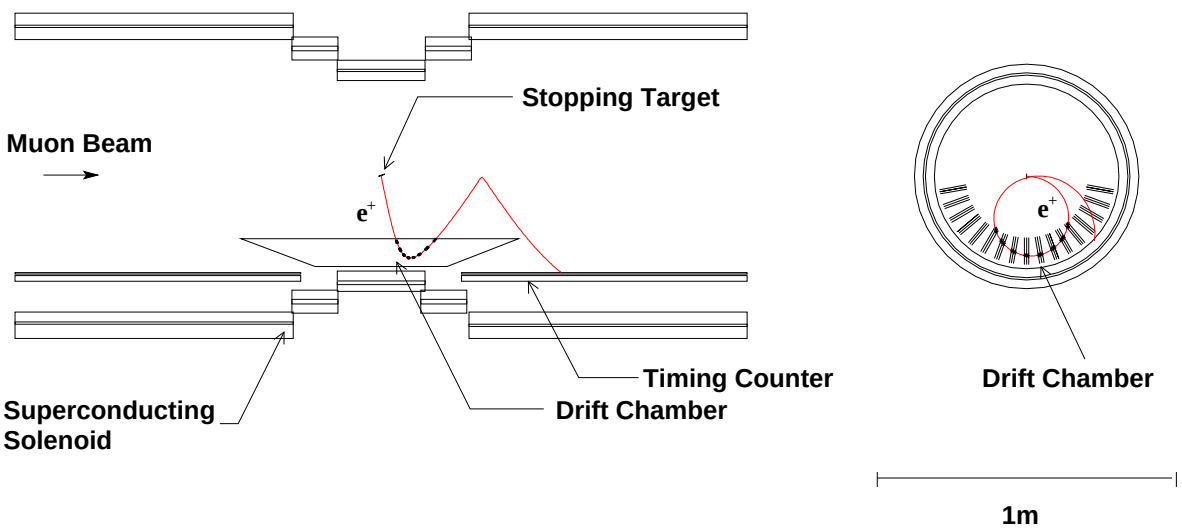

Figure 3.1: Schematic view of the positron spectrometer.

3.1 Concept of the COBRA spectrometer

A solenoidal magnetic field in general has the merit of confining low momentum tracks within a certain radius so that in the case of muon decay a large fraction of Michel positrons do not reach the track-detectors located at large radii. However, as shown in Fig. 3.2(a), in a simple uniform solenoidal field such as the one adopted in the MEGA experiment, positrons emitted close to 90° make many turns in the tracking chamber, thereby causing problems in pattern recognition or even making a stable operation of the chambers difficult. Also, the bending radius of positrons of a given absolute momentum depends on the production angle, which makes it difficult to select high momentum tracks, as shown in Fig. 3.2(b).

In order to avoid these problems, we have adopted a solenoid with a gradient field, which provides the central field of 1.25 Tesla at $z = 0$ and slowly decreasing field as $|z|$ increases. As shown in Fig. 3.3(a), the positrons emitted close to 90° are swept away by this gradient field much more quickly than in the

case of the uniform magnetic field.

The gradient field is arranged such that monochromatic positrons from the target follow trajectories with a constant projected bending radius independent of the emission angle, as shown in Fig. 3.3(b): the bending radius is determined by the absolute momentum and not by its transverse component. This allows us to define the absolute momentum window of positrons to be detected by the drift chamber cells.

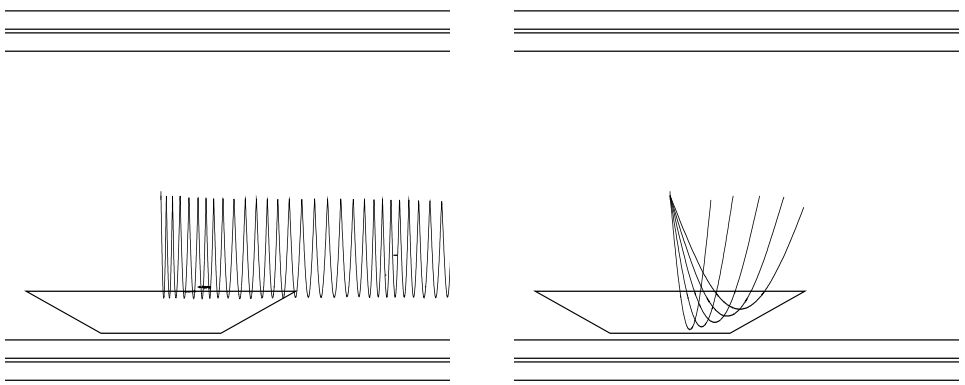

Figure 3.2: Problems with a uniform solenoidal magnetic field:
(a) $r - z$ view of the solenoid shown with the trajectory of a particle emitted at 88° making many turns inside the detector.
(b) Trajectories of monochromatic particles emitted at various angles. The bending radius depends on the emission angle.

Fig. 3.4 shows the rate of Michel positrons per cm^2 per second as a function of radius for a muon decay rate of 1×10^8/s. By placing the chamber at a radius larger than 20 cm the counting rate can be contained to a level below the limit of stable chamber operation. Note that the rates at the outermost radii are especially low.

3.2 Thin-wall Superconducting Magnet

3.2.1 Overview of the design of the COBRA magnet

The schematic view of the COBRA magnet is shown in Fig. 3.5 along with other detector components. Fig. 3.6 shows the layout of the coils in the magnet with their dimensions. The COBRA magnet consists of a main superconducting magnet and a pair of compensation coils which is adopted to reduce the stray magnetic field around the photon detector. The superconducting magnet consists of five coils with three different radii; one central coil, two gradient coils, and two end coils. A resistive (i.e. non superconducting) cable will be used for the compensation coil.

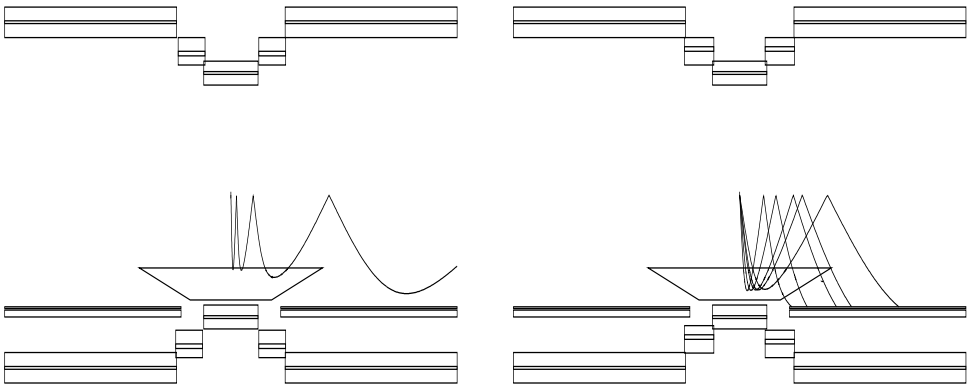

Figure 3.3: Advantages of a gradient magnetic field:
(a) $r - z$ view of the COBRA spectrometer shown with the trajectory of a particle emitted at 88°. The particle is swept away much more quickly than in Fig. 3.2(a).
(b) Trajectories of monochromatic particles emitted at various angles. The bending radius is independent of the emission angle.

The magnet is designed to form a gradient magnetic field so as to achieve the good features of the positron spectrometer such as the constant bending radius of the positrons and the quick sweep of the positrons.

The parameters of the COBRA magnet are listed in Table 3.1, whereas Fig. 3.7a shows the contour plot of the magnetic field distribution produced by the COBRA magnet. The field intensity along the magnet axis is shown in Fig. 3.7b. The performance of the spectrometer and the stray field around the photon detector were optimized by adjusting the diameter, length, and current density of the coils. The five superconducting coils are connected in series and the current density of the coil is controlled by changing the density of the cable winding and operating current, as summarized in Table 3.1. A detailed description of the COBRA magnet can be found in [31].

3.2.2 Development of the superconducting cable

A high-strength aluminum-stabilized superconducting cable was developed for the COBRA magnet. Fig. 3.8a shows the cross-sectional view of the cable. The cable consists of NbTi multi-filament embedded in a copper matrix and an aluminum-stabilizer. The aluminum-stabilizer is mechanically reinforced by "micro-alloying" technology. The aluminum-stabilizer can be reinforced by adding small amounts of metals such as nickel, magnesium, and copper while keeping the electrical resistivity as low as possible [32]. Some 5000 ppm of Nickel are added to the aluminum-stabilizer in the superconducting cable for the COBRA magnet.

The performance of the superconducting cable was measured around 4 K. The parameters of the superconductor are summarized in Table 3.2. An overall yield strength of the cable was found to be above

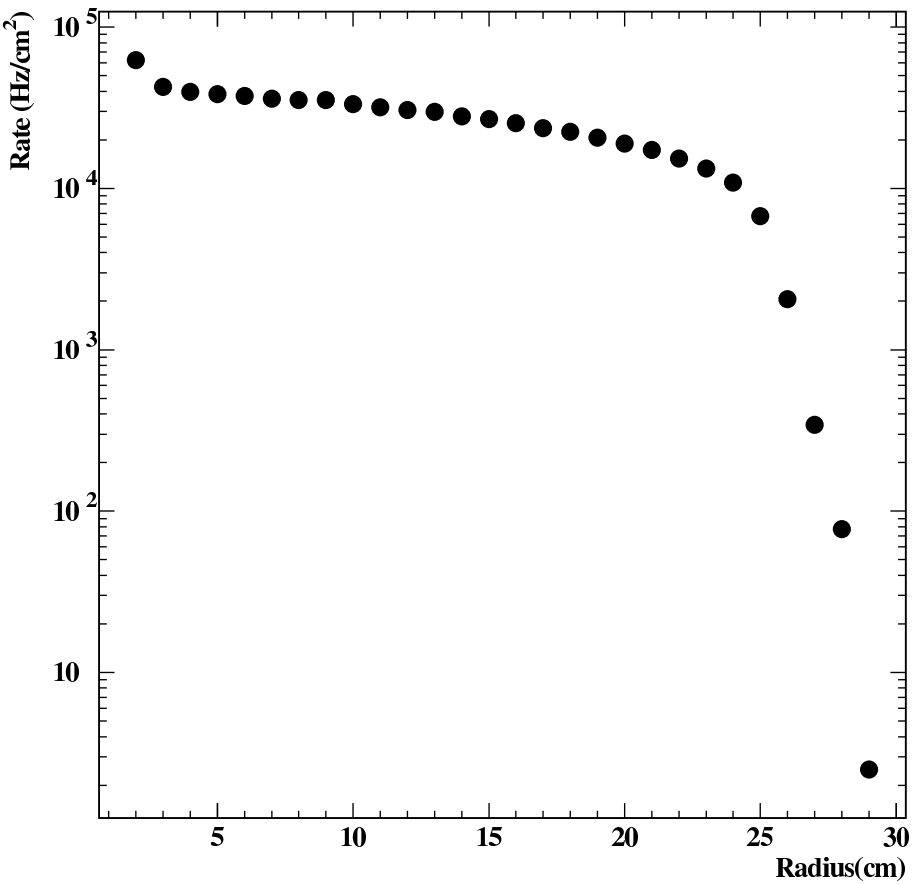

Figure 3.4: Rate of Michel positrons per cm^2 per second as a function of radius assuming a muon decay rate of 1×10^8/s.

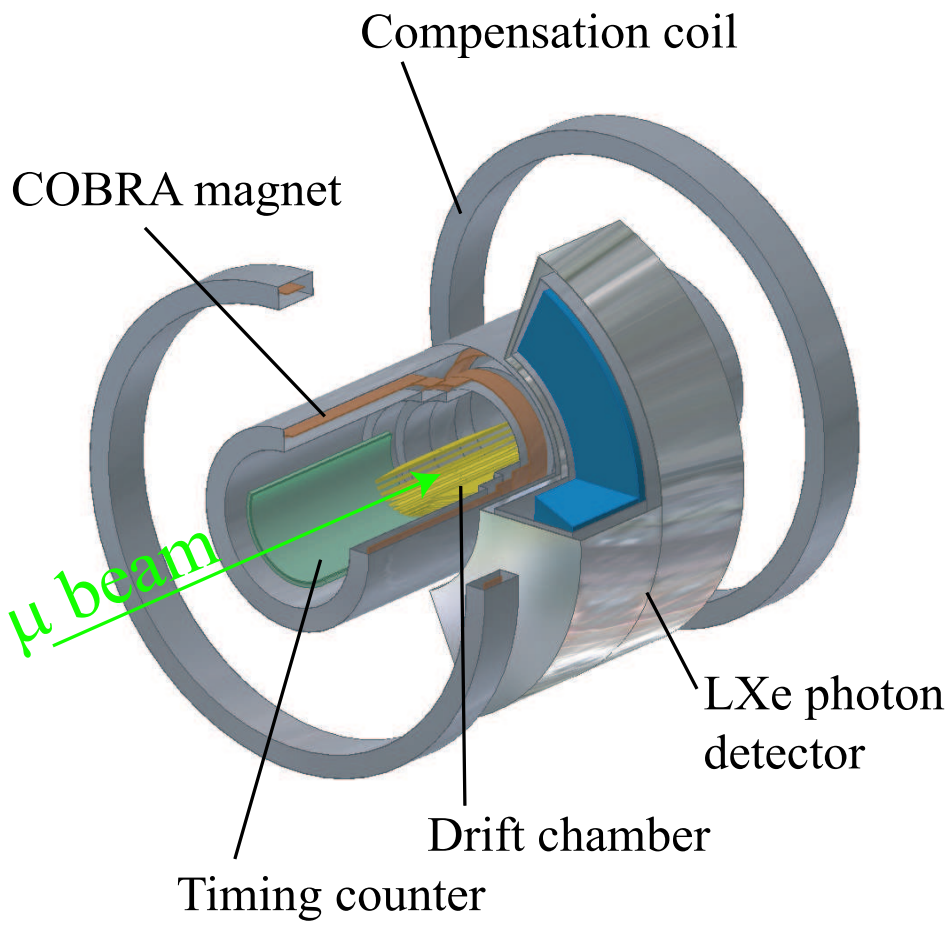

Figure 3.5: Schematic view of the MEG detector with the COBRA magnet and the compensation coils.

220 MPa at 4.2 K while keeping the Residual Resistivity Ratio (RRR)[1] above 280. The characteristics of superconductivity were also measured. Fig. 3.8b shows the measured critical current as a function of the applied magnetic field. The operating current will be 360 A and the peak value of the magnetic field is 1.7 T in the central coil. The load line of the COBRA magnet with the operating point is also shown in Fig. 3.8b. Since the operating temperature of the coil is estimated to be about 5 K, this figure indicates that the performance of the cable has a safety margin of about 30% compared to the operating condition of the COBRA magnet.

3.2.3 Suppression of the stray field

The stray field from the superconducting magnet could degrade the performance of the liquid Xenon photon detector because the PMT gain rapidly drops as the strength of the applied magnetic field increases. Fig. 3.9 shows the relative output of the PMT foreseen to be used in the liquid Xenon photon detector

[1] Ratio of the bulk resistivity at room temperature to the normal conducting resistivity at 4 K

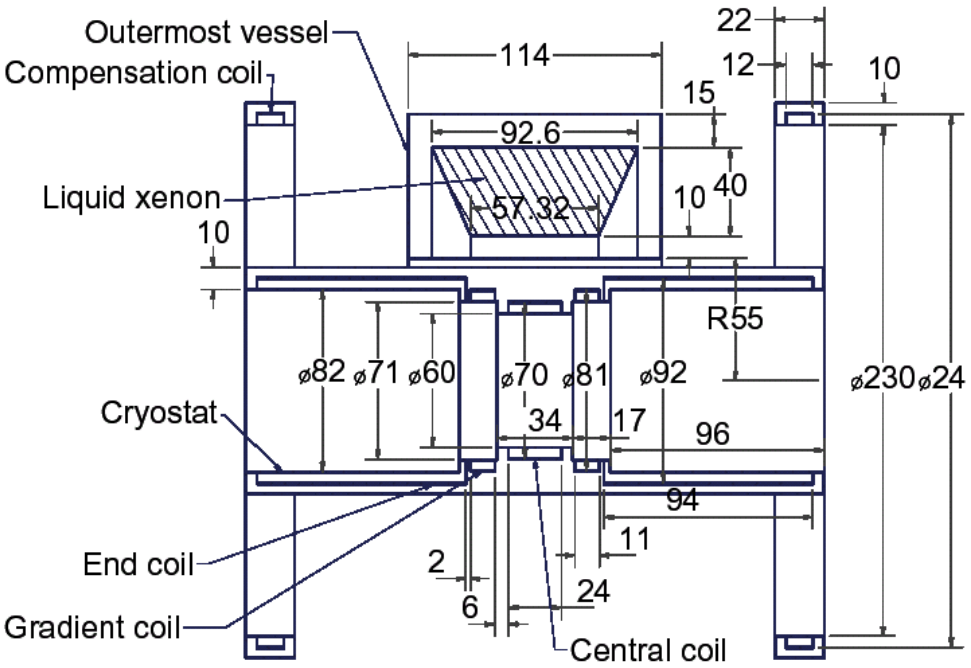

Figure 3.6: Layout of the COBRA magnet with the compensation coils.

Coil	Central	Gradient	Inner end	Outer end	Compensation
Conductivity	Super	Super	Super	Super	Resistive
Inner dia. (mm)	700	810	920	920	2210
Outer dia. (mm)	712.4	820.6	929.5	929.5	2590
Length (mm)	240.3	110.4	189.9	749.2	265
Layers	4	4	3	3	14
Winding	edge-wise	edge-wise (1st) flat-wise (2nd-4th)	flat-wise	flat-wise	double pancake
Inductance(H)	1.64	0.62	0.35	2.29	0.54
I_{op}(A)	360	360	360	360	360
Energy E (kJ)	106	40	23	148	35
Weight M (kg)	9	4	7	28	1620
E/M (kJ/kg)	11.8	10.0	3.3	5.3	0.02

Table 3.1: Parameters of the COBRA magnet.

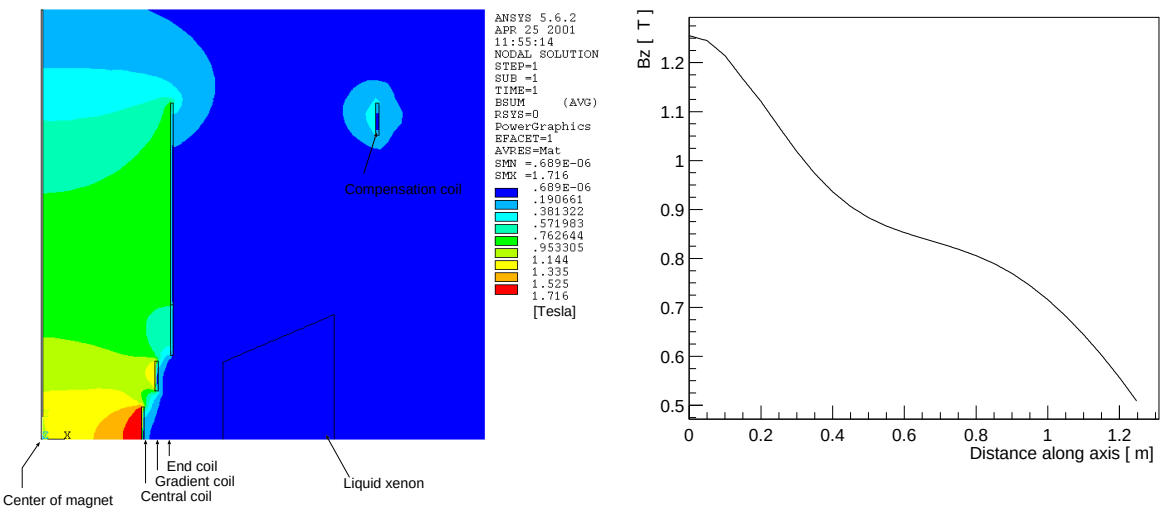

(a) (b)

Figure 3.7: (a) Contour plot of the magnetic field produced by the COBRA magnet; (b) Magnetic field intensity along the magnet axis.

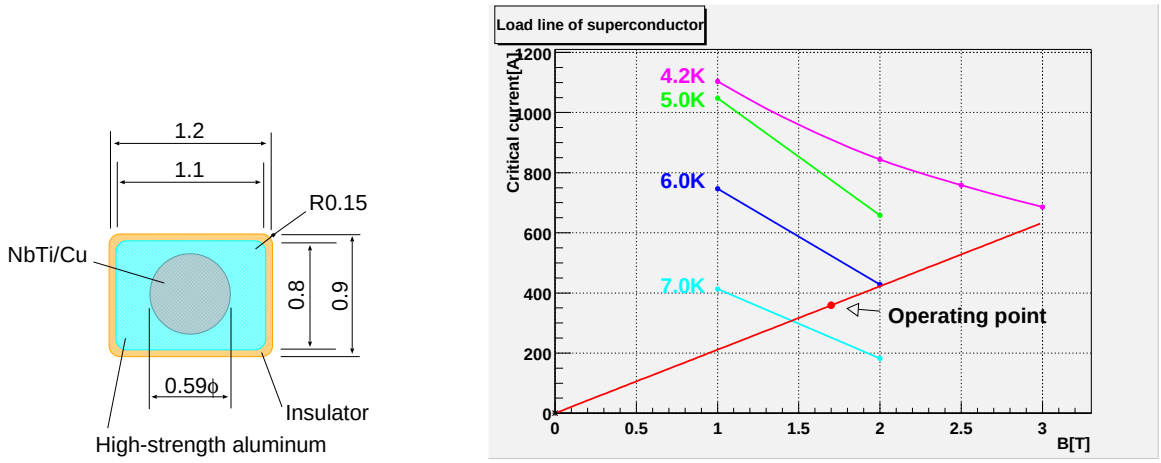

(a) (b)

Figure 3.8: (a) Cross-sectional view of the high-strength aluminum-stabilized superconducting cable developed for the COBRA magnet. (b) Measured critical current as a function of the applied magnetic field. The load line and operating point for the COBRA magnet are also shown.

Conductor material	NbTi/Cu
NbTi/Cu diameter	0.59 mm
NbTi/Cu Cu ratio	0.82
Insulator	Kapton polyimide tape
Overall cross section	0.8×1.1 mm^2
Overall cross section with insulator	$0.9 \times 1.2\,$mm^2
Critical current density	5476 A/mm^2 at 4.2 K, 2.0 T
Critical current	851 A at 4.2 K, 2.0 T 666 A at 5.0 K, 2.0 T
RRR	Cu 55.9 Al 280
0.2% yield strength (conductor)	598 MPa at 4.2 K
0.2% yield strength (Al stabilizer)	105 MPa at 4.2 K
0.2% yield strength (overall)	221 MPa at 4.2 K

Table 3.2: Parameters of the superconducting cable developed for the COBRA magnet.

(HAMAMATSU R6041Q) as a function of the magnetic field [33] where the z-axis is defined as the PMT axis. The tolerance to the magnetic field of the PMT strongly depends on the direction of the applied magnetic field compared to the tube axis. There is a strong dependence even on the direction on the photo-cathode plane due to the structure of the dynodes. The maximum allowed strengh of the magnetic field is 150 Gauss and 50 Gauss respectively for the perpendicular and parallel directions to the tube axis. The maximum allowed strength is defined as the field strength which reduces the relative gain of the PMT by 50%. Therefore, the stray field should be reduced down to the 50 Gauss level in the vicinity of the photon detector.

At an early stage of the design work on the COBRA magnet we had investigated the shielding of the stray field by using an iron return yoke. It was not, however, possible to suppress the stray field below the acceptable level mainly due to the local leakage field coming from the step structure of the magnet. Another demerit of the return yoke is that a large amount of iron is necessary so that the electromagnetic forces between the COBRA magnet, beam transport magnet, and yoke have to be carefully managed.

We currently adopt an active shielding of the stray field by using a pair of compensation coils as described in Section 3.2.1. The direction of the operating current for the compensation coil is the same as that for the main magnet. The magnetic field around the photon detector can be canceled effectively by the compensation coils. Fig. 3.10 shows the contour plot of the magnetic field produced by the COBRA magnet with the compensation coils. The residual field is small over the whole photon detector region.

Fig. 3.11 shows the profile of the magnetic field at the PMT position. The component of the magnetic field parallel and perpendicular to the PMT axis are separately shown. Note that the PMTs on the side wall of the calorimeter are arranged so that the axis is parallel to the magnet axis. The maximum allowed strength for each component is also shown by dashed lines. It can be seen that the field strength at the PMT position is well below the acceptable level.

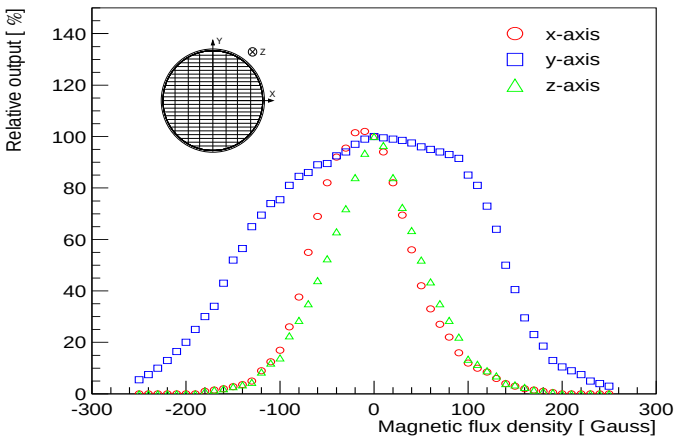

Figure 3.9: Relative output of the PMT to be used in the photon detector as a function of the applied magnetic field [33]. The z-axis is defined as the PMT axis here.

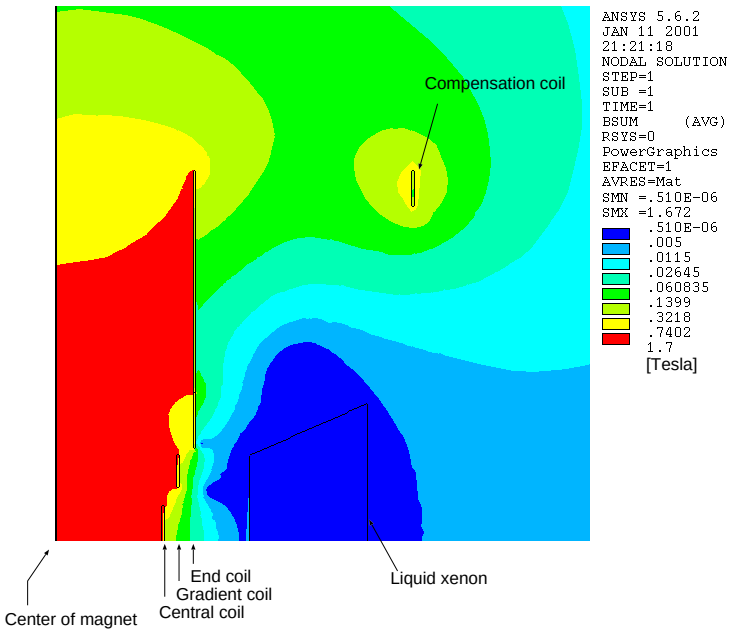

Figure 3.10: Contour plot of the residual magnetic field. A box in the photon detector region shows the boundary where the PMTs are arranged. Note that the contour interval is not linear.

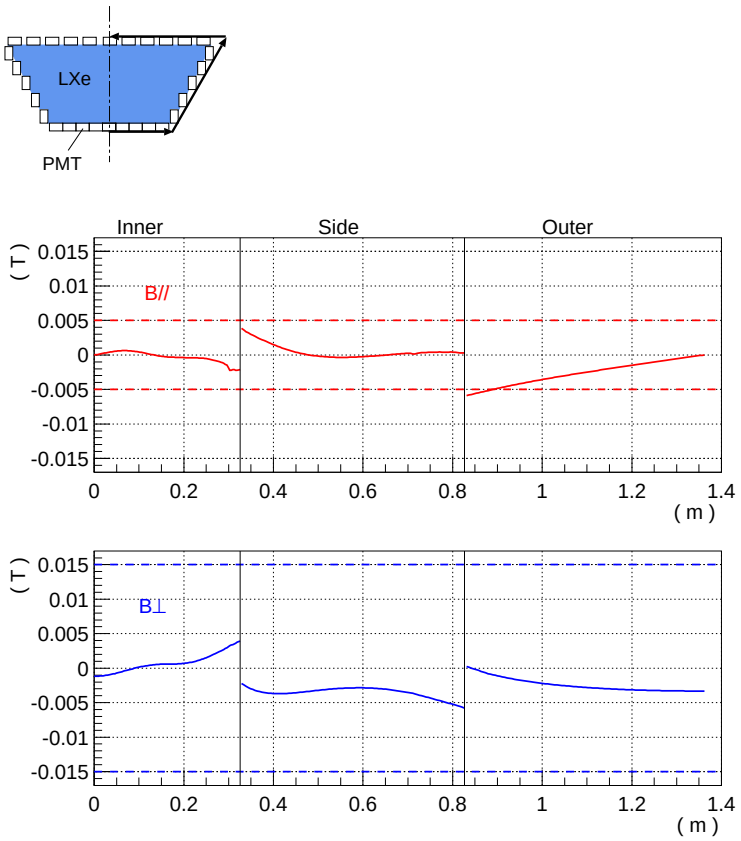

Figure 3.11: Magnetic field intensity along the boundary path of the liquid Xenon photon detector where the PMTs are arranged. The top (bottom) figure is the profile of the component parallel (perpendicular) to the tube axis. The maximum allowed levels are also drawn with dashed lines. The horizontal axis shows the length from the point of $z = 0$ cm and $r = 62$ cm along the boundary path (as shown in the inset) right outside the PMT array wall on the horizontal plane including the magnet axis. It is measured up to the point of $z = 0$ cm and $r = 108$ cm.

	Axial force (ton)	Hoop stress (MPa)
Central coil	13.1	66
Gradient coil	4.2	53
End coil	15.3	46

Table 3.3: Electromagnetic force acting on the coil.

3.2.4 Mechanical design of the COBRA magnet

Fig. 3.12 shows the coils, the support shell of the coils and the cryostat. This design was optimized by detailed mechanical calculations and related experimental tests which will be described here.

Table 3.3 shows the calculated electromagnetic force acting on each coil. The stress due to the electromagnetic force is maximized around both edges of the support shell of the central coil. In order to reduce the stress around that region, a thin support cylinder is placed over the central coil (bypassing support) as shown in Fig. 3.12. The shape and thickness of the support shell and bypassing support were optimized to make the mechanical stress acceptable for the materials used in the magnet. Fig. 3.13 shows the calculated stress distribution around the central coil and bypassing support. The result indicates that the maximum stress is 74 MPa at the edge of the support shell for the central coil which is well below the maximum allowed stress, 100 MPa at 4 K for the aluminum (A5083P) to be used for the support shell.

Various mechanical tests for some essential parts in the magnet are being performed to verify the validity of the current design of the magnet [31].

3.2.5 Transparency of the magnet

Due to the the high-strength superconductor developed for the COBRA magnet, we can minimize the thickness of the support structure required for a given electromagnetic force acting on the coils. The components used in the coil and cryostat of the magnet within the acceptance of the photon detector are listed together with their thicknesses in Table 3.4. In order to minimize the operating current the superconducting cable was wound in the "edge-wise" way in the central coil instead of the usual "flat-wise" way. These two kinds of ways to wind the cable are illustrated in Fig. 3.14. A stronger central field can be obtained with a lower operating current using an edge-wise winding at the cost of a slight increase in thickness ($2.6 \times 10^{-2} X_0$).

3.3 Chamber System

Positron tracks are measured with 17 drift chamber sectors aligned radially at 10° intervals in azimuthal angle. Each sector consists of two staggered arrays of drift cells, as shown in Fig. 3.15. The sensitive area of the chamber extends from a radius of 19.3 cm to 27.0 cm. In the z direction the active region extends up to $z = \pm 50$ cm at the innermost radius and $z = \pm 21.9$ cm at the outermost. Positrons of 52.8 MeV/c emitted from the target with $|\cos\theta| < 0.35$ and $-60° < \phi < 60°$ are covered by this geometry.

This staggered-cell configuration allows us to measure the r-coordinate and the absolute time of the track simultaneously. The difference between the drift times $(t_1 - t_2)$ in the adjacent cells gives the r-

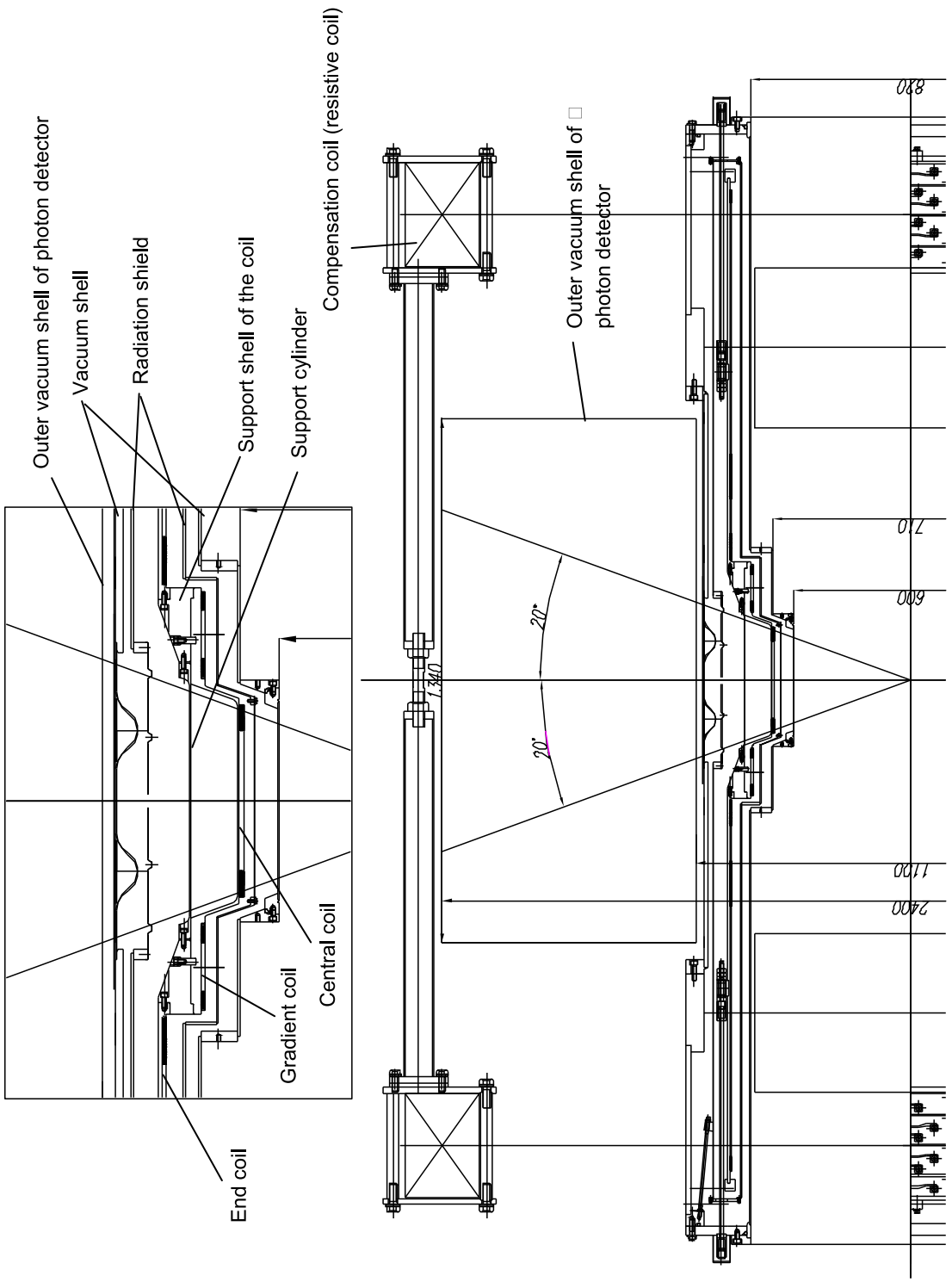

Figure 3.12: Design of the coil and cryostat of the magnet.

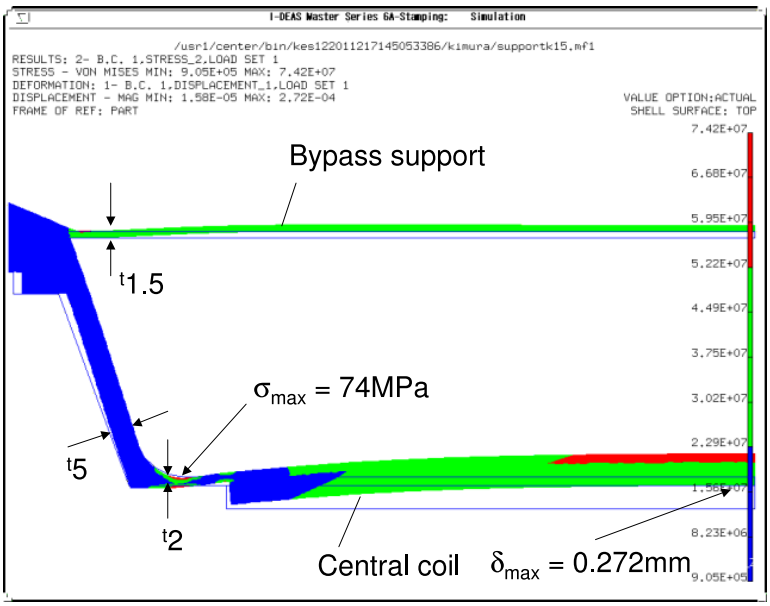

Figure 3.13: Stress distribution around the central coil of the magnet.

	Equivalent thickness (g/cm^2)	Radiation thickness (X_0)
Coil		
Conductor (Al)	0.745	0.0312
Conductor (NbTi/Cu)	0.868	0.0766
Insulation (Uplex/G-Epp)	0.069	0.0020
Epoxy-resin	0.058	0.001
Support cylinder	0.945	0.0396
Pure Al strip	0.068	0.003
Subtotal	2.753	0.153
Cryostat		
Outer vacuum shell	0.405	0.017
Radiation shield	0.162	0.007
Inner vacuum shell	0.405	0.017
Super insulation	0.105	0.003
Subtotal	1.192	0.048
Total	3.83	0.197

Table 3.4: Transparency of the COBRA magnet.

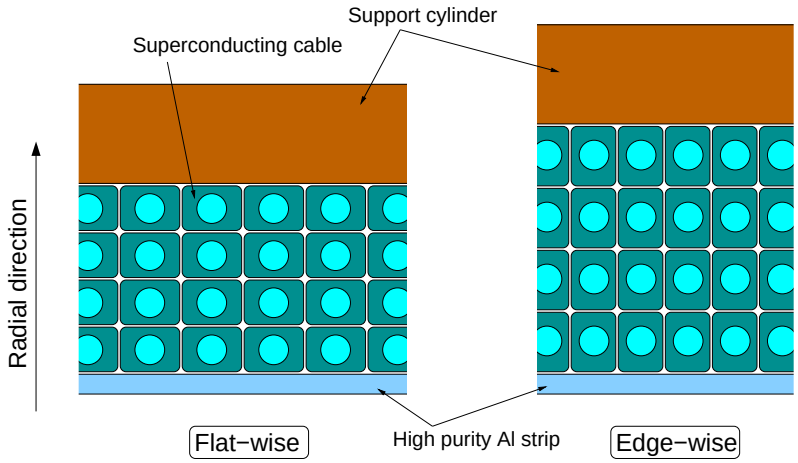

Figure 3.14: Flat-wise and edge-wise winding.

coordinate of the track with $100 \div 200$ μm accuracy, while the mean time $(t_1 + t_2)/2$ gives the absolute time of the track with ~ 5 ns accuracy. This excellent timing resolution is important for the pattern recognition.

By the ratio of charges observed at both ends of a sense wire the z-coordinate along the wire can be initially located with an accuracy of ~ 1 cm. The chamber walls are made of thin plastic foils. A thin layer of aluminum deposit on the four cathode foils is shaped to make a Vernier pattern as shown in Fig. 3.18 (middle). By a comparison of the charges induced on the two sets of Vernier pads of each cell (see also Section 3.3.1) it is possible to determine the z position with an accuracy of about 300 μm [34].

We plan to read each of the sense wires and the Vernier pads with a 100 MHz digitizer (see Section 5.4).

The chamber sectors and the volumes between them are filled with 50% He – 50% C_2H_6 gas mixture at 1 atm. Such a mixture is chosen to have sufficient ionization loss in the gas ($\sim 65\, e^-$/cm for minimum ionizing particles) as well as to minimize multiple Coulomb scattering of tracks ($X_0 \sim 650$ m). This mixture has proven to work well in several existing experiments like BELLE [35] and BaBar [36]. The drift velocity saturates at roughly 4 cm/μs for a relatively low electric field (~ 1.5 kV/cm) [37]. Other gas candidates are however being investigated.

Momentum and angular resolutions are primarily limited by multiple scattering in the gas and chamber materials. The position resolution of the chambers does not contribute much as long as it is less than 300 μm.

Fig. 3.16 shows the structure of a chamber sector. In the present design a foil of Kapton, 12 μm thick, is stretched between two end-plates, which might be honey-comb structures made of thin plates of plastics and G10. An array of sense and potential wires are also strung between the end-plates. Each end-plate is fixed to an aluminum plate of a narrow cylindrical shape, which is then fixed to the inner wall of the magnet cryostat.

3.3.1 Drift Chambers R&D

To obtain information about the performance of the proposed chambers, two test prototypes were built.

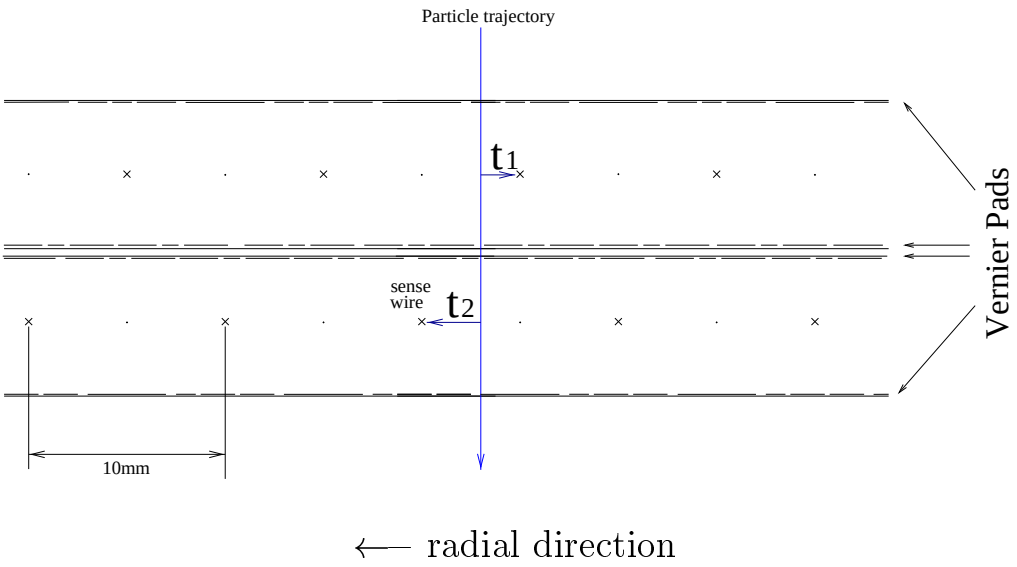

Figure 3.15: Cross-sectional view of a part of a chamber sector. It consists of two layers of drift cells staggered by half-cell.

The first one in Tokyo [38], a classical square-framed construction, which demonstrated that the required precision is, in principle, achieved using β-particles from a ^{90}Sr source (Table 3.5). Those measure-

Resolution	method	Tokyo prototype
σ_r	drift time measurement	$100 \div 150$ μm
σ_z	Vernier cathode measurement	425 μm
σ_z	charge division measurement	2 cm
σ_t	drift velocity and drift time	$4 \div 12$ ns

Table 3.5: Various resolutions achieved in the Tokyo test of the Drift Chamber prototype; for the measurement conditions see [38].

ments also proved that the necessary gas gain could be obtained for a variety of candidate gas mixtures.

The other prototype, built at PSI [39] (8 cm in length for the longer $z-$side) has tested the mechanical solution of an open-framed chamber (without a frame on the target side) and confirmed the ^{90}Sr results of the Tokyo measurements. The position resolution in the radial direction obtained over a complete drift-cell is shown in Figure 3.17, resulting in 120 μm at the centre, for a high voltage of 1900 V and (50 : 50) by volume Helium-Ethane gas mixture. The corresponding time resolution was found to vary between 5 and 12 ns over the drift-cell.

This prototype chamber was successfully operated in a 1 Tesla magnetic field using beam particles (elecrons, pions and muons) in a test in the πM1 area at PSI.

The following sections describe how the parameters of the final chamber will be optimized using

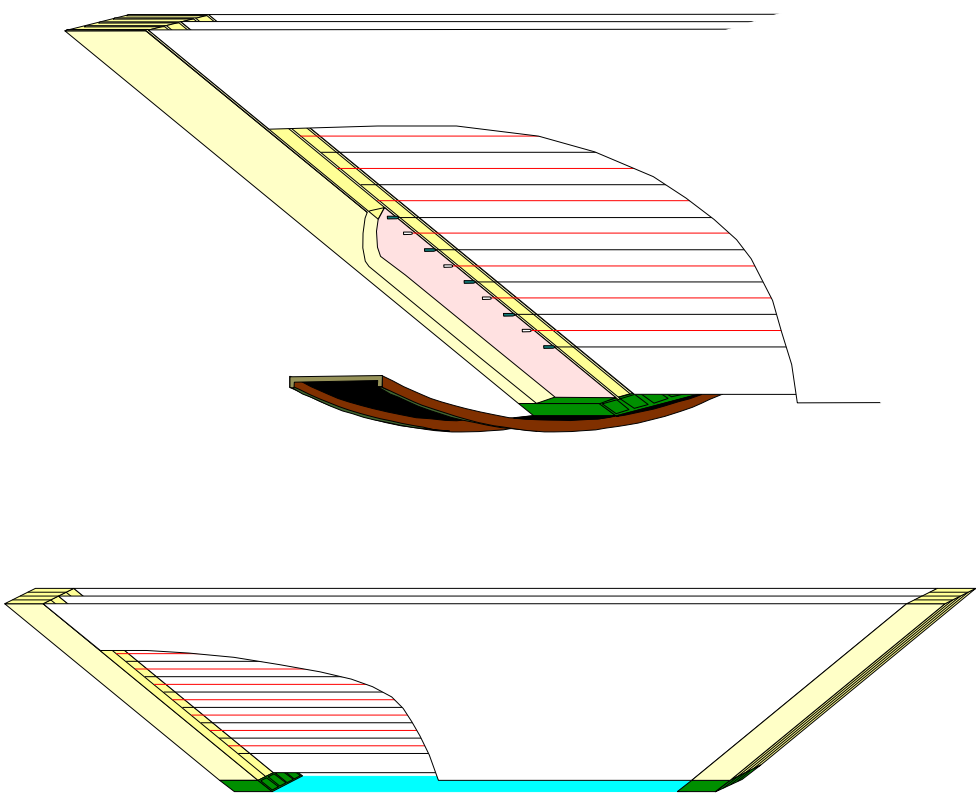

Figure 3.16: A sector of the drift chamber seen from the side. The end-plates stretching wires and foils are schematically shown.

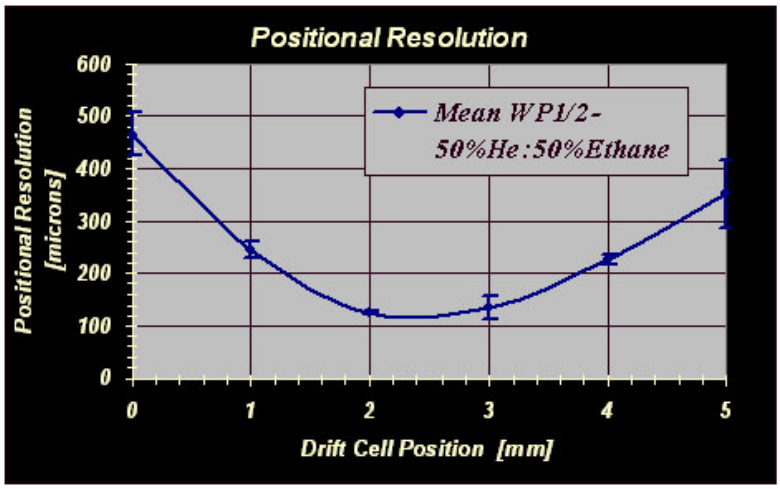

Figure 3.17: Position (drift) resolution in μm measured across a drift-cell of the PSI mini-prototype chamber, using a ^{90}Sr source and a scintillator telescope, as well as a double collimator system. A (50 : 50) in volume Helium-Ethane gas mixture, at a high voltage of 1900 V, was used.

two types of test chambers currently under construction. The first, the so-called "Double cathode" test chamber and the second, the "Charge division" test chamber, which will be used to optimize the position resolution along the wire. It is also described how a 1 : 1 version of the cathode structure will be built to optimize the Vernier geometry and to train the construction of the most critical part of the drift chamber.

Double Cathode Test Chamber

Initially [10] a structure with a triple-strips Vernier cathode deposited on the two external foils of each chamber layer and a common cathode in the middle was envisaged. This solution is however not homogenous in position sensitivity. A Monte Carlo simulation (Figure 3.18) showed that a replacement of the middle common cathode by two separated double-strip cathodes for each chamber layer, only minimally affects the momentum resolution and the efficiency. This solution will therefore allow the use of the same double-strip Vernier cathode (Figure 3.18) for each of the planes, shifted by a quarter of the Vernier period relative to each other: this way the half-period ambiguity can be resolved and the homogeneity of the position sensitivity is restored. A complete R&D programme will soon start with four small square chambers (each of three, 6 cm long, cells) equipped with cathodes as described above. This simple structure makes it easy to test different cathode structures (produced as prints on a 100 μm kapton foil). The size of these chambers is small enough to fit into a dipole magnet for measurement at 1 Tesla. The number of chambers allows an auto-calibration of the position resolution, using either cosmic muons without a magnetic field or beam particles in a constant field. This set-up will enable the behaviour and gas properties in the magnetic field to be studied and the optimization of a number of chamber parameters such as the distance between the two middle cathodes (as a large capacity might induce cross-talk between cathode foils thus affecting the read-out) and the optimal period of the Vernier structure, while the tails in the position and

timing distributions will be measured as a function of efficiency and rate.

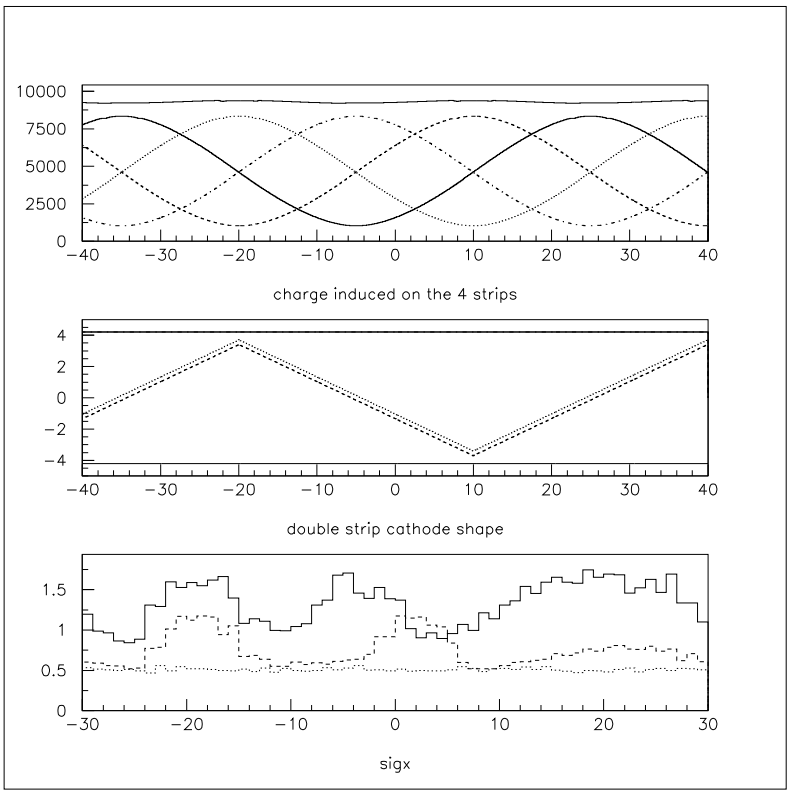

Figure 3.18: Results of a Monte Carlo simulation of the Vernier cathode pattern. With the shape of the double-strip cathode, as shown in the middle picture, the four induced charge dependences shown in the upper picture are obtained. The lower figure shows a comparison of the position resolution for the two double-strip cathodes (dotted line) with that of two versions of the triple-strip cathode: (solid and dashed line). The horizontal axis shows the distance along the wire (mm), while the vertical axis shows the resolution in arbitrary units.

Various materials and techniques to seal the chambers externally with glue (e.g. THREE BONDS 1350) have been studied; such solutions, which would dramatically simplify the construction of the chambers and significantly reduce the costs, will be tested on the small chambers.

Charge Division Test Chamber

A 1 m long, rectangular chamber with three anode wires, equipped with the same prints and electronics as the "Double cathode" test chamber is almost ready and will be used to optimize the anode read out. It will also allow the comparison of different wire materials (e.g. Steel, 1200 Ω/m resistivity, tungsten, 330 Ω/m etc.). The shape of the cathode on the open-frame side has also to be studied. It was found that a lengthening of the chamber, towards the target, by adding a dummy cell, simplifies the construction

and ensures a non-distorted electric field configuration in the active volume. As far as possible, the use of support structures, which would increase multiple scattering and create dead regions, will be avoided. To get the necessary strength, the 12 μm thick cathode foil will be pre-tensioned and inhomogenously deformed. This deformation must be measured and, if necessary, create cathode structures which are not uniform in their original free state but uniform once mounted. For this reason the highest priority will be placed on making a practical final design of the cathode mounting tools and of the cathode supporting frames (hood), with the goal of ordering these parts before the remaining parts of the first 1 : 1 prototype.

3.3.2 Pattern Recognition

Fig. 3.19 and 3.20 show examples of simulated $\mu^+ \to e^+\gamma$ events with accidentally overlapping Michel decays occurring at an average of 1×10^8/s.

With our constant-radius spectrometer most of the low energy Michel positrons curl up with small bending radii and do not touch the drift chamber cells. Hit rates in outer drift cells are particularly low, as shown in Fig. 3.4. Highest momentum positrons reach the outer drift cells, where the direction of the trajectories is almost perpendicular to the drift direction. A simple sum of the drift times $(t_1 + t_2)$ measured by the staggered cells then determines the absolute positron timing with a 5 ns accuracy (see Section 3.3).

A strategy of the offline reconstruction of tracks can be the following: we start from the hits in outer cells by picking up pairs of hits in adjacent staggered cells with the sum of the drift times close to the maximum drift time. Most of hits produced by accidental tracks are off timing and thus will fail to satisfy this condition.

The hits surrounded by circles in the figures are those satisfying this timing condition. It is found that the 52.8 MeV/c track of the positron from $\mu^+ \to e^+\gamma$ always results in three or four sectors having a pair of hits satisfying the condition, while it is rarely the case for accidental tracks. We start from these hits and extrapolate the track toward smaller radii.

In the extrapolation process some hits at inner radii might be unusable by overlap of accidental hits. Simulation studies have shown that more than 90% of tracks have only zero or one hit lost by the overlap events.

The probability of picking up wrong hits at inner radii is found to be small, since each hit-point carries the 3-dimensional information which is especially accurate in the z direction, namely ~ 300 μm compared with the 1 m span of the sense wire. Lower figures of Figure 3.19 and 3.20 show the events in $x - z$ view, i.e. seen from the top of the detector. It is evident that individual tracks can be identified with the 3-dimensional information.

The present design of the chamber layout and the pattern recognition procedure will allow us to cover about 10% of the highest momentum window. This should be enough to determine the momentum resolution function from the real data.

3.3.3 Tracker Resolutions

Momentum and angular resolutions of the spectrometer are limited by multiple scatterings in the gas and the chamber material. As mentioned in Section 2.2, the central region inside the magnet is filled with pure helium (Figure 3.21) in order to minimize the amount of material in front of the tracking chambers.

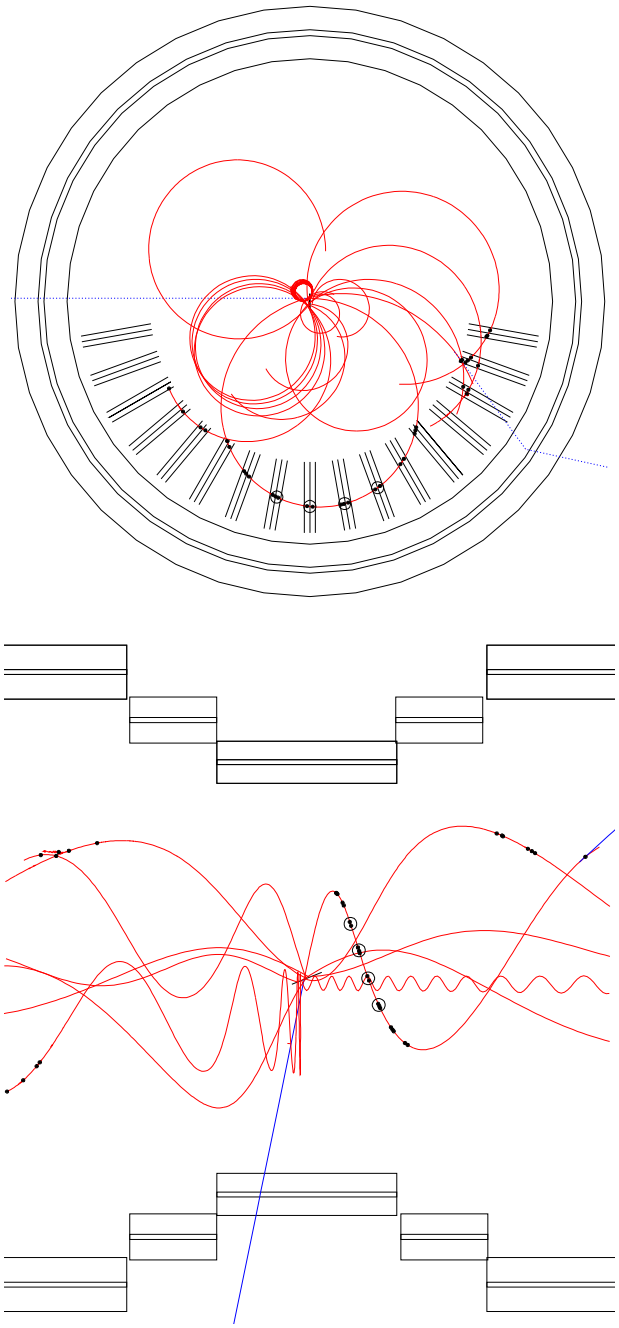

Figure 3.19: The $r-\phi$ view (upper figure) and the top $(x-z)$ (lower figure) of a typical simulated $\mu^+ \to e^+\gamma$ event with accidental pile-up of Michel positrons. The positron from the $\mu^+ \to e^+\gamma$ decay is seen as the track with a large radius at the bottom of the $r-\phi$ view. Points within a circle are a pair of hits in adjacent staggered cells which satisfy the timing condition, as explained in the text, and are used as a starting point of pattern recognition.

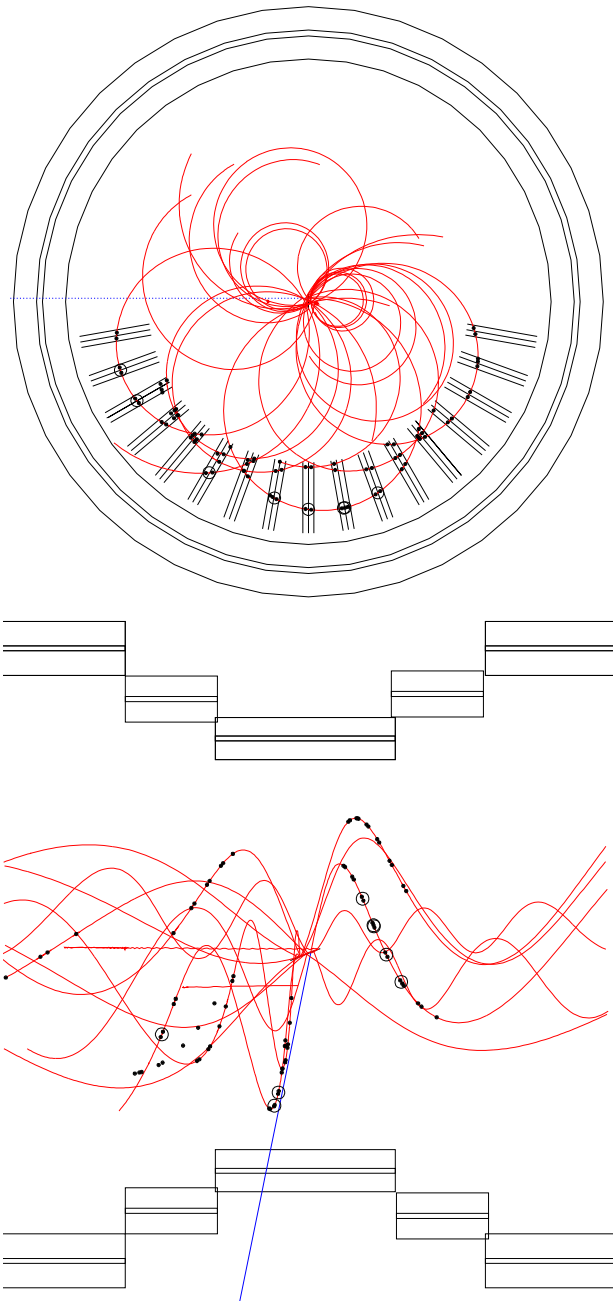

Figure 3.20: The $r-\phi$ view (upper figure) and the top $(x-z)$ view (lower figure) of a simulated $\mu^+ \to e^+\gamma$ event with accidental pile-up of Michel positrons. Individual tracks can be clearly identified with the 3-dimensional information carried by each hit-point.

The expected resolutions of the spectrometer have been studied with GEANT simulations by incorporating detailed material distributions. Positrons of 52.8 MeV/c were generated and their trajectories were reconstructed by using several methods. Depending on the different method used the momentum resolution obtained ranges from 0.7% to 0.9% (in FWHM) and the angular one from 9 to 12 mrad (in FWHM). The momentum resolution is comparable with the MEGA design value, whereas the positron origin on the target can be reconstructed with a resolution ranging from 2.1 to 2.5 mm.

3.4 Timing Counter

This detector is designed to measure the positron timing with a resolution of 100 ps FWHM and to be used in the trigger for selecting events containing a positron coincident in time and collinear in direction with a photon identified in the electromagnetic calorimeter.

Hodoscope arrays of plastic scintillators are placed on both sides of the positron spectrometer to provide the positron timing and trigger signal.

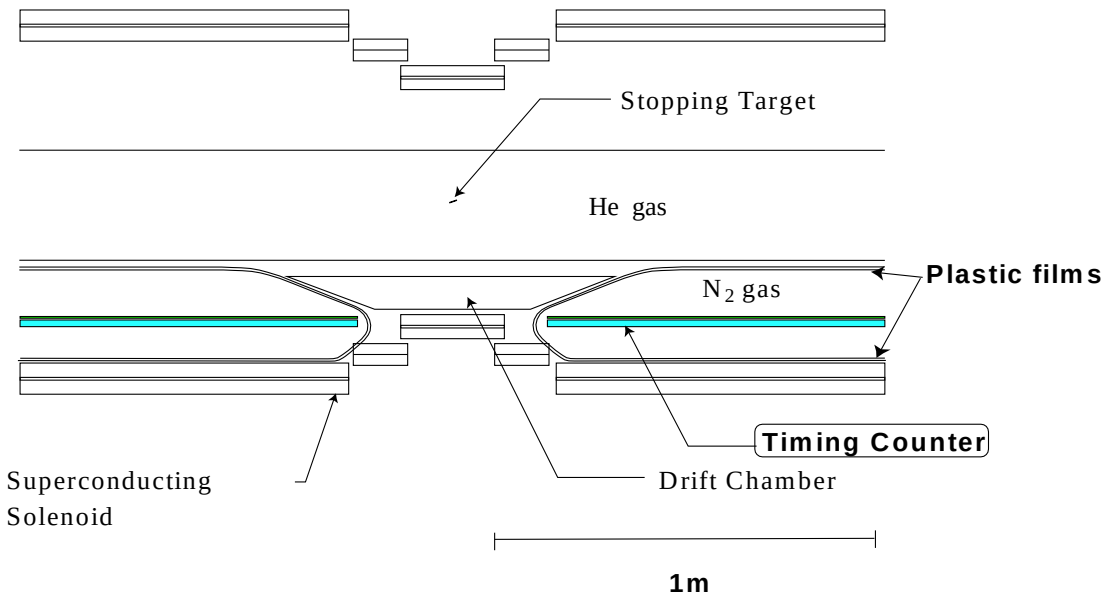

Figure 3.21: The present layout of positron timing counters

Figure 3.21 shows the present design of the layout. The timing counter arrays are placed at a radius of 29.5 cm, covering 145° in ϕ and $25 < |z| < 95$ cm. The $\mu^+ \to e^+\gamma$ positrons emitted in the angular range $0.08 < |\cos\theta| < 0.35$ are incident on the timing counter after completing ~ 1.5 turns in the $r - \phi$ plane.

The multiple scattering effect on the positron timing was investigated by using the Monte Carlo simulation. The sigma of the time spread introduced by the multiple scattering is about 20 ps, negligible when compared to the detector resolution.

Figure 3.22 shows the configuration of the timing counters, which consist of two layers of scintillator hodoscopes (composed of ~ 5 cm wide scintillator bars) orthogonally placed along the ϕ and z directions, respectively. The outer layer will be used for timing measurement while the inner one will serve mainly for triggering purposes. The scintillators which compose each layer can have a slant shape, so that a positron incident on the hodoscope crosses two or three adjacent scintillators. The pulse-height ratios among these adjacent scintillators will provide an information on the impact point with accuracy better than ± 1 cm in z and ± 3 cm in ϕ directions. Each scintillator is viewed on each side by photomultipliers (one per side), which measure the pulse heights as well as the arrival times of the scintillation light (t_L and t_R) at both ends. The time difference $t_L - t_R$ provides another measurement of the impact point along the scintillator (ϕ for the inner and z for outer scintillators), while the mean time $(t_L + t_R)/2$ gives the absolute impact time. We thus have redundant and independent measurements both for the timing and for each coordinate of the impact point.

Other solutions, including optical fibers, for the inner (curved) layer of scintillators are being considered as the light transmission efficiency for the present geometrical configuration might not be sufficient even for triggering purposes.

In order to estimate the accidental hit rate of the scintillators, Michel decay positrons were generated and followed to the timing counters by a GEANT simulation, which showed that 2% of Michel decays are incident on the timing counters placed at each end of the spectrometer. This corresponds to an average counting rate per scintillator bar of 0.1 MHz, resulting in an occupancy of 10^{-3} for a time window of 10 ns.

Photomultipliers have a limited life time in the helium gas. As shown in Figure 3.21, the area surrounding the timing counters will be separated by two layers of metal-coated plastic films from the central region which is filled with helium gas. N_2 gas will flow in between the plastic films embedding the timing counters. Such a system is known to assure a long-enough life time of the PMTs.

First beam tests of this detector prototypes were made at KEK in 1999 [40] and repeated at Pisa in 2001 [41] using cosmic ray muons.

Several timing counter prototypes were built and tested: made of 1 m long BC404 scintillator bars (cross section 5 cm $\times$1 cm), wrapped with 50 μm of aluminized Mylar and coupled to PMTs through light guides at the two opposite ends.

We used Philips XP2020 UR ($2''\phi$, 470 ps transit time spread) or Hamamatsu R5946 fine mesh ($1.5''\phi$, same t.t.s. as the Philips ones) PMTs and tested light guides of different shapes.

The timing properties of these detectors were studied by means of cosmic ray muons. Since the rate of these muons is relatively low and it is necessary to correct for position dependent effects, we set–up a telescope made of eight Micro Strip Gas Chambers [42], four of which had strips at a small angle (5.7°) with respect to the other four, for stereo reconstruction of the muon tracks (see Figure 3.23). The dimensions of each chamber are 10 cm $\times$ 10 cm. The impact point of one muon along the counter prototype was reconstructed with a resolution better than 1 mm.

The muon timing (relative to a reference counter) is independently measured by each of the two PMTs of the counter, after correcting for "time walk" effects. As shown in Fig. 3.24, the weighted average of the two measurements was ≈ 60 ps, independent of the position along the counter. Measurements were also performed by tilting the counter to increase the muon path and energy deposit. We checked that the timing resolution improves as the square root of the total number of photo-electrons.

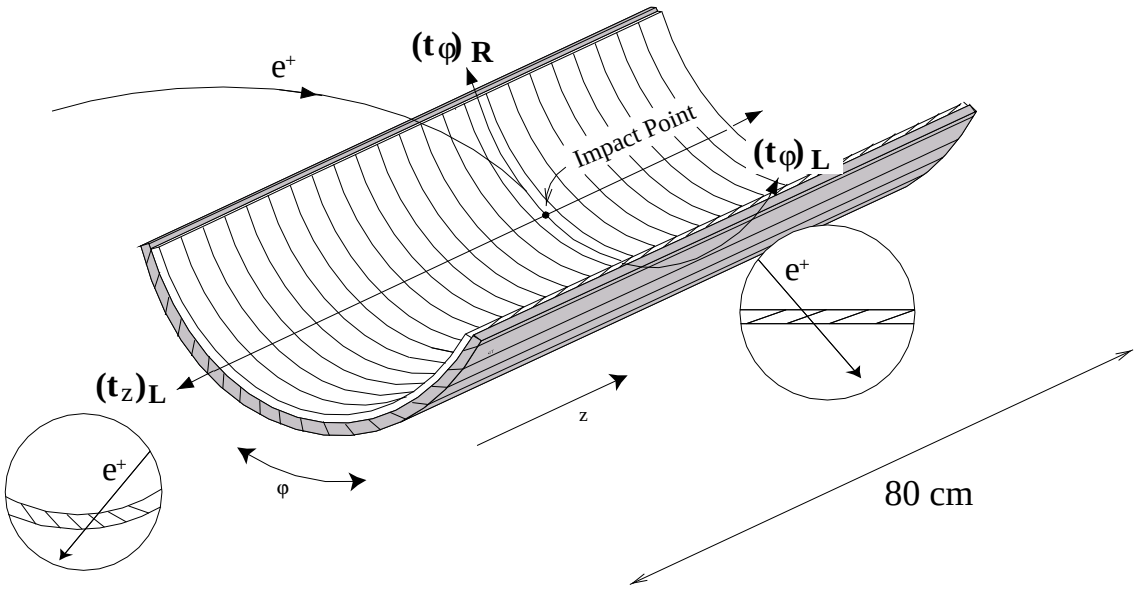

Figure 3.22: The timing counter configuration.

We used a Monte Carlo simulation to take into account the positrons trajectories in the final experiment in order to select the relative position and the thickness of the two layers of scintillator.

A 40 ps timing resolution ($\Delta t_{\rm fwhm} \sim 100$ ps) requires a minimum of 5 MeV energy deposit in the scintillator. A good detector configuration is obtained by using a 0.5 cm inner layer (for triggering purposes) and a 2 cm outer layer (the one for the timing measurement). We evaluate a ~ 94 % positron efficiency for such a detector configuration and a minimum 5 MeV deposit in the layer used for the timing measurement.

The rate in the timing counter due to Michel positrons will be about 2 MHz and should not constitute a problem for the operation of this device. We must obviously take care that other sources of background do not significantly increase the occupancy of this detector.

The engineering study of the timing counter has been started. A 3D mechanical drawing of the detector is shown in Figure 3.25. The axis of the outer layer PMTs can be kept below 10° relative to the direction of the magnetic field lines.

We plan to study the timing resolution of the R5946 PMTs in a high magnetic field environment though similar studies for similar PMTs were already made by other collaborations [43] yielding an insensitivity of the PMT timing response to magnetic fields along the PMT axis up to 1.6 T.

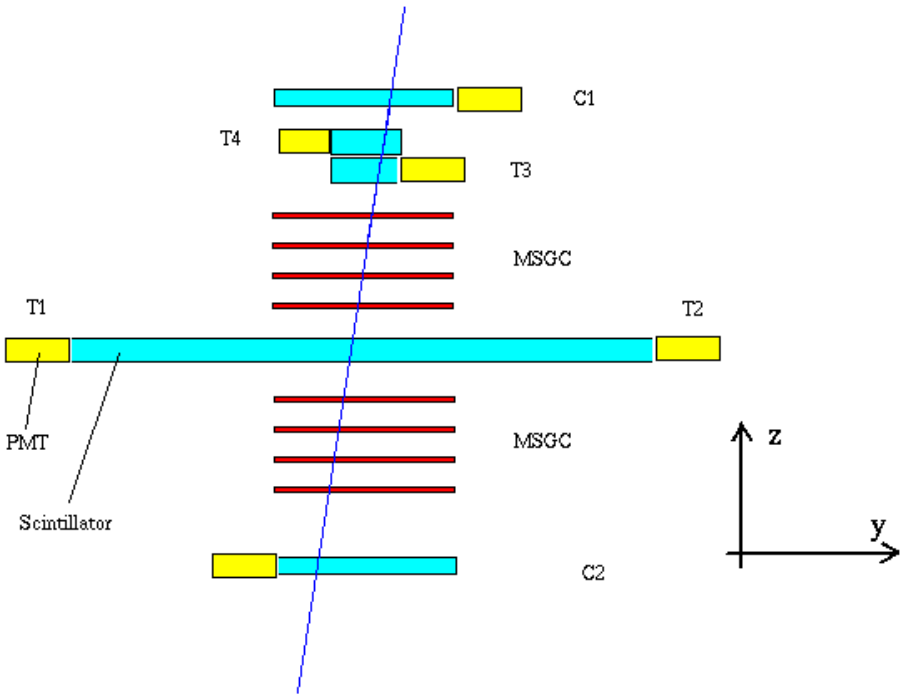

Figure 3.23: Layout of the MSGC tracking system for Timing Counter studies.

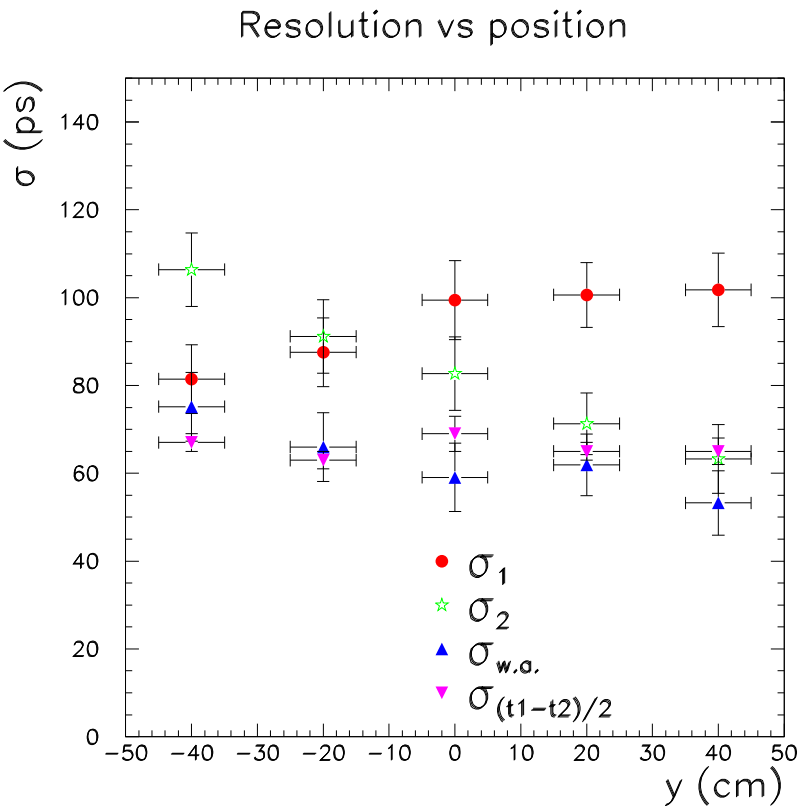

Figure 3.24: Timing resolution along the counter.

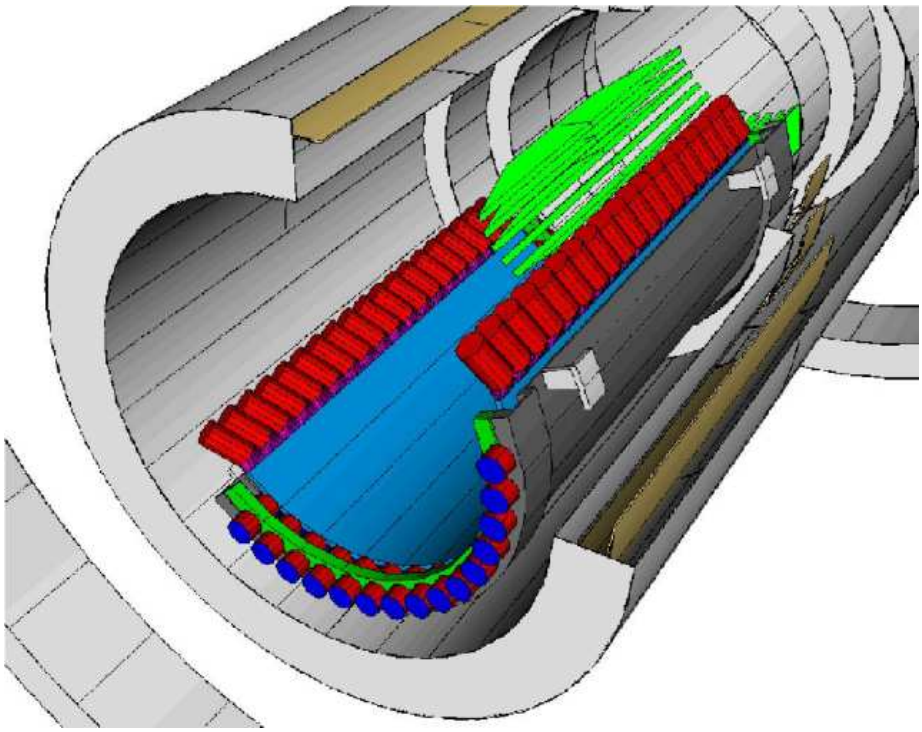

Figure 3.25: Preliminary 3D mechanical drawing of the Timing Counter.

4. The Photon Detector

4.1 General design

We use only the scintillation light from liquid Xenon, and do not attempt to collect the ionization. Liquid Xenon scintillator has a high light yield (comparable to NaI(Tl)) and fast signals which are the most essential ingredients for the precise energy and timing resolutions required for this experiment. Its short decay-time is indispensable to minimize the pile-up of high rate γ-rays. Liquid Xenon is also free from problems of non-uniformity, which limit the energy resolutions of scintillating crystals.

The liquid Xenon properties are summarized in Table 4.1. Two distinct effects determine the optical properties of liquid Xenon: diffusion (also referred to as Rayleigh scattering) and absorption; the latter heavily affects the photo-statistics while the former does not.

Density	2.95 g/cm^3
Boiling and melting points	165 K, 161 K
Energy deposition per scintillation photon	24 eV [44]
Radiation length	2.77 cm
Decay-time	4.2 ns, 22 ns
	45 ns [45]
Peak emission wavelength	175 nm
Scintillation absorption length	> 100 cm
Attenuation length (Rayleigh scattering)	~ 40 cm
Refractive index	1.56 [46]

Table 4.1: Properties of liquid Xenon

A design of the liquid Xenon photon detector is shown in Fig. 4.1. We adopt here a simple "mini-Kamiokande" scheme [47], i.e.sides by about 800 photomultiplier tubes, with an effective photocathode coverage as high as $\approx 35\%$ on the front face. The outputs of these 800 PMTs provide a detailed image of the scintillation light needed to measure the position of the photon-conversion and to identify pile-up γ-rays. Every PMT will be read by a fast (2 GHz) waveform digitizer allowing us to achieve excellent timing and energy resolutions and giving the possibility to recognize the pile-up of accidental γ-rays.

The detector is located outside the magnet. The surface of the liquid Xenon is at 65 cm from the target center and its depth is 47 cm. The fiducial volume of the detector covers a solid angle of $\Delta\Omega/4\pi \simeq 12\%$ ($|\cos\theta| < 0.35$ and 120° in ϕ).

The temperature of liquid Xenon is -100°C, i.e. much higher than -200°C of liquid N_2. The thermal insulation and the cooling is thus simpler and easier to achieve.

The cryostat for the liquid Xenon detector consists of the Xenon vessel and a vacuum vessel for

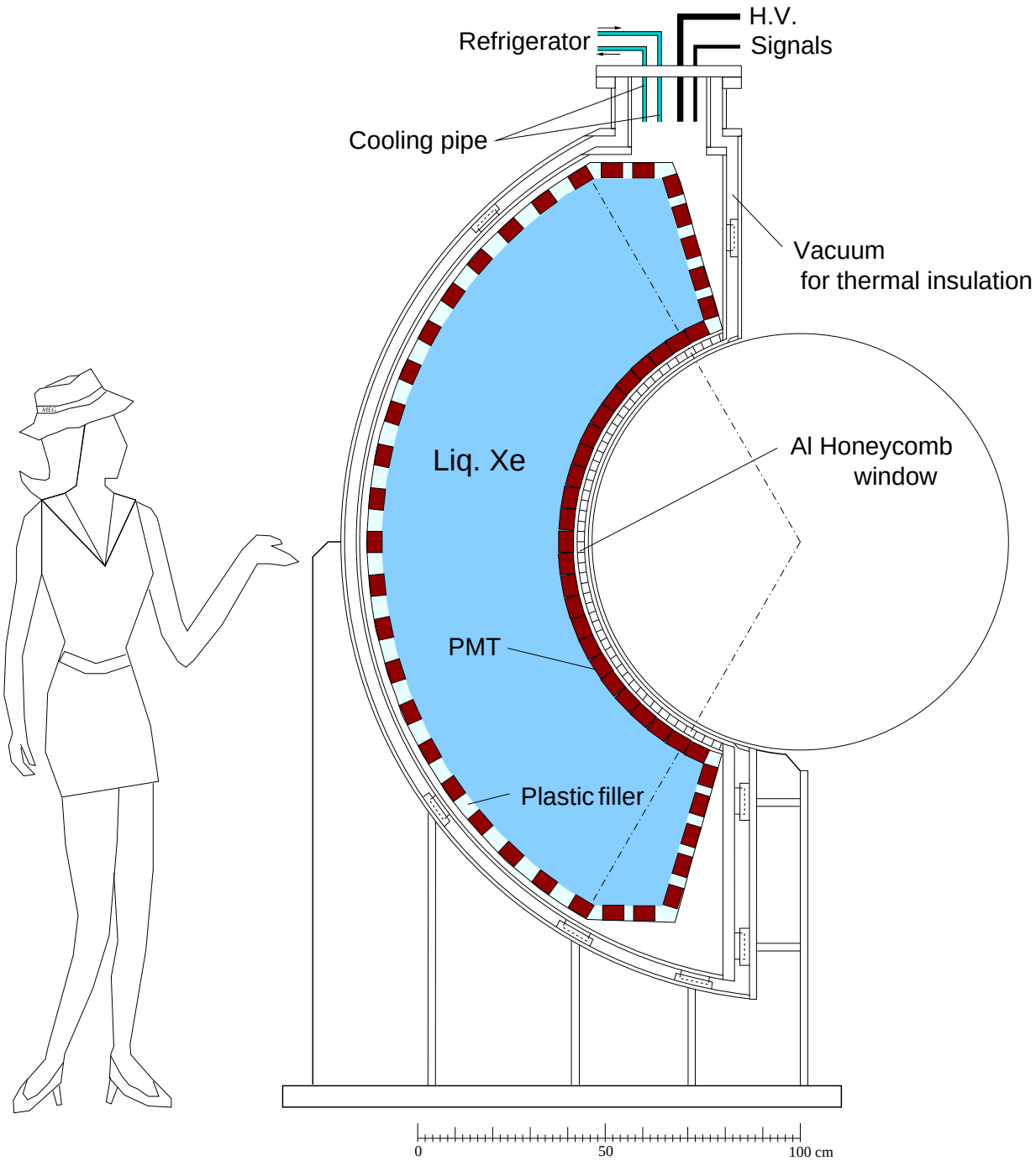

Figure 4.1: A cut view of the liquid Xenon detector.

thermal insulation. Its front face is a honeycomb structure made of aluminum used to reduce materials for incident photons. A 20 mm thick honeycomb core is sandwiched between two 1 mm plates, while the vacuum (outer) vessel is made of 0.5 mm stainless steel. The whole cryostat is made of stainless steel. As a cooling system of liquid Xenon, a direct-cooling refrigerator without coolant will be used.

Bunches of thin cables for signal and HV are taken out through special feedthroughs developed for the ATLAS experiment [48]. The structure to support the arrays of PMTs is installed through the side flange. The space between the PMTs is filled with a plastic filler attached at the support structure to prevent liquid Xenon from seeping in.

Xenon is purified before being liquefied by flushing it through Oxisorb cartridges [49], headed gas getter purifiers and molecular sieves. During operation Xenon gas, evaporated from liquid Xenon, will be recirculated through the purification system. The purity of the liquid will be monitored by looking at the light from alpha calibration sources inside the detector and by means of ionization chambers.

4.2 Photon detector R&D

The R&D work on the photon detector presented here has been performed using what we call the "large prototype". First R&D work was performed [10, 50] using a smaller (~ 2 liters active volume) apparatus seen by 32 PMTs. The Large Prototype has been investigated using a 40 MeV gamma beam, cosmic rays, and alpha sources. While performing these tests, it was found that the absorption length ($\lambda_{\rm Abs}$) of scintillation light in liquid Xenon in our detector was shorter than 10 cm due to remnants of water of the order of ppm. Because of this contamination an insufficient amount of scintillation light was detected. In order to remove the contaminant we introduced a purification scheme into the gas system and succeeded in achieving a $\lambda_{\rm Abs}$ of ~ 100 cm by circulating Xenon through a purifier.

4.2.1 The large prototype

A schematic view of the large prototype is shown in Figure 4.2: a rectangular box onto which 228 PMTs are assembled is installed into a chamber with a thermal insulation vacuum layer. The active volume of the detector is 67 liters. We use 2" UV-sensitive PMTs (R6041Q) whose main characteristics are summarized in Table 4.2.1.

PMT size	57 mm ϕ
Photo-Cathode material	Rb-Cs-Sb
Effective area	46 mm ϕ
Q.E. at 165 K	$\sim$5% (@ 175 nm)
Dynode type	Metal channel
Number of stages	12
Typical H.V.	1000 V
Current amplification	$\sim 10^7$

Table 4.2: Properties of R6041Q.

PMT developement is currently going on in collaboration with Hamamatsu Photonics with the aim of improving their performance [51].

A pulse-tube refrigerator is installed on the top of the chamber to condense Xenon. A liquid nitrogen cooling pipe is also incorporated to aid the refrigerator when more cooling power is required such as in the case of liquefaction. Usually we use 120 liters of liquid Xenon for detector operation. There are four ^{241}Am alpha sources and eight blue LEDs placed on the wall of the holder for PMT calibration. Detector operation has been tested for more than 100 days in total.

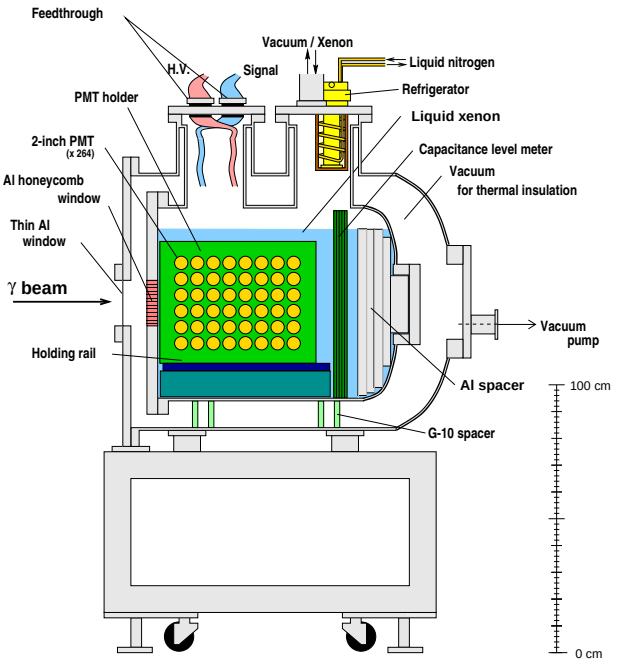

Figure 4.2: Schematic view of the large prototype.

4.2.2 Gamma beam test at TERAS

A γ beam test was carried out in February 2002 in AIST, Tsukuba in Japan. The electron storage ring (TERAS) was operated at the maximum electron current of 200 mA around the nominal beam energy of 762 MeV. Laser light of 266 nm was fed to the head-on collision point to induce inverse-Compton scattering for providing photons of energy up to 40 MeV. There were two collimators between the collision point and Xenon detector for defining the spot size on the detector face and removing low energy background. The schematic view of the γ beam line is shown in Figure 4.3. The detector was moved with respect to the beam incident position for studying the position dependence of the detector performance. For triggering cosmic ray events, 3 pairs of scintillation counters (TC1, TC2, and TC3) were placed as shown in Figure 4.4.

Figure 4.5 shows a calculated γ beam energy spectrum which includes all parameters of the laser system, electron storage ring, and geometry of collimators. The Compton edge at 40 MeV can be used

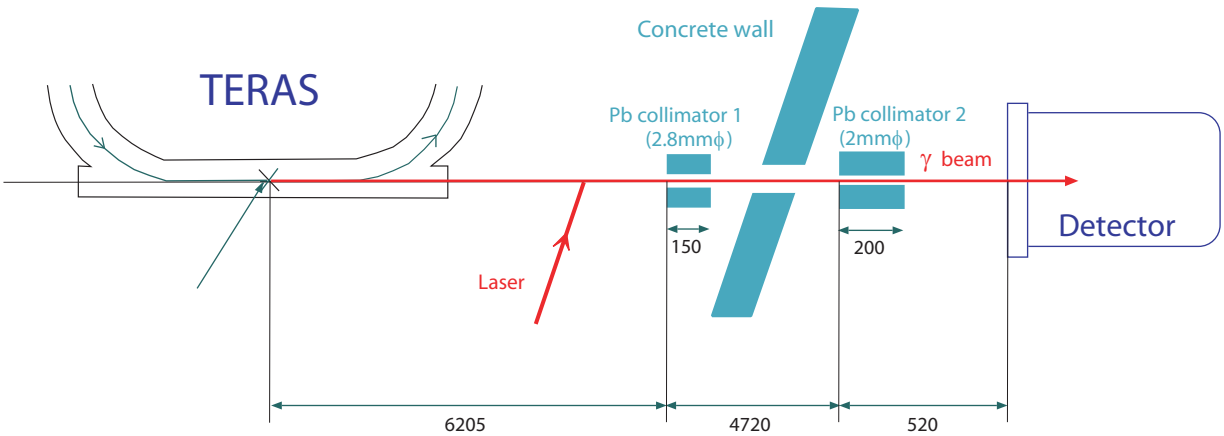

Figure 4.3: Layout of TERAS

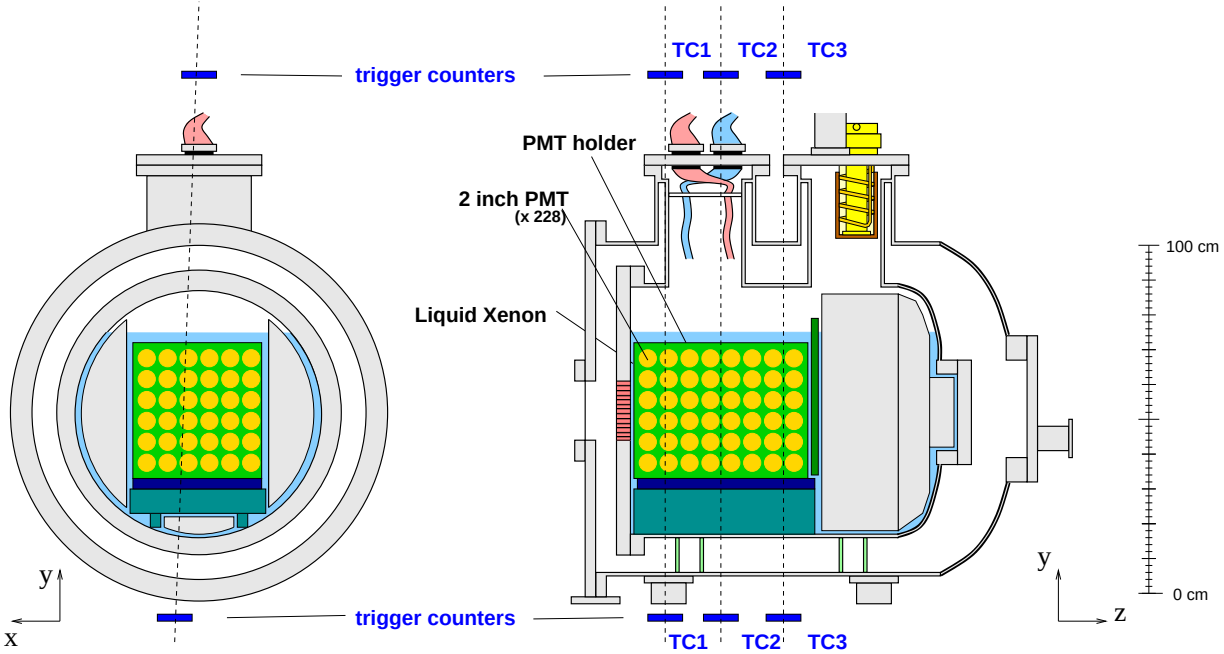

Figure 4.4: Experimental set-up for cosmic ray measurements with the Large Prototype. The trigger counters for cosmic ray trigger are also shown.

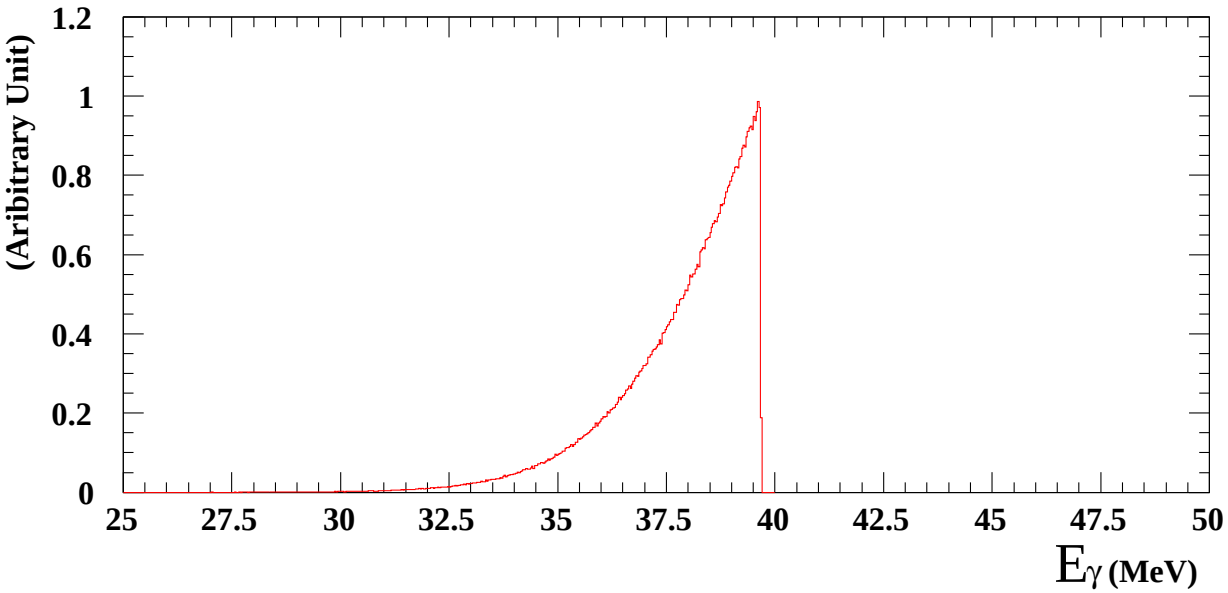

Figure 4.5: Calculated γ beam energy spectrum at TERAS.

for evaluating the energy resolution of the detector.

Xenon liquefaction was done prior to the beam time. The detector was evacuated to 2.0×10^{-2} Pa and then gas Xenon was filled in the chamber up to 0.2 MPa. The chamber and the detector were pre-cooled by means of the refrigerator and the liquid nitrogen cooling pipe down to around 165 K. Gas Xenon was accumulated in the chamber and liquefied via the cooling system. After liquefaction the liquid Xenon was kept at a stable temperature (163 K) and pressure (120 kPa) with the refrigerator. During the detector operation of 14 days, the temperature was stabilized to within ± 0.1 K and the pressure drift was kept to less than 1%.

PMTs Calibration

There are eight blue LEDs mounted on the holder for PMT gain calibrations. The LEDs were pulsed at 100 Hz frequency by an LED driver with continuously adjustable driving voltage. The trigger signal was supplied by the same clock generator used for the LED driver. Two out of eight LEDs were pulsed simultaneously for standard gain calibration and the other combinations were used for the estimation of the calibration systematic error. 50000 events with five different LED amplitudes were recorded in one calibration process. The standard deviation of the ADC spectrum (σ_{ADC}) depends on the number of photoelectrons (N_{pe}) observed by the PMT:

$$\sigma_{ADC}^2 = \sigma_0^2 + \frac{\overline{ADC}^2}{N_{pe}} \tag{4.1}$$

where $\overline{ADC}$ is the mean value of the ADC spectrum and σ_0 is a combined standard deviation, including the instability of LED voltage, time variation of the pedestal, etc. The variable N_{pe} is expressed in terms

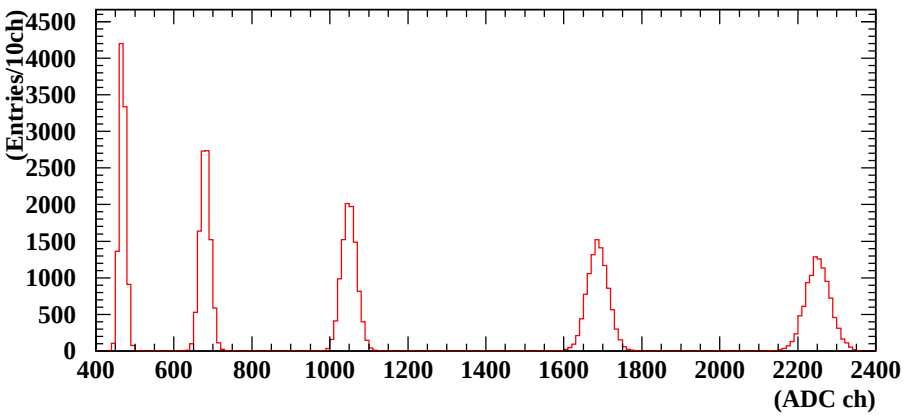

Figure 4.6: ADC spectrum of a typical PMT during the LED calibration.

of the PMT gain G as:

$$N_{pe} = \frac{\overline{ADC} \times C}{e \times G} \tag{4.2}$$

where C is the least count of the ADC, 200 fC, and e is the electric charge of an electron. From these two equations σ^2_{ADC} can be written as:

$$\sigma^2_{ADC} = \sigma^2_0 + \frac{e \times G}{C} \times \overline{ADC} \tag{4.3}$$

The variance σ^2_{ADC} is proportional to $\overline{ADC}$ and the gain of the PMT can be evaluated from the slope parameter. Figure 4.6 shows an ADC spectrum for a typical PMT and in Figure 4.7 an example of the relation between σ^2_{ADC} and $\overline{ADC}$ is shown. By fitting this relation with a linear function the PMT gain was evaluated and adjusted to 10^6 at the start of detector operation[1]. Calibration data were taken three times a day during operation.

The reproducibility of the calibration was estimated to be $\sim 1\%$. As systematic study using different combinations of LEDs showed, the gain adjustment accuracy ranges from 1% to 4%, with 2% on average. Details of the gain calibration are described in [52].

In order to take into account the different quantum efficiencies of the PMTs, calibration data were taken for alpha events in low temperature gas Xenon. Since the effects of absorption and scattering are expected to be negligibly small in gas, light transmission can be easily simulated considering the geometrical configuration. The PMT output spectra were fitted with a convolution of the Poisson function and a Gaussian and then compared with the Monte Carlo predictions in order to evaluate the quantum

[1] Formulæ(4.1) to (4.3) are obtained by neglecting effects associated with the first dynode amplification and the single photoelectron resolution. The inclusion of these effects implies slight modifications of the above expression which, however, are the same for all the PMTs within the errors and do not affect the linearity of the variance. The effective absolute gain so obtained might overestimate the true value by 50%, but should not introduce any further uncertainty in the relative gain.

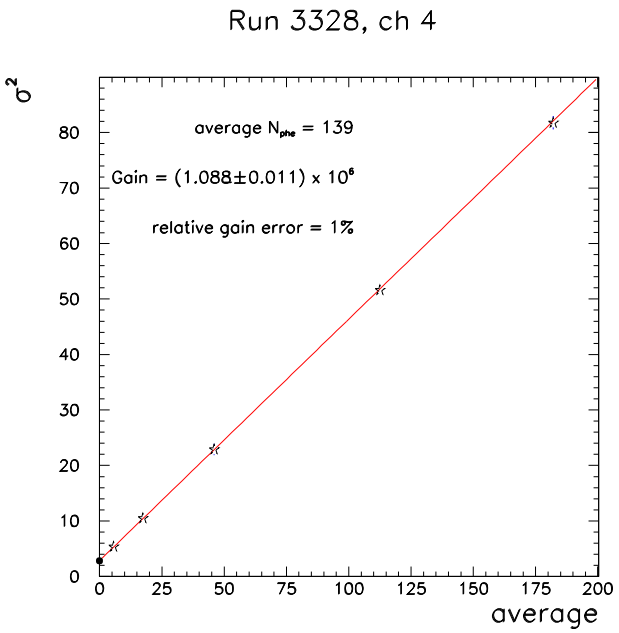

Figure 4.7: Example of the relationship between σ^2_{ADC} and $\overline{ADC}$ in LED calibration.

efficiency of each PMT. The distribution of the obtained quantum efficiencies is shown in Figure 4.8. Details of the analysis are described in [53].

Energy resolution for 40 MeV gamma

For simply getting information on the event depth (the z-coordinate of the first conversion point) a variable is introduced into the analysis which is called here σ^2. The definition of this variable is

$$\sigma^2 = \frac{\sum n_{pe}(i)x(i)^2 + n_{pe}(i)y(i)^2}{\sum n_{pe}(i)} - \left(\frac{\sum n_{pe}(i)x(i) + n_{pe}(i)y(i)}{\sum n_{pe}(i)}\right)^2 \tag{4.4}$$

where $n_{pe}(i)$ is the observed number of photoelectrons in each PMT on the front wall, $x(i)$ and $y(i)$ are the front face PMT positions. This variable expresses the width of the event shape observed by the front face PMTs, which is related to the depth of the photon conversion as predicted by the Monte Carlo simulation, as shown in Figure 4.9.

Figure 4.10 shows the correlation between N_{pe} and σ^2 (left) and a spectrum (right) of the total number of photoelectrons in the region of $50 \leq \sigma^2 \leq 55$, for events corresponding to photons incident at the centre of the detector. It can be clearly seen that there is a strong correlation between these two variables. This suggests that the absorption of the scintillation light in liquid Xenon is larger than expected. The FWHM of the N_{pe} spectrum, evaluated to be 35%, deteriorates under this condition due to small photoelectron statistics and the strong correlation.

For understanding what deteriorates the resolution, a Monte Carlo simulation was done with various input parameters. Results with several $\lambda_{\rm Abs}$ values are summarized in Table 4.3. The contribution

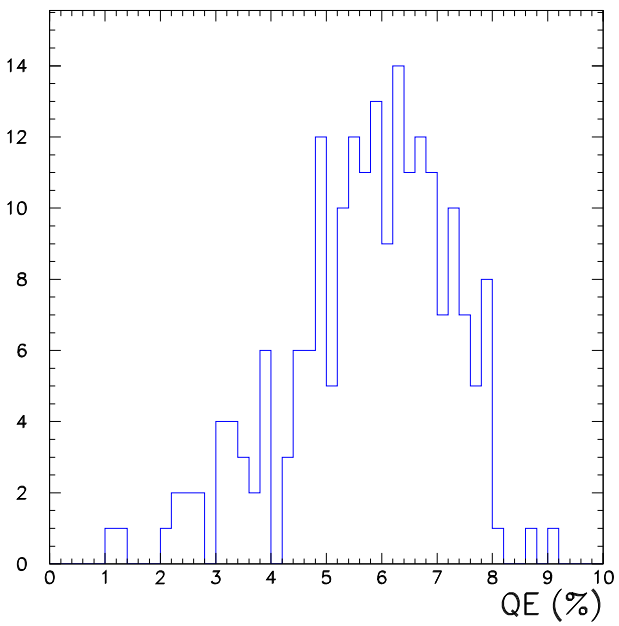

Figure 4.8: Distribution of quantum efficiencies evaluated using gas Xenon data.

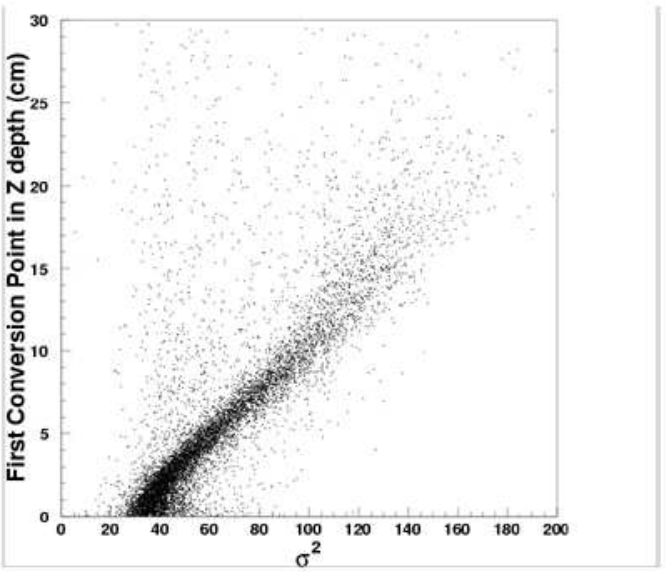

Figure 4.9: Correlation between the depth of the first conversion point and σ^2 predicted by the Monte Carlo simulation.

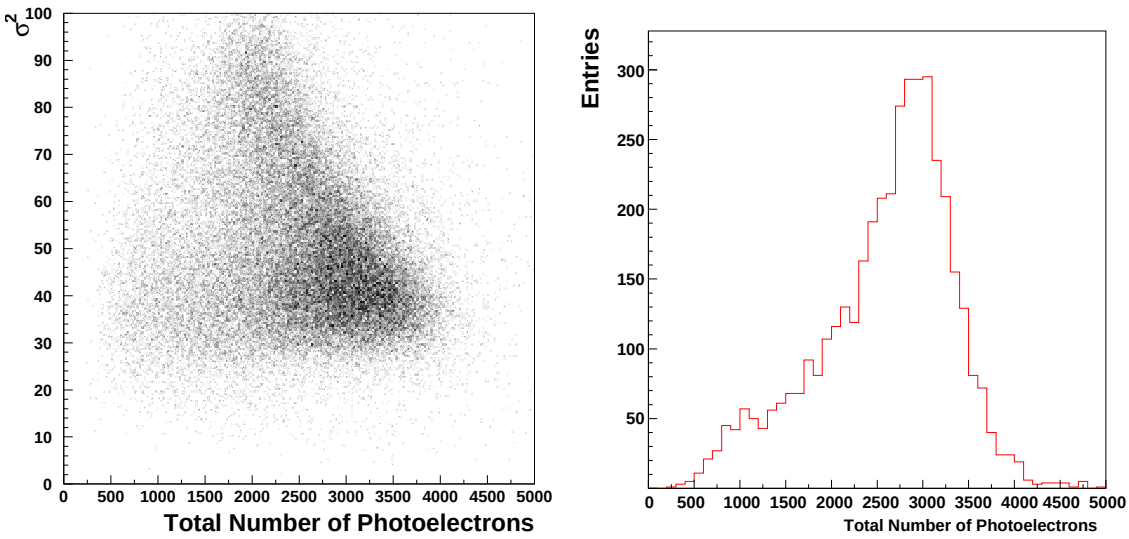

Figure 4.10: Correlation between N_{pe} and σ^2 (left) and N_{pe} spectrum in the region of $50 \leq \sigma^2 \leq 55$ for 40 MeV back-scattered γs (right).

Absorption length ($\lambda_{\rm Abs}$)	FWHM
7 cm	36%
10 cm	22%
50 cm	4 %
100 cm	2 %

Table 4.3: Input parameters of $\lambda_{\rm Abs}$ and the expected FWHMs for each value. The FWHMs were estimated using 40 MeV monochromatic γs.

of the intrinsic back-scattered photon energy spread is estimated to be 6.1% (FWHM) in case of no scintillation light absorption (see Figure 4.5). The effect of the PMT calibration accuracy is estimated, most conservatively, to be less than 3% (FWHM). The obtained FWHM can be explained with a short $\lambda_{\rm Abs}$ around 7 cm and the other effects are negligibly small under these conditions. Figure 4.11 shows the Monte Carlo prediction for the correlation between N_{pe} and σ^2. It assumes a Rayleigh scattering length ($\lambda_{\rm Ray}$) of 30 cm and a $\lambda_{\rm Abs}$ of 7 cm (top left), 100 cm (top right) and 500 cm (bottom). The dependence shown in Figure 4.10 is reproduced fairly well.

Absorption length during the γ beam test

We estimated $\lambda_{\rm Abs}$ by using cosmic ray and alpha events collected during the γ beam test. Details of the analysis are summarized in [53]. Figure 4.12 shows the number of photoelectrons observed in the front (or back) face PMTs as a function of reconstructed z-coordinate of cosmic rays (black dots). The reconstruction was done by using the N_{pe} information from PMTs belonging to the different detector faces.

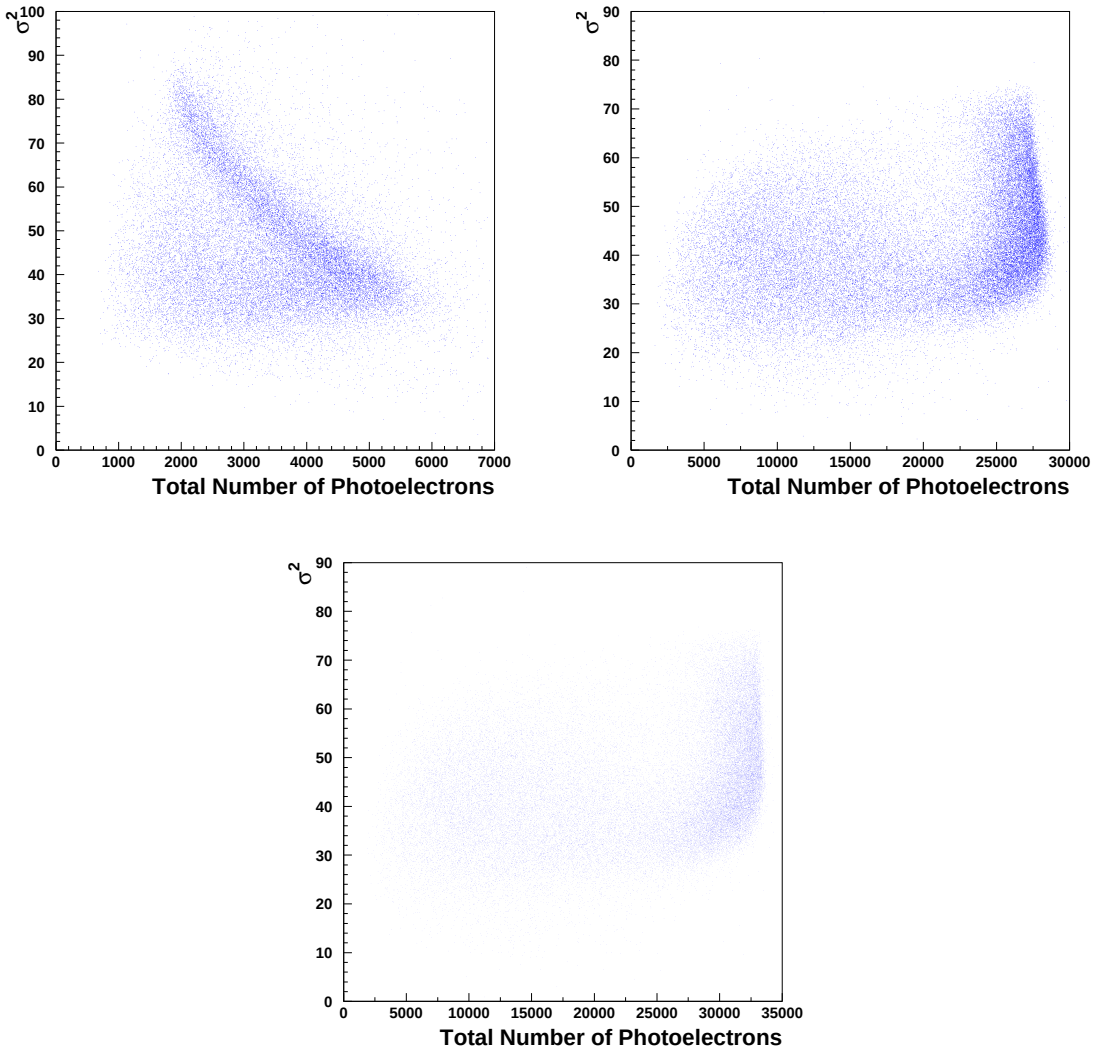

Figure 4.11: Monte Carlo predictions for the correlation between N_{pe} and σ^2. $\lambda_{\mathrm{Ray}} = 30$ cm and $\lambda_{\mathrm{Abs}} = 7$ cm (top left), 100 cm (top right), and 500 cm (bottom) are assumed in the simulation.

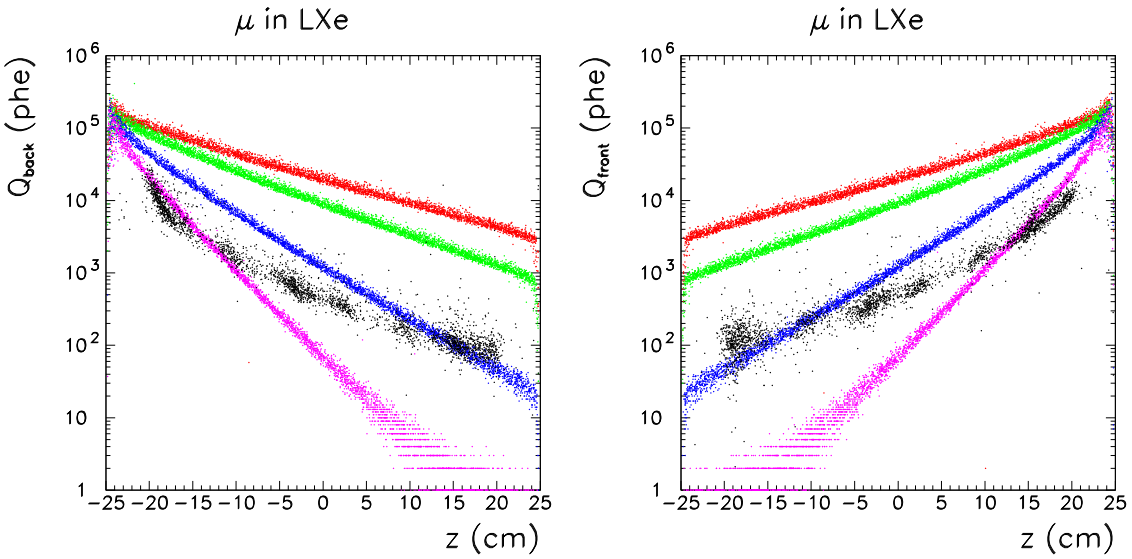

Figure 4.12: Number of photoelectrons observed by the PMTs on the back and front faces for cosmic events (Black dots=data, red=100 cm, green=50 cm, blue=10 cm, magenta=5 cm absorption length).

Monte Carlo simulation predictions with different absorption lengths (5 cm, 10 cm, 50 cm, and 100 cm) are superimposed. In the Monte Carlo simulations $\lambda_{\rm Ray}$ was taken as 30 cm [54]. There is a discrepancy in shape between the data and the Monte Carlo simulation: the data distribution is steeper near the face and falls more gradually for large z. This discrepancy can be explained by introducing a wavelength-dependent absorption effect due to some impurities such as water, which exhibit a high absorption at the scintillation wavelength (Figure 4.13): some light is readily extinguished after a few cm, while a surviving component (a few percent) exhibits a longer (of the order of one meter) $\lambda_{\rm Abs}$. A confirmation of this hypothesis came from a mass spectrometer analysis subsequently described in Section 4.2.3. Alpha events were also analyzed to estimate $\lambda_{\rm Abs}$. Figure 4.14 (left) shows the ratio of observed number of photoelectron to the Monte Carlo prediction with input parameters of $\lambda_{\rm Abs} = \infty$ and $\lambda_{\rm Ray} = 30$ cm as a function of the distance from the alpha sources to the PMTs. In Figure 4.14 (right) the same distribution is shown but with different input parameters of $\lambda_{\rm Abs} = 7$ cm and $\lambda_{\rm Ray} = 30$ cm. It can be seen that the ratio is consistent with 1 in the short distance region, while PMTs located at more than 30 cm away from the source seem to receive more light than predicted. This is the same feature seen in the cosmic ray events analysis, which can be reasonably explained by a wavelength-dependent absorption due to impurities.

In conclusion it is certain that there were impurities present during the γ beam test which affected the detector operation. Cosmic ray, alpha and photon data indicate a short $\lambda_{\rm Abs}$, less than 10 cm, in the liquid Xenon of this test.

Position resolution studies

For determining the γ incident position it is important to define the size of an event so that the reconstruction should be affected as little as possible by shower fluctuations. For this reason the γ incident

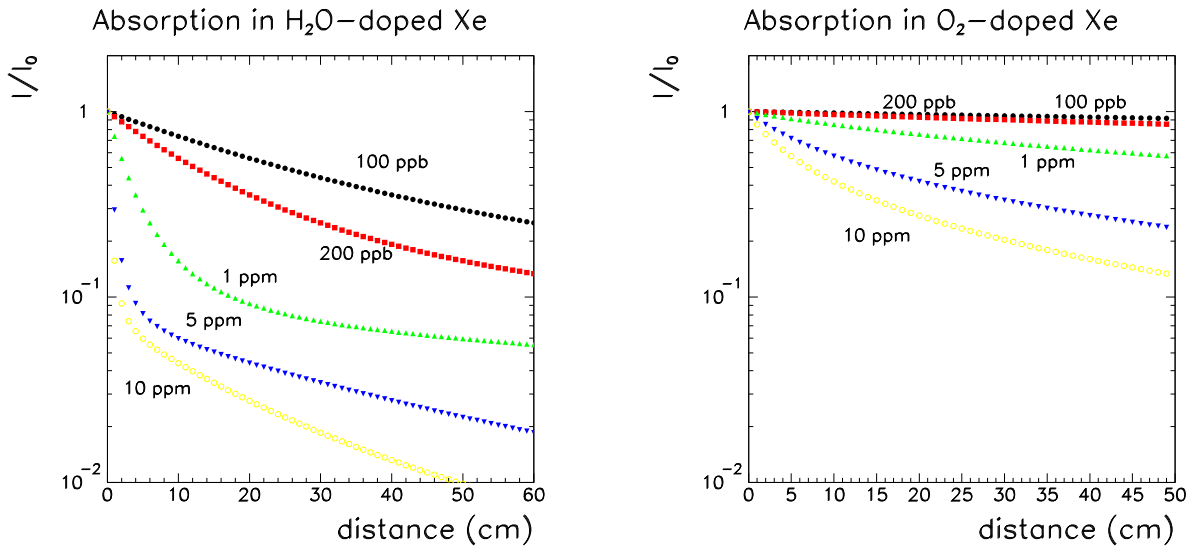

Figure 4.13: Simulation of the light absorption by water and O_2 for different levels of contamination.

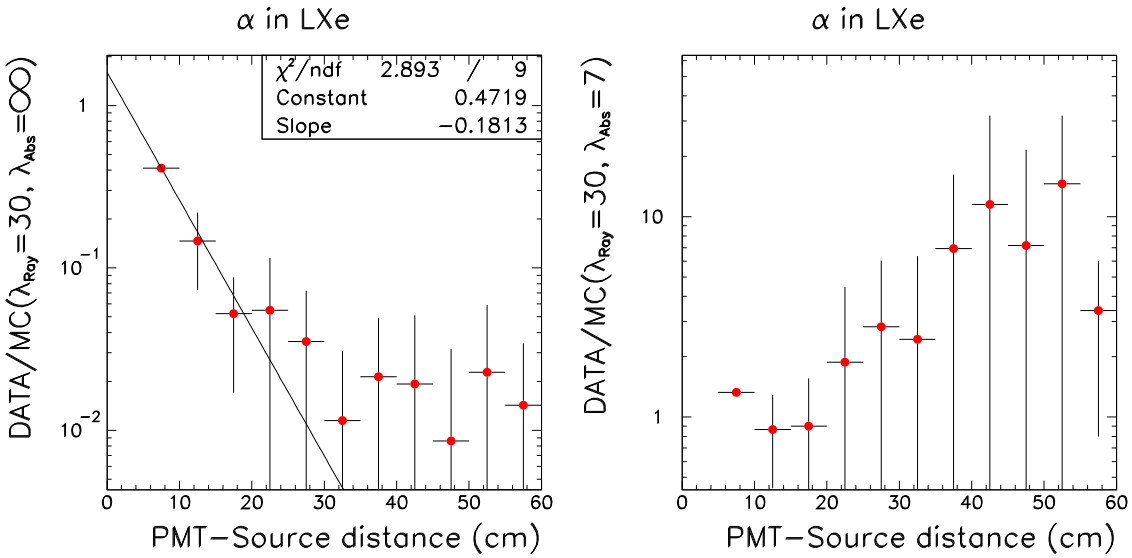

Figure 4.14: Ratio of N_{pe} for alpha events to Monte Carlo prediction as a function of the distance between the alpha sources and the PMTs.

position is reconstructed in two steps as described below. The first step is to find a peak position of the light distribution; the second one is to determine more precisely the incident position by an iterative process. A region is selected around the pre-determined peak and the weighted mean of the distribution is calculated, where the region size is optimized by means of the Monte Carlo simulation so that we can get the best position resolution. The mean value is set as the new peak position value and the procedure is repeated until the peak position converges. Position reconstruction for $x-$ and $y-$coordinates were done independently using the same algorithm. The algorithm uses information only from the front face PMTs arranged in a 6×6 matrix.

Figure 4.15 shows the distributions of reconstructed $x-$positions for 40 MeV photons incident on four different positions[2]. Monte Carlo simulation predictions are shown in Figure 4.16. It can be seen that the data are slightly worse than the Monte Carlo predictions in which a $\lambda_{\rm Abs}$ of 10 cm was used. The reconstructed $y-$coordinate has a similar distribution. Note that in this analysis the effect of the beam spread is not subtracted since it is expected to be small.

Figure 4.18 shows a comparison between data and Monte Carlo simulations with different $\lambda_{\rm Abs}$'s. The horizontal axis shows the distance between the γ incident position and the nearest PMT centre. It can be seen that the obtained resolution can be explained by introducing a $\lambda_{\rm Abs}$ around 7 cm in the simulation and that we can improve the position resolution if we achieve a sufficiently long $\lambda_{\rm Abs}$ of the order of 100 cm.

4.2.3 Purification system

Mass spectrometer analysis

After the beam test, the detector was moved from AIST to KEK for studying more carefully the impurity problem. A quadrupole mass spectrometer was introduced as a residual gas analysis (RGA) device to investigate what kind of materials exist in the chamber prior to filling Xenon. The chamber was again evacuated at KEK, a part of the residual gas in the chamber was sampled to the analyzing section. Figure 4.19 shows the mass spectrum of the remaining gas. Several peaks corresponding to He ($A = 4$), H_2O ($A = 18$), N_2 and CO ($A = 28$), O_2 ($A = 32$) and CO_2 ($A = 44$) can be seen. The peak existing around the mass number of $A \simeq 65$ corresponds to doubly ionized Xenon[3]. From these peaks it is clearly seen that water contamination is the largest contribution and dominates the ultimate vacuum level.

Purification system description

For removing water contamination an additional gas system was used for circulating and purifying Xenon during detector operation, with a heated gas getter purifier. This purifier employs metal getter technology based on zirconium metals that form irreversible chemical bonds to remove all oxide, carbide and nitride impurities down to a ppb level. The purifier can handle gas flow rates up to 30 liters/minute. A metal filter is also employed in this purifier to remove dust particles that could absorb UV light. Figure 4.20 shows the circulation system schematically. Xenon evaporates from the liquid surface and is transferred to the purifier through a diaphragm circulation pump. Then almost all kinds of impurities in Xenon are removed by the purifier. The purified gas is subsequently returned and liquefied in the chamber.

[2]The γ incident positions are explained in Figure 4.17

[3]Consequently Xenon was observed as an atom with half of Xenon mass number ($A = 131$).

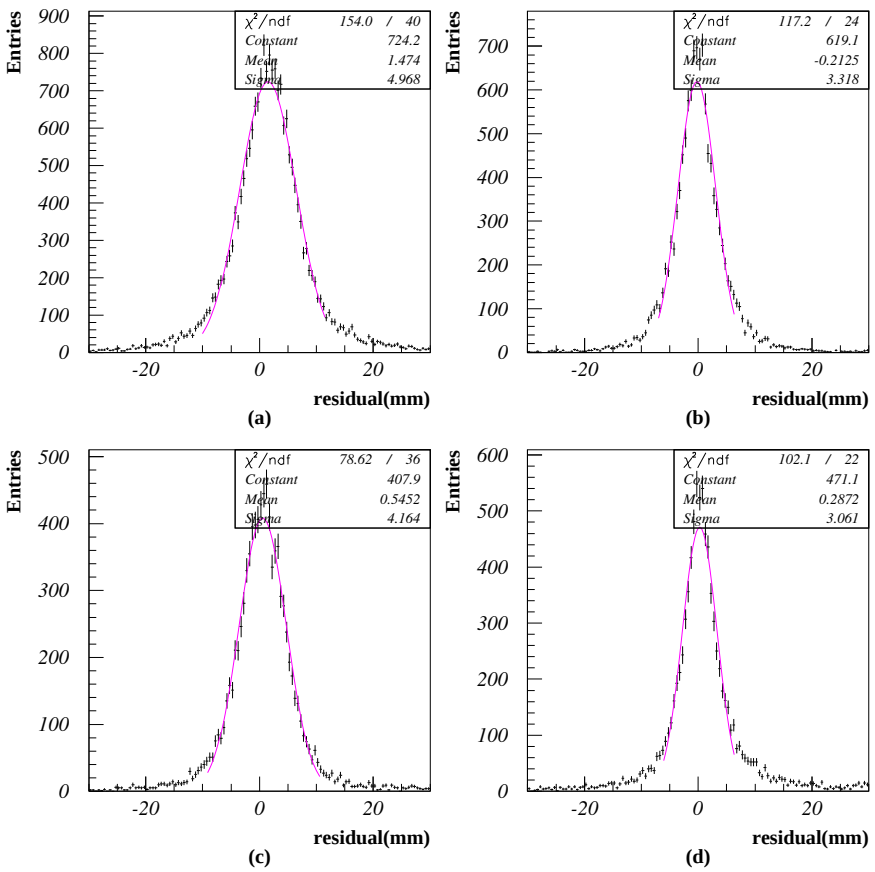

Figure 4.15: Reconstructed position distributions for 40 MeV back-scattered γs for four incident positions. The γ's incident positions (from (a) to (d)) are explained in Figure 4.17.

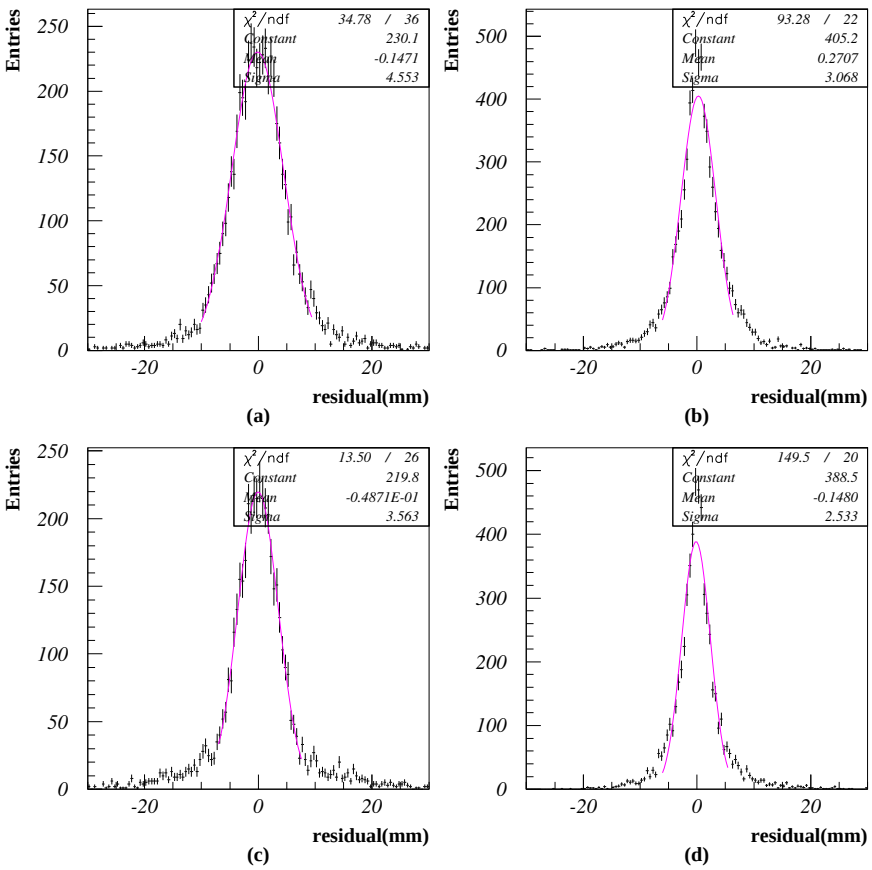

Figure 4.16: Monte Carlo predictions of reconstructed position distribution for four different, incident γ positions. The γ incident positions (from (a) to (d)) are explained in Figure 4.17.

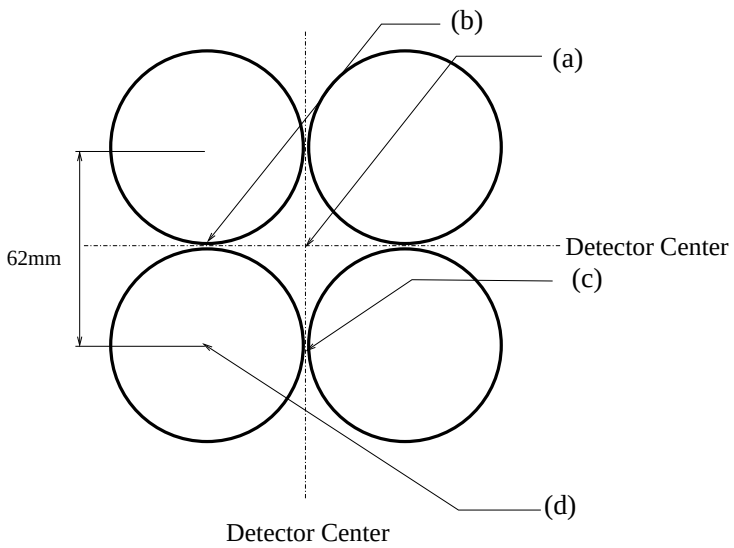

Figure 4.17: Gamma incident positions on the front face PMTs for position resolution study.

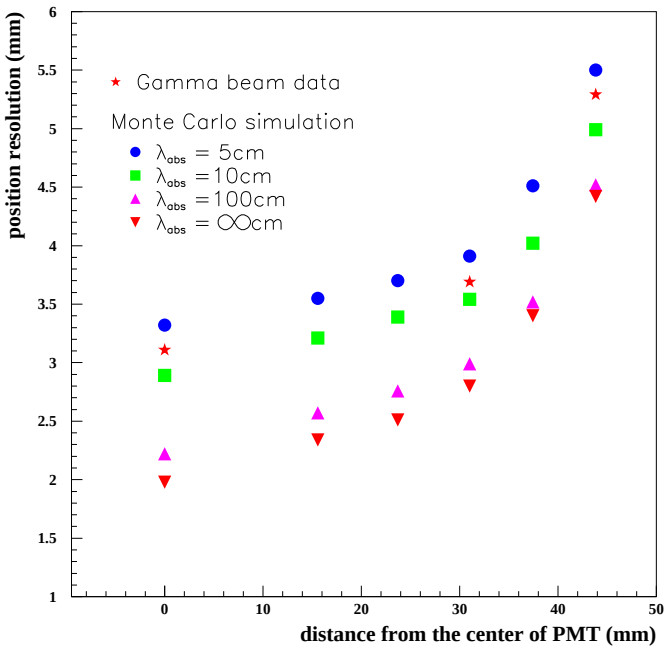

Figure 4.18: Comparison of position reconstruction resolution (in σ) between data and Monte Carlo simulation using several values of λ_{Abs} as input parameters.

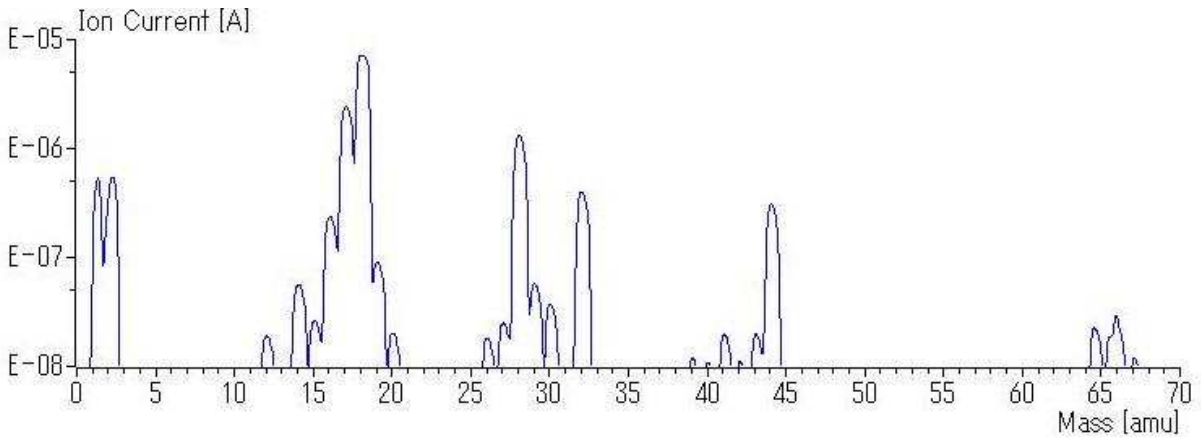

Figure 4.19: Mass spectrum of the remaining gas.

The circulation rate is $\sim$ 6 cm^3/minute in liquid, limited by the power of the circulation pump. More cooling power is required during circulation for liquefying returned Xenon gas in addition to the power for recondensation of evaporating Xenon in the chamber. The required additional cooling power is calculated to be 55 W for this flow rate, which is an overload for the refrigerator currently used. For this reason the detector operating condition during circulation is different from that of the simple refrigerator operation. The pressure in the chamber changes from 0.13 MPa to 0.135 MPa depending on the liquid nitrogen flow, though this does not cause any problem for the scintillation light measurement.

Performance of the purification

Some 120 liters of Xenon were liquefied and a stable detector operating condition was established. The purification cycle was then started and the light yield immediately started to increase both for cosmic ray and alpha events. In Figure 4.21 (left) is shown the light yield for alpha events of PMTs located at 7.6 cm and 11.6 cm away from alpha sources. It is also shown in Figure 4.21 (right) how N_{pe} increases for cosmic ray events as a function of time.

The purification cycle can be modeled as follows: the variation of the contamination level should be proportional to the impurity density at that time if there is no further outgassing at low temperature. Therefore the impurity density in the chamber can be expressed as a function of time:

$$C(t) = C_0 \exp\left(-\frac{t}{\tau}\right) \tag{4.5}$$

where C_0 is the initial value of the impurity density in the chamber and τ is the time constant of the purification cycle, which is determined by the purification speed and efficiency. Consequently, the absorption length caused by this impurity is written with the same time constant as:

$$\lambda(t) = \lambda_0 \exp\left(\frac{t}{\tau}\right) \tag{4.6}$$

where λ_0 means the initial value of the absorption length. Therefore the number of photoelectrons observed

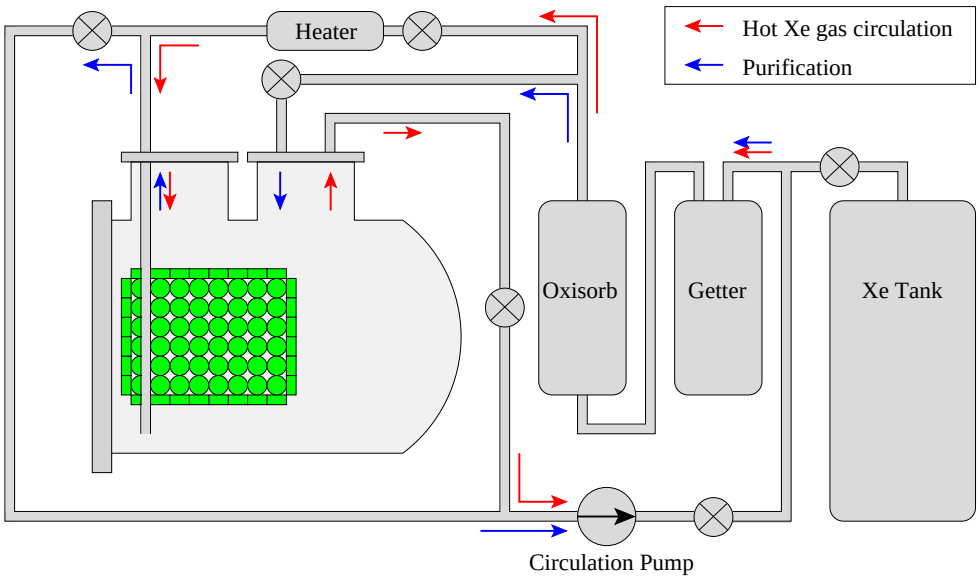

Figure 4.20: Diagram of the circulation system. The gas flow is indicated with arrows. Two kinds of gas circulation mode were prepared, one for purification and the other for hot gas circulation to warm up the detector. Hot gas circulation is under investigation to remove impurity contamination effectively before starting liquefaction.

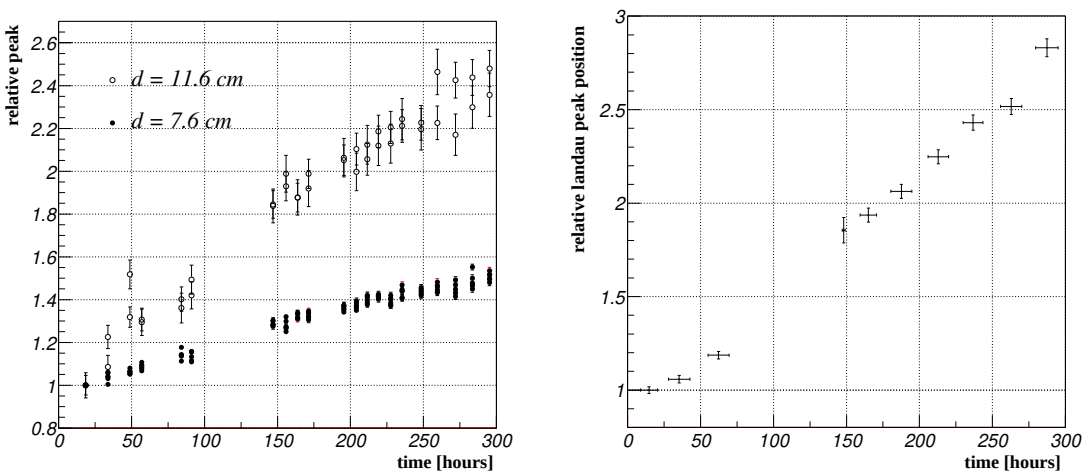

Figure 4.21: Light yield improvement for alpha events observed by PMTs located at 7.6 cm and 11.6 cm away from alpha sources (left). The light yield for cosmic ray events is also shown (right).

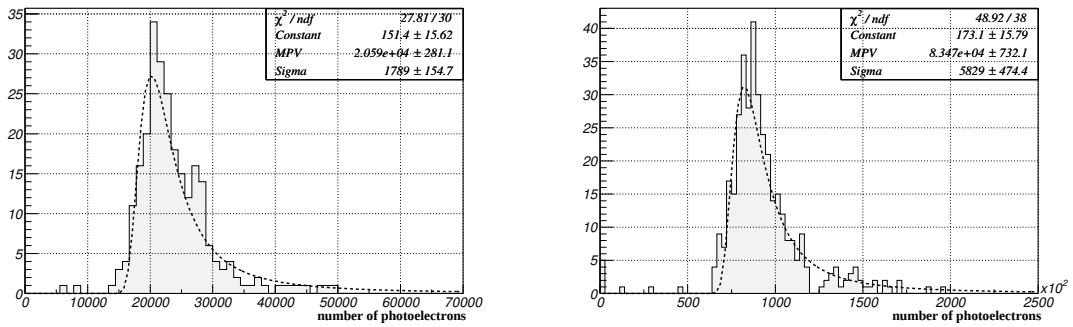

Figure 4.22: Distribution of N_{pe} for cosmic ray events triggered by the middle set of trigger counters. Before purification (left) and after 600 hours purification (right). Note that the abscissa on the right-hand side plot is multiplied by a factor 10^2.

by PMTs at an effective distance r from the light emission point can be written as:

$$N(r,t) = N_\infty \exp\left(-\frac{r}{\lambda_0}\exp\left(-\frac{t}{\tau}\right)\right), \tag{4.7}$$

where N_∞ is the light observed for perfectly transparent liquid Xenon. The light yield for cosmic ray events shown in Figure 4.21 is fitted with this function. The obtained time constant (τ) is 360±12 hours. A similar analysis was made for alpha events and we obtained a consistent time constant, namely ~ 350 hours.

We circulated and purified Xenon continuously for more than 50 days. We made various tests during this time to understand the purification process, by stopping purification, stopping circulation, increasing the flow rate and so on. Figure 4.22 shows the distribution of N_{pe} after 600 hours of purification. The light yield for cosmic ray events increased by more than a factor of 4 compared to the yield at the beginning of purification.

Absorption length after purification

The absorption length was estimated after starting the purification by using the methods described above. Figure 4.23 shows the ratio of alpha data in liquid Xenon to the Monte Carlo simulation (left) and to alpha data in cold gas (right)[4]. Three different data sets are shown: before purification (circles), after two weeks of purification (squares), and after one month of purification (stars).

In the Monte Carlo simulation employed here we used $\lambda_{\rm Ray} = 45$ cm, which is evaluated by using our recent data after purification, instead of 30 cm. The evaluation was made by comparing the number of photoelectrons observed by PMTs on the same surface as the alpha source to the Monte Carlo predictions. The value of $\lambda_{\rm Ray} = 45$ cm is in agreement with recent calculations [55]. The figure shows an increase of the absorption length due to the purification. However, it is apparent that the $2^{\rm nd}$ and $3^{\rm rd}$ data points are systematically lower than the other points. The PMTs corresponding to these points are located on the

[4]Since absorption and diffusion in gaseous Xenon influence light transport less than in liquid Xenon, the gas data can be taken as a reference.

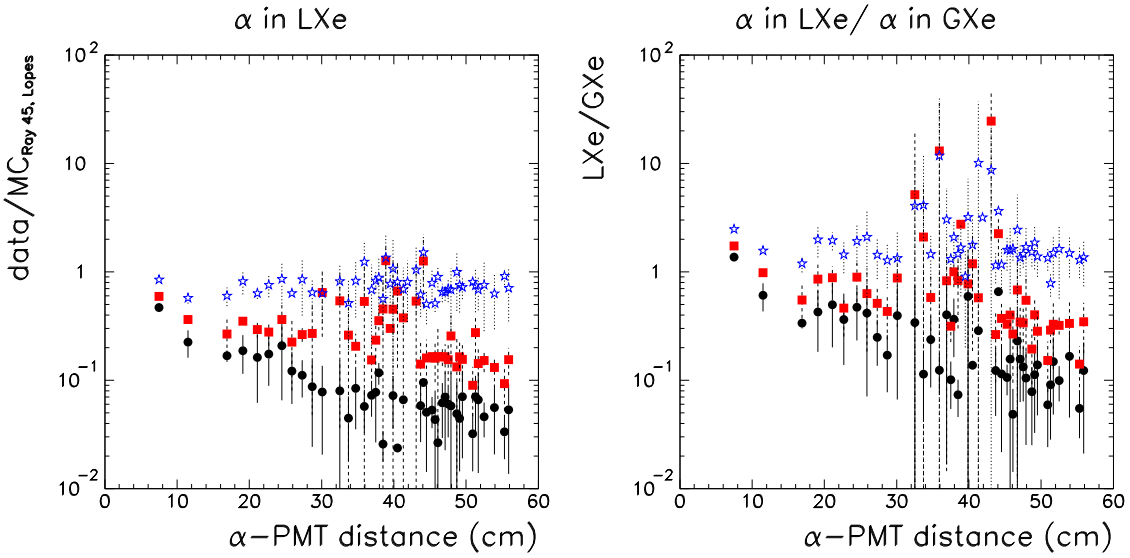

Figure 4.23: Comparison of alpha data in liquid Xenon to Monte Carlo simulation (left) and to alpha data in cold gaseous Xenon (right) for three different runs: before the purification (circles), after two weeks of purification (squares), and after one month of purification (stars).

front face and see the alpha sources under large angles. In addition their signals are read by consecutive electronics channels; further investigation is required for a complete understanding of the data.

In order to estimate the ultimate $\lambda_{\rm Abs}$, the most recent data (stars in Figure 4.23) were re-histogramed and fitted with exponential functions. The $2^{\rm nd}$ and $3^{\rm rd}$ points in Figure 4.23 were excluded in fitting. The results are shown in Figure 4.24. From the comparison with the gas data, we can evaluate an effective $\lambda_{\rm Abs}$ of 80 cm, which however includes the effect of diffusion only in the liquid data and therefore represents a lower limit on the $\lambda_{\rm Abs}$. The exponential fit to the comparison with the Monte Carlo simulation, which includes the effect of Rayleigh scattering ($\lambda_{\rm Ray} = 45$ cm), does not show a significant slope. We can therefore use this result to establish a lower limit of 100 cm at 97.5% confidence level for $\lambda_{\rm Abs}$.

We also compared the cosmic ray data to the Monte Carlo predictions using the observed number of photoelectrons. In this case the comparison is more dependent on the Monte Carlo parameters (such as the required energy for emitting one scintillation photon) and on the modelling (for instance the light reflection on the PMT windows); however, we can conclude that the observed light yield agrees with our simulation with a $\lambda_{\rm Abs}$ of 100 cm, and we are confident that the performances predicted by our Monte Carlo simulation with $\lambda_{\rm Abs} = 100$ cm are achievable.

Future prospect

Further optimization studies of the purification process are currently under way. It is important to study how we can increase the purification speed. In this study the followings need to be investigated:

1. studies on the materials used in the prototype;

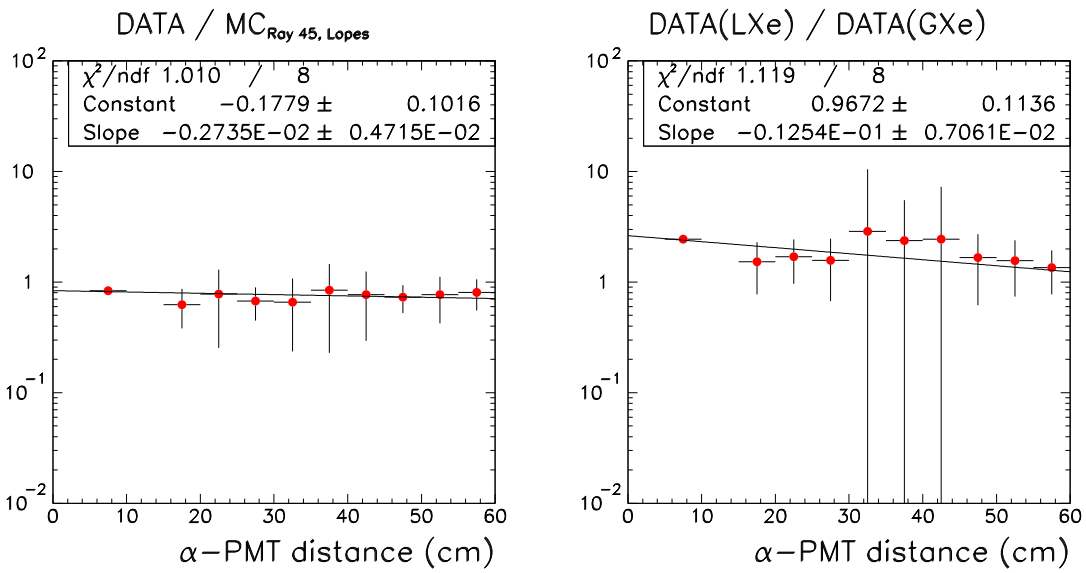

Figure 4.24: Absorption length determination from the comparison to the Monte Carlo simulation(left) and to the cold gas data(right).

2. possible method of baking the material during evacuation;

3. increasing the purification flow rate.

We are considering whether to replace any plastic material in the chamber with metal or Teflon in order to reduce the amount of remaining water as much as possible before starting liquefaction. We also plan to raise the temperature of the detector during evacuation so that residual water molecules can more easily escape from the material surface. However, since the PMTs should not be heated above 60°C, care must be taken, when warming the detector, not to create large temperature gradients in the chamber. For this purpose we plan to circulate hot N_2 gas after a first rough evacuation. The chamber will be evacuated again after nitrogen circulation until a sufficient vacuum level will be reached. Increasing the flow rate of the purification is also an important issue. If we can handle a higher flow rate, we can reduce the time to be invested for Xenon purification.

4.3 Final photon detector

4.3.1 Expected Performance

In this section the expected performance of the final photon detector is evaluated using our Monte Carlo simulations based on the present knowledge obtained from the studies with the large prototype detector. Details on the photon detector simulation can be found in [56].

As it is clear from the preceeding sections, the detector performance largely depends on the Xenon

purity, which affects the absorption length of the scintillation light. Here, we conservatively assume an absorption length of 100 cm that we have so far attained with the prototype, although we aim at realizing a longer absorption length in the final detector.

Due to the C-shape of the final detector, the PMT arrangement is another important factor which determines the performance. To obtain an efficient and uniform response to incident γ-rays, various arrangements are currently being studied.

We use here a simple, realistic, but still not optimized, arrangement of PMTs for an evaluation of the detector performance, which could be improved by other arrangements in the future. In the configuration studied here, the PMTs are placed as dense as possible on the front (entrance) wall, just like in the prototype, with 24 PMTs along ϕ and 13 PMTs along the muon beam direction (z), while the other walls have less dense PMT coverage (the rear wall: $27(\phi) \times 8(z)$, the up-/down-stream walls: $24(\phi) \times 5(r)$, and the top/bottom walls: $8(z) \times 5(r)$). The resulting total PMTs number in this configuration is 848.

Detector resolutions

A 52.8 MeV γ-ray entering the liquid Xenon loses most of its energy near the entry point, typically within $2 \div 10$ cm from the surface (Fig. 4.25).

The distribution of the PMT outputs on the detector entrance face becomes broader when the γ-ray conversion occurs deeper inside the Xenon volume. Using the width of the distribution, the depth of the γ-ray conversion point (z_γ) can be determined with a resolution of 14 mm (FWHM) (Fig. 4.26).

The accuracy of the conversion point determination is translated into a timing resolution of 85 ps. The fast rise time and the high scintillation light statistics provided by liquid Xenon are therefore sufficient in principle for the front PMTs to provide a timing determination with a resolution of 100 ps (FWHM). These performances will however have to be verified experimentally with new measurements using the large prototype.

As described in Section 4.2.1, the position of the incident γ-rays can be accurately determined by using the PMTs nearest to the incident position. Therefore, the position resolutions in the final detector are more or less the same as the prototype ones, as long as the PMT density on the front wall is similar. The resolutions obtained from the γ-ray beam test agree well with those of the Monte Carlo simulations assuming a $5 \div 10$ cm absorption length. With a 100 cm absorption length, the simulation study indicates that the same reconstruction algorithm used for the prototype yields an average 9 mm resolution (FWHM). Another algorithm, giving a more uniform response, achieves a resolution of 10.6 mm (FWHM). Our study also shows that the resolutions slightly improve with higher photo-electron statistics for a longer absorption length.

For what concerns energy measurements we investigated three different ways of reconstructing the energy of $\sim$ 50 MeV photons as a function of the light absorption length used in our Monte Carlo simulation:

1. A simple sum of the charges seen by all the PMTs (Q_{SUM}) taking into account the different PMT densities on the various surfaces;

2. a minimization procedure based on the assumption that the light be emitted at two different points along the photon direction (dipole fit);

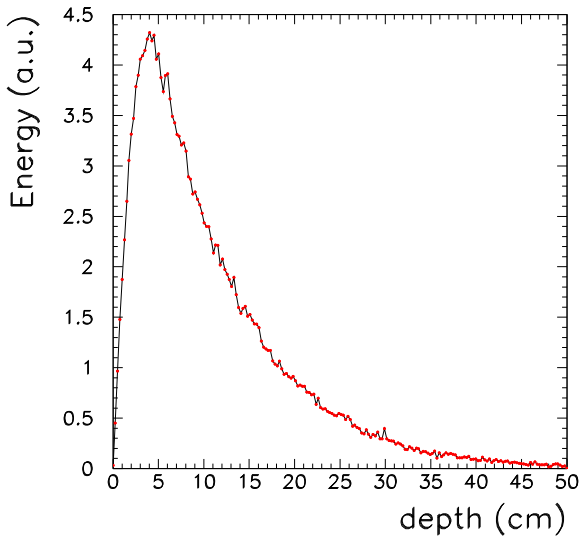

Figure 4.25: An average energy deposit as a function of the distance from the liquid Xenon surface for a 52.8 MeV γ-ray.

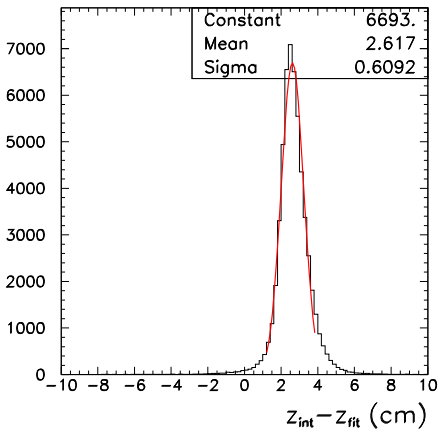

Figure 4.26: Resolution of the γ conversion point z_γ.

3. an algorithm derived by the so–called "principal component analysis" [57] which exploits the information seen by the individual PMTs (linear fit).

The resolutions obtained by the three different methods are shown in Figure 4.27 as a function of the absorption length used in the Monte Carlo simulation. For small absorption lengths the best resolutions are obtained by the "linear fit" method while in the limit of large absorption lengths the three methods

tend to give equivalent results.

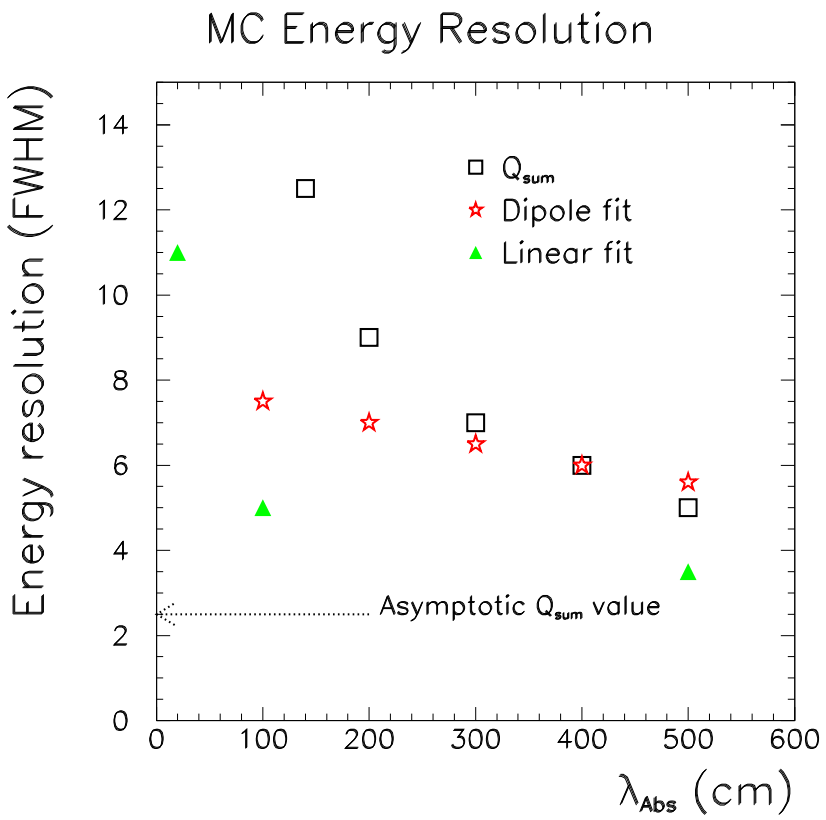

Figure 4.27: Resolutions obtained by the three different methods used for the energy reconstruction of ~ 50 MeV photons as a function of the absorption length used in the Monte Carlo simulation

In the linear fit case, the γ-ray energy is written in a linear approximation as a weighted sum of the charges Q_i seen by each PMT:

$$E_l = c + \sum_i c_i Q_i \tag{4.8}$$

The coefficients c_i and the constant c are determined as follows: a sample of N ($\sim 10^4$) Monte Carlo events is used to compare the linearized value of the energy, E_l, with the true deposited energy, E_t; a χ^2 expression can be formed:

$$\chi^2 = \sum_{\text{MC events}}^{N} (E_l - E_t)^2 \tag{4.9}$$

and the coefficients are obtained requiring that this χ^2 is a minimum. The minimization procedure is

analytical and yields the following results:

$$c = \langle E_t \rangle - \left\langle \sum_j c_j Q_j \right\rangle \tag{4.10}$$

$$c_i = \frac{\mathcal{M}^{-1}}{N-1} \left[\sum_{\text{MC events}}^{N} E_t Q_i \right] - \frac{1}{N} \sum_{\text{MC events}}^{N} E_t \sum_{\text{MC events}}^{N} Q_i \tag{4.11}$$

where the averages are calculated over the event sample and $\mathcal{M}$ is the covariance matrix (computed using the Monte Carlo simulated events):

$$\mathcal{M}_{kl} \simeq \left\langle \left(Q_k - \langle Q_k \rangle\right)\left(Q_l - \langle Q_l \rangle\right) \right\rangle \tag{4.12}$$

Assuming a 100 cm absorption length, this method yields an average of 5% (FWHM) resolution (Fig. 4.28) for γ-rays uniformly entering the detector with energy of 52.8 MeV. This resolution can be further improved by exploiting the knowledge of the photon conversion point: if we prepare different sets of the coefficients c_i for different incident positions in 5×5 cm^2 bins, it improves to 4% (FWHM).

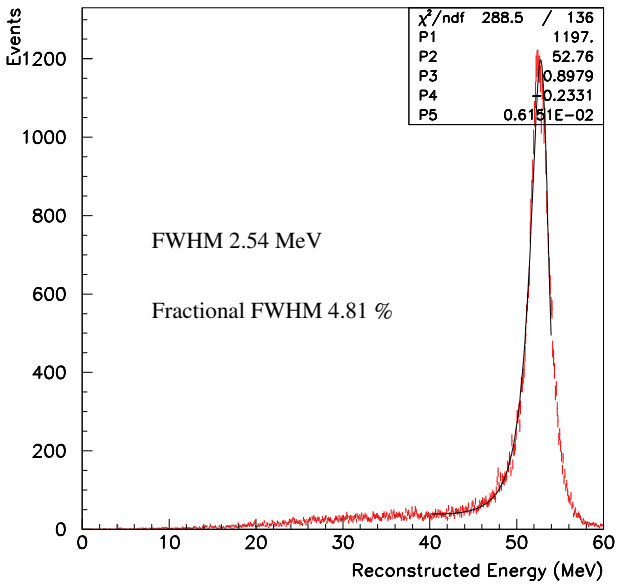

Figure 4.28: Reconstructed energy distribution for photons from $\mu^+ \to e^+\gamma$.

Photon detection efficiency

The effects of the interactions in the front materials and the energy leakage from the front wall are taken into account in the Monte Carlo simulation and cause, for instance, the low energy tail in Fig. 4.28. In the linear fit reconstruction which exploits the knowledge of the photon conversion point we estimate that a 5.6% energy cut (1.4× FWHM) corresponds to a $\approx 60\%$ photon detection efficiency.

Pile-up of Multiple γ-rays

We will make the best use of the scintillation image of γ-interactions provided by all the PMTs and the fast pulse-shape of liquid Xenon scintillation to minimize pile-up of γ-rays which could increase background rates. Fig. 4.29 shows a simulation of a potential pile-up event. There are three handles to separate pile-up γ-rays: spatial separation of two γ-rays by the distribution of the PMT outputs (Fig. 4.29c), pulse timing of the pile-up γ-ray by the PMT nearest to its conversion point (Fig. 4.29b) and pulse-shape separation of the PMT signals (Fig. 4.29a).

Densely placed PMTs effectively work as segmented cells (Fig. 4.29c). According to Monte Carlo simulations two γ-rays, each with an energy greater than 5 MeV, can be distinguished if their incident positions are separated by more than two PMTs (15 cm or 0.2 rad in angles).

Pulse-shape analysis further reduces event pile-up of soft photons using the outputs of the 2 GHz digitizer attached to each PMT. A study with Monte Carlo simulations indicates that two γ-rays, each with an energy greater than 2.5 MeV, can be individually reconstructed if their time difference is more than 10 ns.

Effects of γ-ray pile-ups on the background rates are addressed in Section 6.2.2.

4.3.2 Calibration method

Calibration of the PMTs in the final photon detector will be done by using, in principle, the same method employed in the large prototype study. All PMTs will be tested before installation by measuring their gain and quantum efficiency at the nominal operating voltage. The gain will be continuously monitored and adjusted by using LEDs periodically during the experiment. A relative estimate of the effective quantum efficiency, which includes the collection efficiency of the photoelectrons at the first dynode, under the influence of a magnetic field is as important as the periodic gain calibration of the PMTs. For this purpose, as demonstrated in the large prototype study, scintillation light induced by alpha particles in cold gas Xenon is available because the absorption and scattering effects are small enough that we can well simulate the light transmission. Configuration of the α point sources has to be optimized while designing the PMT configuration on the lateral and back faces.

It is planned to use $\pi^0 \to \gamma\gamma$ decays for absolute energy calibration and for evaluating the detector resolution. The timing resolution will be evaluated as well as that of the positron timing counter by using radiative muon decays.

4.3.3 Cryostat design

Design of the cryostat and cryogenics controlling system has been considered based on the experiences obtained with the large prototype.

We are performing a mechanical calculation of the cryostat by using a finite element analysis method. A technical design of the cryostat is in preparation. Design work of the cryogenics scheme and controlling system has also started, including the circulation and purification scheme. Figure 4.30 shows a preliminary design of the cryogenics system. Detailed examination of the controlling system is in an advanced state.

Xenon will be stored in 8 tanks each of 285 liters volume. Xenon recovery after a test is done by cooling the tanks with liquid nitrogen. Liquefaction and recovery has been repeated seven times during the large prototype study without any problem. For the final detector operation and maintenance, storage

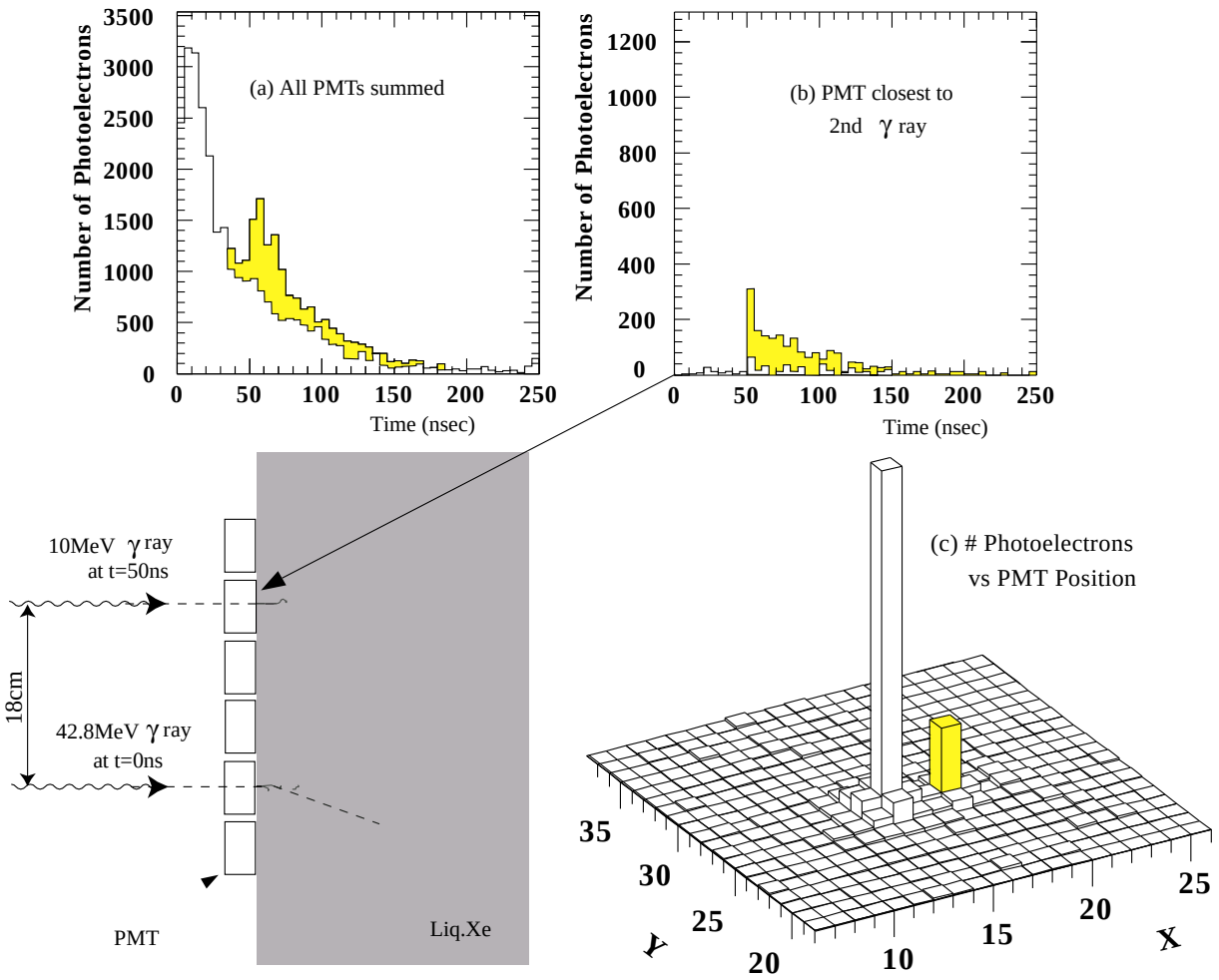

Figure 4.29: A simulated event in which a 43 MeV photon is followed after 50 ns by a 10 MeV photon. Open histograms correspond to signals of the 43 MeV photon and the shaded ones to those of the 10 MeV photon. (a) Pulse-shape (all PMTs summed); (b) Timing of the 10 MeV photon measured by the PMT closest to its conversion point; (c) Spatial separation by the distribution of the PMT outputs (each bin corresponds to a 2"ϕ PMT). The shaded histograms give the contribution from the pile-up event.

and recovery will be done in the same manner. However, it is also important to consider how to recover Xenon in case of an emergency, for example the break of vacuum for the thermal insulation. During the detector operation, for this purpose, the Xenon remaining in the tanks will be transferred to one tank and the other seven tanks will be kept under vacuum. Should it be necessary to recover all the Xenon immediately, due to an unforeseen problem, the gas would be recovered to the seven tanks which act as a 2000 liter buffer. During this recovery to the buffer, the remaining tank will be cooled with liquid nitrogen and start to store Xenon.

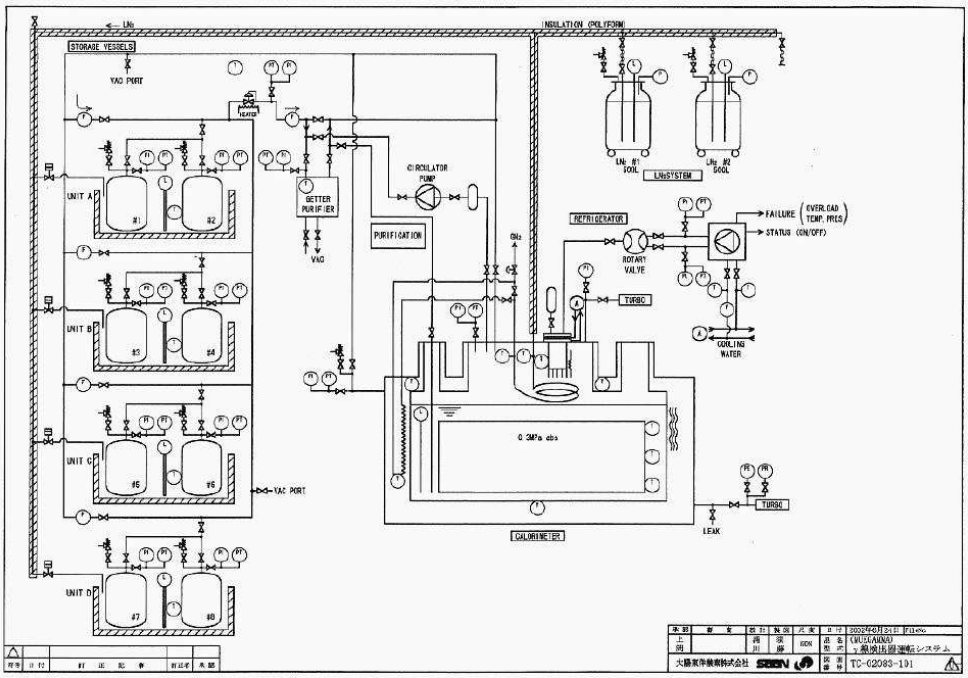

Figure 4.30: Design of the cryogenics system.

5. Electronics, Trigger and DAQ

5.1 Slow Control System

Particle physics experiments require what is commonly referred to as "slow control". This includes the measurement and control of environment variables such as temperature, pressure and humidity as well as the control of high voltages for photomultipliers and wire chambers. While most experiment use an inhomogeneous mix of systems involving RS232, GPIB and PLCs, our experiment will use a new slow control system developed at PSI, called MSCB (Midas Slow Control Bus). This system will be used for the 960 high voltage channels of the experiment, for the control of the liquid Xenon calorimeter and for the superconducting solenoid. The integration of all these systems into the central data acquisition and control system is essential for the long-term stability of the experiment.

The MSCB system uses a field bus–like architecture, where a number of "nodes" are connected to a serial bus, which is controlled by a central PC. Each node contains ADCs, DACs and digital I/O for measurement and controlling tasks. For critical installations the control PC can be backed up by a secondary PC for redundancy. The PCs are connected to the Midas DAQ system [58], which allows for remote operation through a Web interface, history display, automatic alarm notification and for logging of slow control variables to tape.

The hardware of a MSCB node is designed around a new generation of microcontrollers, which contain a 8051-compatible microcontroller core, ADCs, DACs and digital I/O on a single chip. We currently use the ADuC812 [59] from Analog Devices and the C8051F000 from Cygnal [60]. The nodes are connected via an RS-485 bus running at 384 kBaud. A segment can contain 256 nodes, and with one layer of repeaters 65536 nodes can be connected and addressed on a single bus. Two versions of MSCB nodes have been developed. A stand-alone module (Fig. 5.1) which can be embedded directly on a sensor or on an electronics board is powered from the bus, which uses a 10-wire twisted pair flat ribbon cable for distances up to 500 m.

In addition to the stand-alone module, a 19" rack system which hosts cards containing a MSCB node and signal conditioning, has been designed. Cards were made for voltage, current and temperature measurements as well as to control 220 V consumers such as heaters. The MSCB bus runs on the back plane of the crate.

Using the local intelligence of the node controller, regulation loops (PID) and interlock systems can be realized without intervention of the central control PC. The nodes run a simple framework for the communication with the host system, which guarantees real-time behaviour. User routines can be added to implement application-specific logic. The nodes can be reprogrammed over the RS-485 bus.

The MSCB protocol was optimized for minimal overhead. A 16-bit value from a node can be read out by sending a request of three bytes and receiving a reply of four bytes, both including a code (CRC) to avoid data corruption. Depending on the number of nodes, a MSCB system can either use 8-bit or 16-bit addressing. A node can contain up to 256 "channels" for reading and writing and up to 256 "configuration

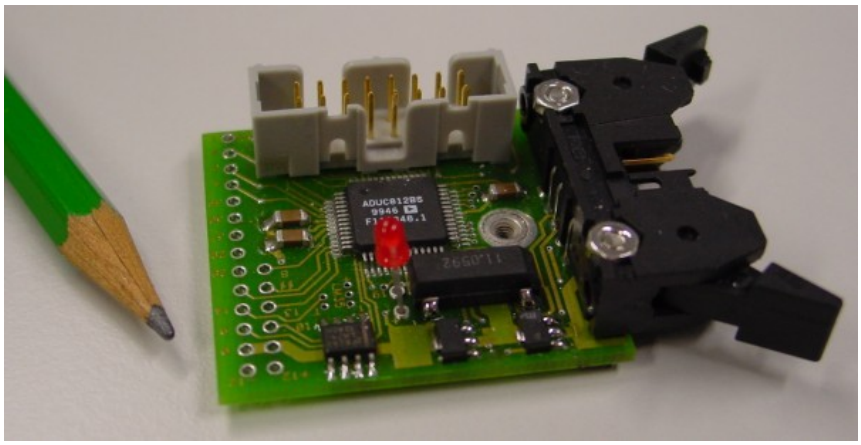

Figure 5.1: Stand-alone node with an RS-485 transceiver, eight channel 12-bit ADC, two channel 12-bit DAC, 16-bit digital I/O and a temperature sensor. The right connector is for the MSCB bus, the one at the back for an optional LCD display.

parameters", which are stored in the EEPROM of the node and can for example be used as constants for PID regulation. Each channel and parameter is described by a set of attributes such as name, physical units and status. These attributes are stored in each node and can be queried from the control PC, making the configuration of large networks very simple. A special repeat mode has been defined which allows the readout of a series of nodes in less than 300 μs per node.

For the control PC a "C" library has been developed running under Windows and Linux. Based on this library, a LabView driver and a driver for the Midas DAQ system are available. Simple LabView applications such as a data logger with graphical display has been implemented.

A prototype of the MSCB rack system is currently used for the pressure and high voltage control at a different experiment and will soon be adapted for the PSI Xenon refilling station. The setup of this system for the control of the photon detector and COBRA magnet is under way.

5.2 High Voltage System

High resolution calorimeters need an excellent stability of the high voltage system. Our 12-stage photomultipliers have a gain variation of about 1% per Volt. Most commercial units have an accuracy of $1 \div 2$ V over the temperature range seen in the PSI experimental hall. This accuracy might not be sufficient in our case.

In order to improve it, a new high voltage system based on the MSCB slow control system is being studied. A common high voltage is distributed to each channel, which regulates its output between zero and the external voltage. Since each channel contains a MSCB node with a microprocessor, an elaborate self-calibration algorithm using two high precision reference voltages can be implemented. This, together with a temperature sensor on each electronics channel, ensures a high voltage stability better than ± 0.3 V over the full temperature range of 20° C to 40° C.

A first prototype with 12 channels has been successfully tested.

5.3 Trigger rate estimates

Detailed simulation studies were performed in order to obtain an estimate of the final acquisition rate expected in the experiment. Background from the accidental coincidence of photons (from the muon radiative decay $\mu^+ \to e^+\nu\overline{\nu}\gamma$ or from positron annihilation in flight) and Michel positrons were considered. A complete GEANT simulation of the proposed experimental set-up was used. We studied the selections based on the photon and positron kinematic variables which could be used in the trigger at various levels.

The photon

The sum of the charge seen by the PMTs of the liquid Xenon photon detector can be used by the trigger to obtain an estimate of the photon energy. By setting a threshold equivalent to a 45 MeV photon energy one achieves a $\sim 97\%$ efficiency on the $\mu^+ \to e^+\gamma$ signal while the fraction (per stopped muon) of background photons satisfying this selection criterion is $f_\gamma \simeq 2 \cdot 10^{-4}$. The rate of the calorimeter events satisfying this requirement would result in:

$$R_\gamma = R_\mu f_\gamma \Omega / 4\pi \tag{5.1}$$

By using a stopping muon rate $R_\mu = 10^8$ μ^+/s and a solid angle fraction Ω of 10% we would obtain a 2 kHz photon event rate.

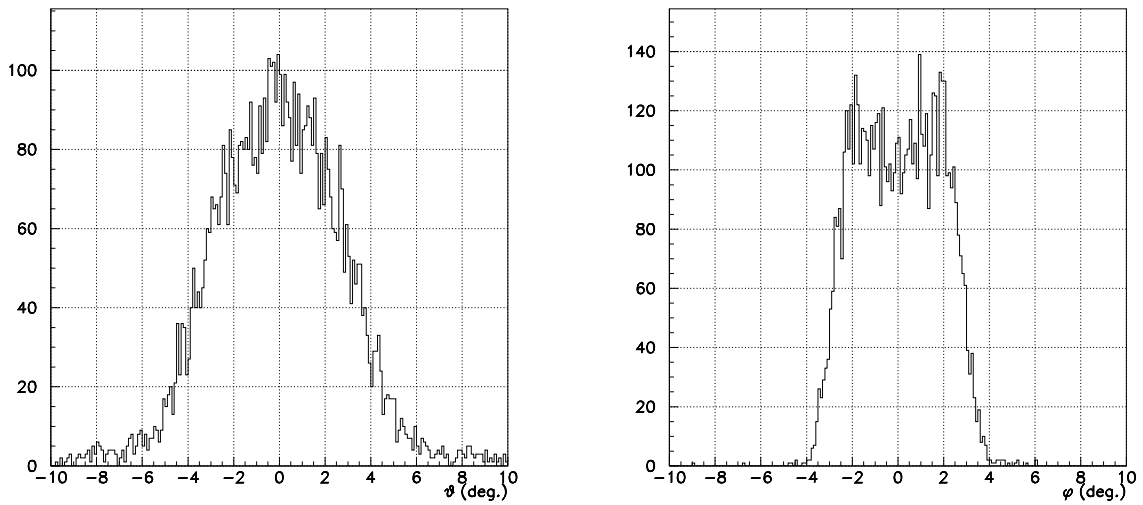

Figure 5.2: Photon direction determination by means of maximum light PMT. The angles are referred to a coordinate system with the polar axis along the μ-beam.

The position of the liquid Xenon photon detector inner face PMT which observed the maximum light gives an estimate of the photon direction which is sufficient for trigger purposes. The determination of the photon direction obtained by connecting the maximum pulse height PMT with the centre of the target is shown in Figure 5.2 relative to the true direction.

The scintillation light emission in liquid Xenon has two decay components and the relative intensity depends on the ionization density of the detected particles. We can define an effective decay time of the ionization light for γ-induced events ($\tau_{\rm eff} \approx 22$ ns). Such a short decay time and the proximity of the photon conversion point to the calorimeter entrance face make the rising edge of the maximum pulse height PMT signal a good estimate of the γ emission time. The Monte Carlo simulated distribution of this variable is shown on the left part of Figure 5.3.

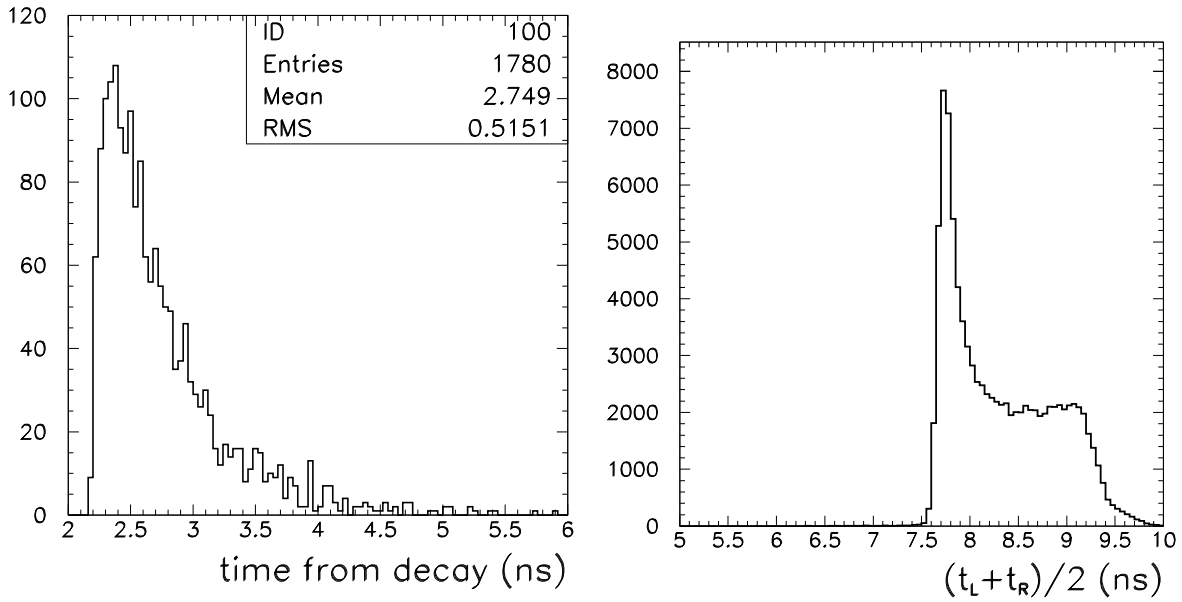

Figure 5.3: Left: Signal time of the PMT with the maximum charge in the calorimeter. Right: Positron impact time on the timing counter.

The positron

The overall rate in the timing counter due to Michel positrons is estimated to be $R_{TC} \simeq 4 \times 10^6$ Hz.

Each scintillating bar of the timing counter is viewed by two PMTs. The mean time of the two PMT signal rising edges is a possible estimator of the positron emission time. The simulated distribution of this estimate is shown in the right part of Fig. 5.3. Without correcting for the positron impact position along the timing counter, the minimal time window, with full efficiency on the $\mu^+ \to e^+\gamma$ event, is ≈ 4 ns. We are testing the operative definition of the signals timing on real PMT pulses, and we can envisage a safer timing coincidence of $\Delta T = 10$ ns between the photon and the positron.

The hit patterns on the timing counters, for $\mu^+ \to e^+\gamma$ events in the angular acceptance range of the calorimeter, can be seen in Figure 5.4. A selection in the photon direction corresponds to a specific region of the timing counter scintillator bars hit by the positron. We found that a 7.5 degree selection in ϕ (coloured bands in Fig. 5.4) corresponds to a spread over five of the 20 scintillator bars for the positrons. The efficiency of this selection on the $\mu^+ \to e^+\gamma$ signal is greater than 99.5%. For the

accidental background the corresponding rejection factor is $f_\phi \simeq 5$. The equivalent rejection factor in the zenith case is lower ($f_\theta \simeq 2$) due to the target angle along the beam axis.

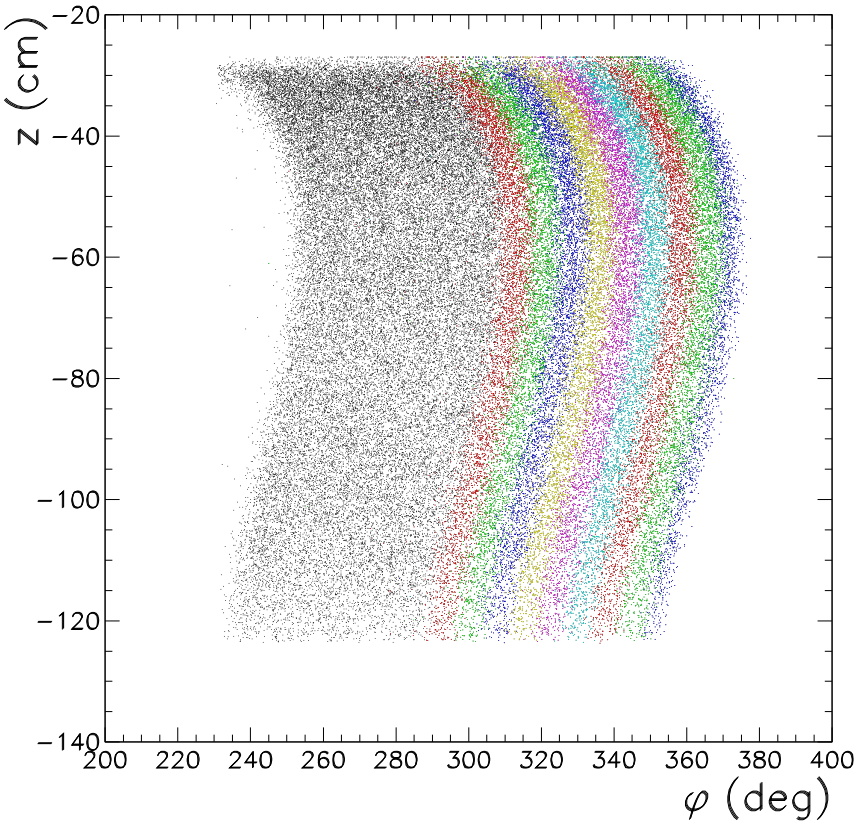

Figure 5.4: Hit patterns on the timing counter for $\mu^+ \to e^+\gamma$ positrons in the acceptance angular range. Different coloured bands correspond to 7.5 degree wide intervals in ϕ.

The maximum radius (R_{DC}) reached by a positron in the drift chamber of the COBRA spectrometer is a measurement of its total momentum. For more than 99.5% of the positrons from $\mu^+ \to e^+\gamma$ decays $R_{DC} > 24$ cm, which corresponds to leave a signal in one of the last seven wires of a drift chamber of the COBRA spectrometer. We can envisage using the signals from these wires as an additional trigger level. However, we estimated that the rejection factor that could be reached in this way is only of about a factor 2.

The trigger rate

We are designing a trigger system that collects signals from the liquid Xenon calorimeter and the timing counters. The information provided by the drift chambers is available with some delay; therefore the drift chambers cannot be used for a fast Level 1 trigger.

We previously mentioned that requiring at least a 45 MeV equivalent energy release in the liquid Xenon calorimeter corresponds to an event rate $R_\gamma = 2$ kHz.

The presence of a hit in the timing counters, within a time coincidence window of $\Delta T = 10$ ns and spatially aligned with the measured photon direction, reduces the uncorrelated background event rate to

$$R_{L1} = 2R_{\gamma}R_{TC}\Delta T\frac{1}{f_{\phi}f_{\theta}} \approx 20\,\mathrm{Hz} \tag{5.2}$$

The estimated trigger rate gives us some margin in case of other possible contributions to the background which are not presently taken into account in this simulation. Different algorithms such as the "linear fit" described in Section 4.3.1 could be easily implemented in the trigger system described in the following.

5.3.1 The trigger system

The trigger system we have adopted is based on a fast (100 MHz) digitization of the liquid Xenon and timing counter PMT signals and on the subsequent treatment of the digitized signals by means of Field Programmable Gate Arrays (FPGAs).

This solution permits individual corrections to each PMT signal: the different PMTs gains can be taken into account and the baseline of each signal can be subtracted. The latter feature is essential for estimating the energy deposited in the Xenon calorimeter by using the sum of the light seen by all the PMTs. Any coherent noise effect, if not corrected, could weaken the efficiency of the energy cut to be used in the trigger.

The FPGAs programmability also allows a very flexible design which can be easily changed and could accomodate even more complicated algorithms than a simple sum.

We are currently designing a trigger system based on only two different electronics boards. A first board (Type1) receives and digitizes the PMT signals, pre-processes the digitized waveforms and sends this information, through Low Voltage Differential Signaling (LVDS) connections, to a second board (Type2) which completes the trigger algorithms. Board Type2 communicates with other boards through LVDS connections too. These two types of boards are arranged in a tree structure, as shown in Fig. 5.5.

Board Type1 is a VME 6U circuit which accommodates 16 FADCs, while board Type2 is a VME 9U circuit with only digital inputs and outputs.

As indicated by the simulation, the front calorimeter face (entrance face) needs, for a good trigger performance, one FADC per PMT while for the lateral and outer faces a four PMT to one FADC fan-in should be tolerable. In this scheme the entire system can be arranged into 3 VME crates (two standard 6U and one 9U), for a total of 42 Type1 and 6 Type2 boards.

The clock frequency of the trigger system is 100 MHz. This choice is a satisfactory compromise between the cost and availability of the components on one side and the required performances on the other. The system needs to be operated synchronously; therefore the clock is distributed by means of Delay Locked Loop (DLL) components. The total trigger latency is evaluated to be 350 ns; this delay can easily be accommodated in the memory depth of the main waveform digitizer of the experiment.

Short description of the boards functions

Board Type1 contains 16 FADCs, one FPGA, a control section and 2 LVDS output connections, for a total throughput rate of 2×5 Gbits/s. The analog-to-digital conversion is performed with a 10-bit device with a 1 V dynamic range.

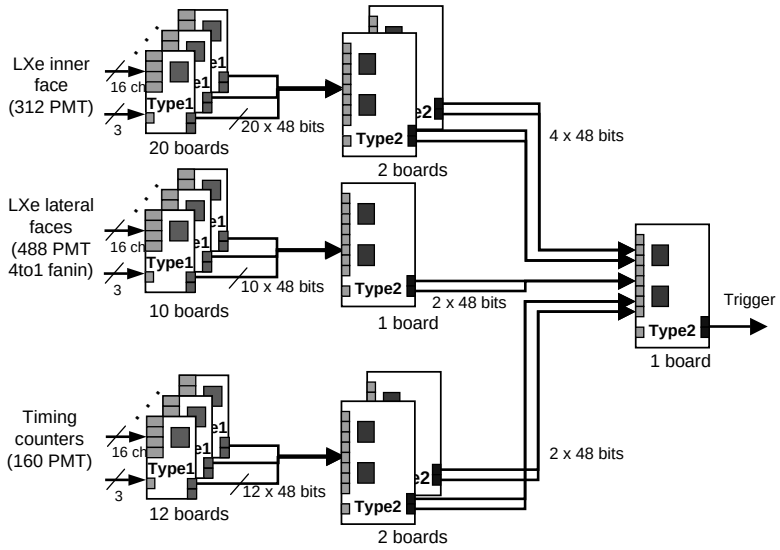

Figure 5.5: The trigger system structure: the two board types are used for the photon calorimeter and for the positron tracker. The boards are arranged in a tree structure.

The Type1 boards have three distinct configurations according to the sub-detector to which they are connected (see Fig. 5.5). The FPGA for the inner calorimeter face implements the following functions:

1. buffering of 16 PMT channel signals;
2. equalization of the PMT gains and, if needed, correction for PMT non-linearity by means of Look-Up-Tables;
3. evaluation of each PMT baseline, and its subtraction from the corresponding signal;
4. search for the PMT corresponding to the maximum signal amplitude;
5. sum of the total collected charge;
6. definition of the signal timing with a precision of one fifth of the clock period;
7. control and debug capability of the data flow.

The board configuration for the other calorimeter faces is similar to this but functions 4) and 6) are not required. The boards for the timing counter have a hit cluster finding algorithm that replaces functions 4) and 5).

Board Type2 contains 2 FPGAs, a control section, 10 input and 2 output LVDS connections, each one with a throughput rate of 5 Gbits/s. The 6 Type2 boards have 4 different FPGA configurations reflecting their different use in the trigger system. The algorithms that these FPGAs should implement are mainly

a subset of those enumerated for board Type1. The chosen board size (VME 9U) is large enough to easily solve the signal routing on the printed circuit, without compromising the signal timing.

Trigger generation

The final board Type2 generates the trigger. The trigger system can generate also other triggers for debugging and calibration purposes. In particular, subsets of the triggers will be generated by relaxing each selection criteria in turn. Further external devices, such as auxiliary calorimeters, may be included in the system for specific calibration purposes by simply adding a dedicated Type1 board in the structure. The redundant number of connections between boards allows also the parallel execution of different sets of trigger algorithms, without increasing the system complexity.

Present status

The FPGA configurations for board Type1 were already designed and simulated, and all the requirements for the calorimeter board were met. The components for the first two prototype boards have already been purchased. The printed circuit design of the prototype board is in progress. This prototype (Type0) is slightly different to a Type1 board. It contains the 16 FADCs and the FPGA like the Type1 board, but it also accommodates the control section of a Type2 board and one input and one output LVDS. Two identical Type0 boards allow a complete system test including all critical aspects:

1. algorithms efficiency with real PMT signals;
2. data transmission and reception between boards;
3. board synchronization;
4. trigger generation.

5.4 Front-end Electronics

Event pile-up in high rate experiments becomes a severe problem. In our case, the coincidence of a γ from radiative muon decay with γs from positron annihilation can easily mimic a γ originating from a $\mu^+ \to e^+ + \gamma$ decay. While Monte Carlo simulations have shown that two incident γs can be spatially separated if their conversion point is more than 15 cm apart, an additional handle is needed. It was therefore proposed to equip all PMTs with waveform digitizers in the GHz range. Studies have shown that two γ-rays, each with an energy greater than 2.5 MeV, can be reconstructed if their time difference is larger than 10 ns.

If the waveform digitizer could achieve sampling speeds above 1 GHz, its timing resolution would be better than 100 ps using sample interpolation, and therefore the usage of conventional ADCs and TDCs could be avoided making the DAQ electronics much simpler. Flash ADCs in the GHz range are still too expensive to use on all the PMTs, but we can follow an earlier development made at PSI [61]. For a different experiment [62] an analog switched capacitor sampling chip has been designed. This chip consists of 128 capacitors, which sample the PMT input signal at a frequency of $500 \div 1200$ MHz. Instead of generating and distributing the sampling frequency directly, the capacitor switches are driven by an

inverter chain, where a trigger signal propagates with high speed through a series of 128 double inverters. Since this is analogous to a domino wave, the chip was named Domino Sampling Chip (DSC). When a waveform has been stored in the capacitors, they are read out at low speed (5 MHz) via a shift register and a commercial ADC (12 bit).

For the $\mu^+ \to e^+\gamma$ experiment, we concluded that a sampling speed of 2 GHz (500 ps bin width) is necessary to obtain a timing resolution of 50 ps via bin interpolation, necessary for the positron timing counter and the liquid Xenon calorimeter. If the domino wave runs continuously in a circular fashion and is only stopped by the trigger, the sampling capacitors can be used as an analog pipeline and delay cables can be avoided. This new chip, called Domino Ring Sampler (DRS) is currently being designed at PSI. The number of storage capacitors has been increased to 1024 and the readout speed via the shift register to 40 MHz. Eight data channels and one calibration channel are integrated on a single chip, which is housed and read out by a custom VME board using 12-bit flash ADCs and FPGAs. The sampling depth of 512 ns accommodates a typical liquid Xenon scintillation pulse of 100 ns width and a pipeline delay of 412 ns which is well above the expected level one trigger latency. A first prototype using a 0.25μ radiation hard technology has been recently submitted. Analog circuit simulations have shown that the domino wave runs steadly at a speed of 2 GHz.

The readout of all nine channels per chip with a single 40 MHz flash ADC consumes 230 μs, which is an acceptable dead time for trigger rates as high as five times than expected.

While all photomultiplier signals will be digitized at 2 GHz, the drift chamber signals are much slower and can be digitized directly with flash ADCs at 100 MHz. Bin interpolation gives a timing resolution of $\sim 1 \div 2$ ns which is equivalent to a position resolution of 100 μm. The FPGA programming will be the same for the boards with the DRS chip and for the drift chamber DAQ boards.

Since the FPGAs are re-programmable through VME, the algorithm can be changed and optimized during the set-up of the experiment. If additional devices such as scalers or constant fraction discriminators are necessary, they can be easily emulated in the FPGAs. It is planned to use VME boards with the DRS chip for the calorimeter readout and the trigger boards with 100 MHz digitizing for the readout of the anodes and cathodes of the drift chambers, thus eliminating the need of any other device except pre-amplifiers, fan-outs and waveform digitizers.

Waveform digitizing on all channels gives an excellent handle on event pile-up and noise suppression, but the amount of raw data per event is large: ~ 1.8 Mb in our case. We are currently studying criteria to reduce and possibly compress the data directly on the FPGAs of the front-end boards.

For sampling speeds in the GHz range, the pile-up rejection is not determined by the sampling speed itself but by the rise time of the signal. As a rule of thumb, two overlaying signals can be distinguished if they are separated by more than the risetime of the signal and they differ not more than a factor of ten in signal height. We measured a rise time of about 8 ns for typical γ induced showers, which gives us a pile-up rejection of 10 ns for individual channels, if the overlaying signals do not differ too much in height. For the pile-up of very small signals, the signal of several photomultipliers have to be combined and the shower shape has to be evaluated. It should be noted that this method reaches its limit if the overlaid signal becomes very small, like 511 keV γs from positron annihilation. The calorimeter must therefore be shielded against this background.

5.5 Data Acquisition

For the $\mu^+ \to e^+ + \gamma$ experiment we will use the MIDAS DAQ system [58], which has been sucessfully used for many years in the PIBETA [62] experiment and has now become the standard DAQ system at PSI and TRIUMF. Besides all the necessary means of data readout, transport and storage, MIDAS contains a full slow control system, an integrated data analysis functionality and a Web interface for remote control. While the current version uses PAW for online data display and analysis, it is planned to switch to ROOT [63]. The software upgrade is scheduled for fall 2002 and supported with additional manpower from TRIUMF.

Automatic calibration and monitoring of the experiment can easily be integrated due to the close coupling of the main DAQ and the slow control. In the PIBETA experiment, for instance, the MIDAS analyzer evaluated all online energy spectra at regular intervals and adjusted the PMT high voltages as necessary. This feature, which ensured a long term stability of the experiment, could be used in this experiment as well. An elaborate alarm system will compare critical histograms with reference histograms and monitor important slow control variables such as Xenon pressure and temperature. In case of problems, operators are notified by alarm sounds in the counting house and by cellular phones.

The expected data rate depends on the trigger rate and the waveform compression in the front end electronics. In addition to $\mu^+ \to e^+ + \gamma$ triggers, we will have a mixture of other triggers for calibration and background analysis. Assuming an overall trigger rate of 100 Hz and an average channel occupancy of 50% for the calorimeter and 10% for the drift chamber and positron counter, the waveform data amounts to 1.2 MB/event or 120 MB/s. To process this data, an online Linux cluster is planned where each node processes a manageable data stream of less than 10 MB/s. Since we want to keep all waveforms for potential $\mu^+ \to e^+ + \gamma$ events but not for the calibration events, a third level trigger will be implemented in this computer farm. For events which are not close to $\mu^+ \to e^+ + \gamma$ events, the waveforms will be analyzed online and only ADC and TDC data will be stored, reducing the data amount dramatically to about 10 kB per event. For the other events the waveforms can be compressed in the Linux farm. The experience of the PIBETA experiment has shown that typical compression rates of a factor of ten are possible. If we decide to keep waveforms for events at a 10 Hz rate and only ADC and TDC values for the other 90 Hz, the data rate becomes 10×1.2 MB $\times\, 0.1 + 90 \times 0.01$ MB $= 2.1$ MB per second, which can be taped easily using current DLT technology.

6. Sensitivity and Background

6.1 Single Event Sensitivity

The detector acceptance defined by the positron spectrometer and the liquid Xenon detector is $0.08 < |\cos\theta| < 0.35$ and $-60^\circ < \phi < 60^\circ$, amounting to $\Omega/4\pi = 0.09$.

We assume a detection efficiency for the photon (ε_γ) of $\sim 60\%$, while for the positron we assume $\varepsilon_e \sim 90\%$.

The single event sensitivity is defined as the $\mu^+ \to e^+ + \gamma$ branching ratio for which the number of expected decays is equal to one.

Assuming a muon stop rate of $N_\mu = 0.3 \times 10^8$/s and a total running time of the experiment $T = 2.6 \times 10^7$ s, the single event sensitivity for this experiment is calculated as

$$B(\mu^+ \to e^+\gamma) = \frac{1}{N_\mu \cdot T \cdot (\Omega/4\pi)} \times \frac{1}{\varepsilon_e \cdot \varepsilon_\gamma \cdot \varepsilon_{sel}} \quad (6.1)$$

$$= \frac{1}{(0.3 \times 10^8) \cdot (2.6 \times 10^7) \cdot 0.09} \times \frac{1}{0.90 \cdot 0.6 \cdot 0.7} \quad (6.2)$$

$$= 3.8 \times 10^{-14}. \quad (6.3)$$

ε_{sel} is the efficiency of the event selection. Selection cuts covering 90% of the signal (1.4 FWHM for gaussian distributions) are considered to be applied on the reconstructed positron energy, on the e^+/γ relative angle and timing. The efficiency for the cut on the photon energy is included in ε_γ.

Should we decide to use a lower beam intensity ($0.2 \times 10^8 \mu$/s) to reduce the accidental background (see next Section) the single event sensitivity might become a bit worse (5.6×10^{-14}).

These sensitivities can be converted to 90% confidence level upper limits, in case of no signal observed, by using the background rate estimates given in the following section. The upper limits we obtain for the two different muon stopping rate hypotheses are 1.0 and 1.6×10^{-13}, respectively.

6.2 Background

There are two major backgrounds to the $\mu^+ \to e^+\gamma$ experiment: (1) Prompt or physics background from radiative muon decays, $\mu^+ \to e^+\nu_e\overline{\nu}_\mu\gamma$, and (2) accidental background. The backgrounds crucially depend on detector performances. With the expected performances of our detectors, summarized in Table 6.1, the accidental background poses more threat than the prompt one.

The accidental background B_{acc} can be approximately estimated by using the following formula [64, 10]:

$$B_{acc} \propto \delta E_e \cdot \delta t_{e\gamma} \cdot (\delta E_\gamma)^2 \cdot (\delta\theta_{e\gamma})^2 \quad (6.4)$$

The resolutions and the upper limits obtained by the previous experiments can be found for comparison in Appendix A (See Table A.1).

	FWHM
ΔE_e	$0.7 \div 0.9\%$
ΔE_γ	4%
$\Delta\theta_{e\gamma}$	$17 \div 20.5$ mrad
$\Delta t_{e\gamma}$	0.15 ns

Table 6.1: Expected detector performances.

6.2.1 Prompt Background

The prompt background was calculated using the formula given in [65, 66]. By numerical integration over the selection cuts (1.4 FWHM for each selection variable) we find a background of $2.2 \div 3.7 \times 10^{-15}$ events per muon decay, depending on the resolution values assumed (See Tab. 6.1).

6.2.2 Accidental Background

The inclusive photon yield per muon decay $g_\gamma(y)$ ($y \equiv 2E_\gamma/m_\mu$) was evaluated in [10] by taking into account the following sources of photons:

1. photons from radiative muon decays;
2. photons from annihilation-in-flight;
3. photons from positron interactions with surrounding materials;
4. neutron induced background.

The integrated yield $f_\gamma(y) = \int_y^1 dy' g_\gamma(y')$ is plotted in Fig. 6.1. With a δy cut of 2.8%, the annihilations-in-flight give a slightly larger contribution than radiative decays. The rate of two photon pile-up can be written as:

$$g_{\gamma\gamma}(y) = \int_0^y dy' g_\gamma(y') g_\gamma(y - y') \eta(y', y - y'), \tag{6.5}$$

where $\eta(y_1, y_2)$ is the pile-up rejection factor for two photons with energy fractions y_1 and y_2, and $0 < y < 2$. It depends on $\Delta\Omega_{\gamma\gamma}$ and $\Delta t_{\gamma\gamma}$ which define the two-photon separation power in solid angle and in time respectively, and are dependent on the energies of the photons. They are evaluatedy by Monte Carlo simulations (See Section 4.3.1).

The pile-up spectrum $g_{\gamma\gamma}(y)$ is then integrated from $(1 - \delta y)$ to $(1 + \delta y)$, $f_{\gamma\gamma}(y) = \int_{1-\delta y}^{1+\delta y} dy' g_{\gamma\gamma}(y')$, where $y \equiv 1 - \delta y$. The resulting integrated pile-up photon rate $f_{\gamma\gamma}(y)$ is shown in Fig. 6.2. With a δy cut of 2.8%, $f_{\gamma\gamma}$ is a non-negligible $(10 \div 15\%)$ fraction of the single photon rate which must be considered in the background calculations.

The rate of accidental coincidences of Michel positrons with random photons given by $f_\gamma(y) + f_{\gamma\gamma}(y)$ is obtained by numerical integration over the selection cuts. We find an accidental background of $2.2 \div 3.5 \times 10^{-14}$ events per muon decay, depending on the resolution values assumed (See Tab. 6.1) and with a stopping muon rate ranging between 0.2 and 0.3×10^8/s.

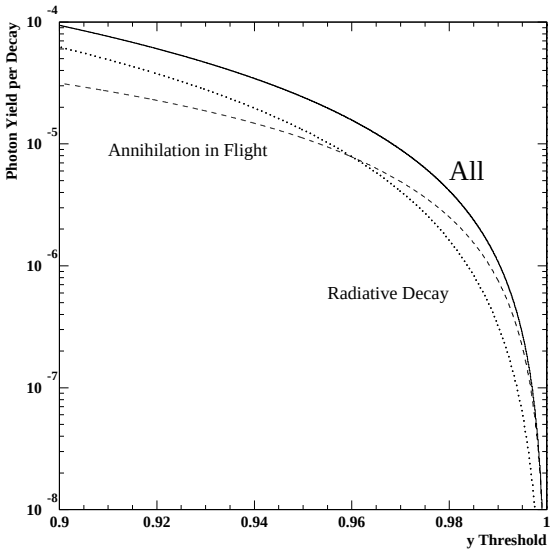

Figure 6.1: Integrated photon yield per muon decay $f_\gamma(y)$.

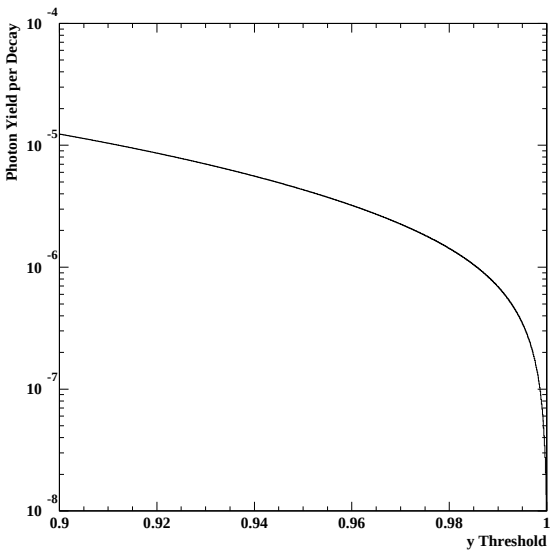

Figure 6.2: Integrated pile-up photon yield per muon decay $f_{\gamma\gamma}(y)$.

7. Collaboration, Cost and Schedule

7.1 Collaboration

We plan the following subdivision of responsibilities for the organization of the experiment and the apparatus construction:

- spokespersons: T. Mori, A. Baldini
- technical coordinator: S. Ritt
- responsible institutes for the different devices:
  - Beam Line: PSI
  - COBRA Magnet: KEK–Tokyo
  - Drift Chambers: PSI
  - Timing Counters: Genova–Pavia
  - Photon Detector: Tokyo–KEK–Pisa
  - Trigger: Pisa
  - Electronics and DAQ: PSI

All the collaborators are listed on the first page of this report. The number of full equivalent physicists is 14 for Japan, 10 for Italy and 3 for PSI. The collaborators from Waseda University, BINP and Osaka University mostly help with the technical aspects of the photon detector. The Pisa construction responsibility in the photon detector concerns the PMT procurement and testing.

7.2 Cost

A subdivision of the costs of the experiment for all the different detectors is given in Table 7.1. The subdivision of responsibilities illustrated in Section 7.1 implies the budgetary subdivision among the three main countries shown in Table 7.2.

7.3 Schedule

Results should be obtained before the LHC experiments (and the proposed $\mu \to$ e conversion experiment [9]) to make a possible first discovery or place most stringent limits on the new physics.

- Beam line tuning with the COBRA magnet in the later part of 2003;

System	Item	Cost US$M
Liq. Xe Scintillation Detector	Liquid Xe	0.900
	Vessel and Refrigerator	0.305
	PMTs	1.667
	Feedthroughs, cables, connectors	0.158
	Xe system purification, Refrig., Tanks, Vacuum	0.430
Drift Chambers		0.142
Timing Counters		0.700
Superconducting Solenoid		1.250
Beam Line		0.140
HV		0.124
Trigger		0.400
Readout Electronics and Data Acquisition		0.430
Total		6.646

Table 7.1: Cost estimation

Country	US$k
Japan	2800
Italy	2500
Switzerland	1300

Table 7.2: Cost subdivision

- Engineering runs in 2004.
- A total running time of about two years.

A. The Past Experiments

Experimental searches for $\mu^+ \to e^+\gamma$ have a long history reaching back to 1948 [67]. During the past 25 years the experimental sensitivity to this decay mode was raised by two order of magnitudes. Experimental efforts have been devoted to the improvement of detection resolutions of four variables, namely the positron energy E_e, the photon energy E_γ, the timing between the positron and photon $\Delta t_{e\gamma}$, and the angle between the positron and photon $\Delta\theta_{e\gamma}$. Various kinds of apparatus have been used. In Table A.1, the experimental results of 90% C.L. upper limits of $\mu^+ \to e^+\gamma$ decay are listed with their detector resolutions.

Place	Year	ΔE_e	ΔE_γ	$\Delta t_{e\gamma}$	$\Delta\theta_{e\gamma}$	Upper limit	References
SIN	1977	8.7%	9.3%	1.4 ns	–	$< 1.0 \times 10^{-9}$	[68]
TRIUMF	1977	10%	8.7%	6.7 ns	–	$< 3.6 \times 10^{-9}$	[69]
LANL	1979	8.8%	8%	1.9 ns	37 mrad	$< 1.7 \times 10^{-10}$	[70]
LANL	1986	8%	8%	1.8 ns	87 mrad	$< 4.9 \times 10^{-11}$	[71]
LANL	1999	1.2%*	4.5%*	1.6 ns	17 mrad	$< 1.2 \times 10^{-11}$	[1]

* shows an average of the numbers given in [1].

Table A.1: Chronology of $\mu^+ \to e^+\gamma$ searches since the era of meson factories. The resolutions quoted are given as full width at half maximum (FWHM).

Bibliography

[1] MEGA Collaboration, M. L. Brooks *et al.*, Phys. Rev. Lett. **83** (1999) 1521;
MEGA Collaboration, M. Ahmed *et al.*, Phys. Rev. **D65** (2002) 112002.

[2] R. Barbieri and L.J. Hall, Phys. Lett. **B338** (1994) 212;
R. Barbieri, L.J. Hall, and A. Strumia, Nucl. Phys. **B445** (1995) 219.

[3] Super-Kamiokande Collaboration, Y. Fukuda *et al.*, Phys. Rev. Lett. **81** (1998) 1562;
Super-Kamiokande Collaboration, Y. Fukuda *et al.*, Phys. Lett. **B433** (1998) 9 and **B436** (1998) 33;
Super-Kamiokande Collaboration, Y. Fukuda *et al.*, Phys. Rev. Lett. **82** (1999) 2644;
Super-Kamiokande Collaboration, Y. Fukuda *et al.*, Phys. Rev. Lett. **85** (2000) 3999.

[4] Super-Kamiokande Collaboration, Y. Fukuda *et al.*, Phys. Rev. Lett. **81** (1998) 1158;
Super-Kamiokande Collaboration, S. Fukuda *et al.*, Phys. Rev. Lett. **86** (2001) 5651;
Super-Kamiokande Collaboration, S. Fukuda *et al.*, Phys. Rev. Lett. **86** (2001) 5656.

[5] SNO Collaboration Q. R. Ahmad *et al.*, Phys. Rev. Lett. **87** (2001) 071301;
SNO Collaboration Q. R. Ahmad *et al.*, Phys. Rev. Lett. **89** (2002) 011301;
SNO Collaboration Q. R. Ahmad *et al.*, Phys. Rev. Lett. **89** (2002) 011302.

[6] M. Gell-Mann, P. Ramond and R. Slansky, in *Supergravity*, Proceedings of the Workshop, Stony Brook, New York, 1979, ed. by P. van Nieuwenhuizen and D.Freedman (North-Holland, Amsterdam);
T. Yanagida, in Proceedings of the Workshop on Unified Theories and Baryon Number in the Universe, Tsukuba, Japan, edited by A. Sawada and A.Sugamoto (KEK Report No. 79-18, Tsukuba) (1979).

[7] J. Hisano and D. Nomura, Phys. Rev. **D59** (1999) 116005 and references therein.

[8] A. Czarnecki, W. J. Marciano and K. Melnikov, Talk given at Workshop on Physics at the First Muon Collider and at the Front End of a Muon Collider, Fermilab, Nov. 6–9, 1997 (hep-ph/9801218);
J. Äystö et al., *Physics with low–energy muons at a neutrino factory complex*, CERN-TH/2001-231.

[9] MECO Collaboration, W. Molzon spokesman, *A Search for* $\mu^- N \to e^- N$ *with Sensitivity Below* 10^{-16}, AGS proposal P940, 1997.

[10] *Search for* $\mu^+ \to e^+ + \gamma$ *down to* 10^{-14} *branching ratio*, PSI Proposal R-99.05.1, May 1999.

[11] G.W. Bennet *et al.*, hep-ex/0208001 v2 (2002).

[12] J. Hisano and K. Tobe, Phys. Lett. **B510** (2001) 1997

[13] L. J. Hall and Y. Nomura, hep-ph/0205067 (2002).

[14] L.J. Hall, V.A. Kostelechy and S. Raby, Nucl. Phys. **B267** (1986) 415.

[15] J. Hisano, T. Moroi, K. Tobe and M. Yamaguchi, Phys. Lett. **B391** (1997) 341 and Erratum, Phys. Lett. **B391** (1997) 357

[16] The ALEPH, DELPHI, L3 and OPAL Collaborations, and the LEP Higgs Working Group, *Searches for the Neutral Higgs Bosons of the MSSM: Preliminary Combined Results Using LEP Data Collected at Energies up to 209 GeV*, LHWG Note/2001-04, hep-ex/0107030, July 2001

[17] MACRO Collaboration, Phys. Lett. **B434** (1998) 451

[18] Soudan Collaboration, Phys. Lett. **B391** (1997) 491

[19] R. Davis Jr., D.S. Harmer, and K.C. Hoffman, Phys. Rev. Lett. **20** (1968) 1205;
B. Cleveland *et al.*, Ap. J. **496** (1998) 505

[20] Gallex Collaboration, Phys. Lett. **B285** (1992) 376;
Gallex Collaboration, Phys. Lett. **B357** (1995) 237;
Gallex Collaboration, Phys. Lett. **B388** (1996) 384;
Gallex Collaboration, Phys. Lett. **B447** (1999) 127.

[21] SAGE Collaboration, Phys. Rev. Lett. **83** (1999) 4686

[22] GNO Collaboration, Phys. Lett. **B490** (2000) 16

[23] Kamiokande Collaboration, K.S. Hirata *et al.*, Phys. Rev. Lett. **63** (1989) 16;
Kamiokande Collaboration, K.S. Hirata *et al.*, Phys. Rev. Lett. **65** (1990) 1297.

[24] J. Hisano, T. Moroi, K. Tobe, M. Yamaguchi and T. Yanagida, Phys. Lett. **B357** (1995) 579.

[25] J. Hisano, D. Nomura T. Yanagida, Phys. Lett. **B437** (1998) 351.

[26] A. Badertscher, D. Renker and L. Simons, PSI internal report (1989);
PSI Users' Guide, Accelerator Facilities.

[27] A. Baldini *et al.*, *Update & Supplement to LOI R-98-05.0/1*, BV29, July 1999.

[28] *Report on the Progress for the* $\mu^+ \to e^+\gamma$ *Experiment at PSI*, Progress Report Jan. 2002.

[29] TRANSPORT - *A Computer Program for Designing Charged Particle Beam Transport Systems*, K.L. Brown *et al.* CERN Yellow Report 73-16, (1973);
Decay TURTLE - *A Computer Program for Simulating Charged Particle Beam Transport Systems, including Decay Calculations* K.L. Brown and Ch. Iselin, CERN Yellow Report 74-2 (1974);
Graphics versions of both Programmes by U. Rohrer PSI-Report (1980).

[30] GEANT - *Detector Description and Simulation Tool*, Applications Software Group CERN, CERN Program Library Writeup W5013 (1993).

[31] MEG technical note TN015, June 2002.
(http://meg.psi.ch/docs/index.html)

[32] A. Yamamoto *et al.*, Nucl. Phys. **B78** (1999) 565–570.

[33] The tolerance to the magnetic field was measured by the Hamamatsu Photonics.

[34] J. Allison *et al.*, Nucl. Instr. and Meth. **A310** (1991) 527.

[35] BELLE Collaboration, *BELLE Progress Report*, KEK Report 97-1, April 1997;
BELLE Collaboration, *BELLE Technical Design Report*, KEK Report 95-1, April 1995.

[36] BaBar Collaboration, *Technical Design Report*, March 1995.

[37] O. Nitoh *et al.*, Jpn. J. Appl. Phys. **33** (1994) 5929.

[38] *R&D Report on the drift chamber prototype at Univ. of Tokyo*, May 2001,
Muegamma technical note TN013.
(http://meg.psi.ch/docs/index.html)

[39] *Report on the Progress for the* $\mu^+ \to e^+\gamma$ *Experiment at PSI*, Progress Report, January 2001.

[40] K. Abe *et al.*, MEG-TN012 (2000).

[41] MUEGAMMA Collaboration, *PSI Annual Report* (2001).

[42] R. Bellazzini *et al.*, Nucl. Instr. and Meth. **A457** (2001) 22.

[43] H. Kichimi *et al.*, Nucl. Instr. and Meth. **A453** (2000) 315.

[44] T. Doke, Nucl. Instr. and Meth. **A327** (1993) 113.

[45] A. Hitachi *et al.*, Phys. Rev. **B27** (1983) 5279.

[46] L. M. Barkov *et al.*, Nucl. Instr. and Meth. **A379** (1996) 482,

[47] S. Orito, The first workshop on $\mu \to e\gamma$ at PSI, March 1997.

[48] ATLAS Liquid Argon Calorimeter Technical Design Report, CERN/LHCC/96-41, ATLAS TDR 2, December 15, 1996.

[49] Oxisorb is a trade mark of Messer Griesheim GmbH.

[50] S. Mihara *et al.*, IEEE Transactions **49** n.2 (2002).

[51] MEG collaboration, *Status report to the PSI Scientific Committee*, July 2002, available at http://meg.psi.ch/docs/index.html

[52] MEG technical note TN017, June 2002.
(http://meg.psi.ch/docs/index.html)

[53] MEG technical note TN014, Apr. 2002.
(http://meg.psi.ch/docs/index.html)

[54] N. Ishida *et al.*, Nucl. Instr. and Meth. **A384** (1997) 380-386.

[55] G. M. Seidel, R. E. Lanou and W. Yao, hep-ex/0111054

[56] MEG technical note TN018, Jan. 2001.
(http://meg.psi.ch/docs/index.html)

[57] S. Belforte *et al.*, *SVT Technical Design Report*, CDF note 3108 (1994); CERN EP report 81-12/ReV.

[58] MIDAS home page, http://midas.psi.ch

[59] http://products.analog.com/products/info.asp?product=AduC812

[60] http://www.cygnal.com/products/C8051F000.htm

[61] C. Brönnimann *et al.*, Nucl. Instr. and Meth. **A420**, 264 (1999)

[62] PIBETA experiment at PSI, http://pibeta.psi.ch

[63] http://root.cern.ch

[64] S. Korenchenko *et al.*, *Letter of Intent for an experiment at PSI*, R-98-05.0 (1998), available at http://meg.psi.ch/docs.html

[65] Y. Kuno and Y. Okada, Phys. Rev. Lett. **77** (1996) 434.

[66] C. Fronsdal and H. Überall, Phys. Rev. **113** (1959) 654;
S. G. Eckstein and R. H. Pratt, Ann. of Phys. **8** (1959) 297.

[67] E.P. Hincks and B. Pontecorvo, Phys. Rev. Lett. **73** (1948) 246.

[68] A. Van der Schaaf *et al.*, Nucl. Phys. **A340** (1980) 249.

[69] P. Depommier *et al.*, Phys. Rev. Lett. **39** (1977) 1113.

[70] W.W. Kinnison *et al.*, Phys. Rev. **D25** (1982) 2846.

[71] R.D. Bolton *et al.*, Phys. Rev. **D38** (1988) 2077.